SURFACE GLASSY DYNAMICS AND SINGLE-MOLECULE ABSORPTION OF QUANTUM DOTS DETECTED BY SCANNING TUNNELING MICROSCOPY

BY

DUC ANH NGUYEN

DISSERTATION

Submitted in partial fulfillment of the requirements
for the degree of Doctor of Philosophy in Chemistry
in the Graduate College of the
University of Illinois at Urbana-Champaign, 2016

Urbana, Illinois

Doctoral Committee:

Professor Martin Gruebele, Chair
Professor Joseph W. Lyding
Professor Gregory S. Girolami
Professor So Hirata

Abstract

Using optically assisted scanning tunneling microscopy (STM), I investigated surface glassy dynamics, absorption spectroscopy and intermolecular energy transfer between single quantum dots (QDs) and carbon nanotubes (CNTs).

Glass is an exotic state of matter which is not in equilibrium, but can be stable for billions of years. However, the microscopic understanding of glasses, the glass transition and glass dynamics remains a highly debated area. In addition to the bulk glass, studying surface glass dynamics likely contributes equally towards understanding the connection between theories of glass and experiments to test these theories.

In the first part of this thesis, I studied surface glassy dynamics by making STM movies of various amorphous surfaces at room temperature in a wide temporal range from 10^{-3} s to ~10^{5} s. STM movies reveal that the surface of metallic glasses and amorphous materials consists of a disordered network of cooperatively rearranged regions (CRRs or clusters). On all investigated surfaces, CRRs have an average size of ~4-5 glass forming units and mostly relax in a two-state fashion. Dynamics of single CRRs was also monitored by parking the STM tip on the top and measuring the tunneling as a function of time. CRRs on the glass surfaces show excess fluctuations in tunneling current compared to measurements on crystalline surfaces. By quantifying this fluctuations, I was able to reconstruct the energy landscape of two-state hopping.

At sufficient low temperature in the supercooled liquid regime, glass dynamics is split into two modes of relaxation, primary α-relaxation which is responsible for the glass transition and secondary β-relaxation which is thought to be the precursor of the α -relaxation. In the glassy regime, β-relaxation is the main relaxation mode which is important for mechanical properties of glasses. I investigated a system of La-based metallic glasses with distinct β-relaxation characteristics, ranging from a pronounced peak to a shoulder relative to the α-relaxation peak. This study allows us to correlate the atomic mobility with nanoscale hopping of surface CRRs.

Glass dynamics is strongly influenced by external perturbation including mechanical, thermal and optical stresses. I investigated surface glassy dynamics under optical stress by making movies on amorphous silicon carbide surface irradiated with above-bandgap light. The glass surface relaxes faster under light illumination, mainly by recruiting previously immobile

clusters to hop. This photoinduced enhancement of surface dynamics follows an athermal electronic mechanism, which could underlie photoinduced aging and relaxation in glasses.

Interaction and energy transfer between QDs and other molecules are important for applications in biological imaging, solar cells and photocatalysis. In the second part of this thesis, optically assisted STM was employed to investigate absorption and intermolecular energy transfer between single QDs and CNTs. Single PbS, CdSe, CdSe/ZnS QDs and CNTs were deposited onto gold, crystalline silicon carbide and amorphous silicon carbide surfaces by matrix-assisted dry contact transfer. Adsorbed molecules were excited with modulated 532 nm light and the modulated tunneling current proportional to the optical absorption signal was detected by STM with a lock-in amplifier. Absorption of individual QDs varies significantly on all investigated surfaces. Single QD absorption shape and intensity are strongly dependent on the sample bias voltage, reflecting different excited states. Using the STM tip, QDs can be moved on the surface, and three-dimensional absorption shapes were imaged. In arrays of QDs, absorbed energy is funneled to one or a few QDs. Evidence of energy transfer between single QDs and single CNTs was also observed.

To Linh, Minh and my family.

Acknowledgements

First and foremost, I would like to thank my advisor, Professor Martin Gruebele, for his constant mentoring and support. I have learned a lot from him, not only in science, but also in many other aspects. He has encouraged and inspired me to think of many new ideas which have turned out to be very helpful. Without his support, this work would not have been possible.

Secondly, I would like to thank Professor Joseph W. Lyding for instructing me to operate and exploit many features of the STM. His willingness and patience in helping me troubleshoot the STM is invaluable. He also gave me many technical suggestions in performing experiments.

A special thank is sent to Dr. Sumit Ashtekar for training me on STM and glass dynamics in my first year. This helped me develop a solid background in these fields.

I really appreciate the members in the Gruebele and Lyding groups who have overlapped with me during my time at UIUC for their feedback on my works. In particular, I would like to thank Dr. Lea Nienhaus for her help in setting up the laser and training on making PtAu thin films. Also, great thanks to Adrian Radocea and Dr. Justin C. Koepke for a lot of helpful discussion about STM and various aspects of the experiments. In addition, I was lucky to have a chance to work with diligent undergraduate students. Thanks to Brian Pringle and Nhan Nguyen for their help in part of the data collection.

Finally, I would like to thank my family for their endless support. Without the encouragement and support from my wife, I would not have obtained the achievements as today. In addition, my parents always encourage me in my tough time. Moreover, they are willing to travel to UIUC to help me take care of my son, thus I could completely focus on my work.

Table of Contents

Part I: Surface Glassy Dynamics

1. Introduction to glasses, the glass transition and glass dynamics

1.1. Glasses and the glass transition

Glasses have been used for thousands of years, covering a wide range of applications from daily appliances to electronic, medical and optical devices.[1,2] However, despite of their popular uses, the microscopic understanding of glasses and the glass transition remains a highly active and controversial area.[2-4]

Glasses are formed by supercooling a liquid.[5] In Fig. 1.1, enthalpy or volume is measured as a function of temperature.[2] When a liquid is cooled slowly, it crystallizes through an abrupt transition at the melting temperature T_m. A crystal of low enthalpy or volume is formed. If the liquid is cooled fast enough, crystallization is avoided and the liquid state is maintained even below the melting temperature. This form of liquid is a supercooled liquid. Upon further cooling, a supercooled liquid finally smoothly solidifies and a glass is formed. The temperature at which a supercooled liquid becomes a glass is the (thermodynamic) glass transition temperature T_g. T_g depends on the cooling rate; the faster the cooling rate, the higher the value of T_g (curve b in Fig. 1.1). However, the range of T_g for a specific material is narrow because viscosity of the liquid increases so rapidly as the temperature drops. In practical terms, T_g is the temperature where the liquid seems to stop flowing to a human observer.

Schematic structures of liquid, glass and crystal are shown in Fig. 1.2. Glass has similar structure to liquid, a random packing of atoms or molecules, but with higher density preventing flow. One of the biggest challenge in the field of glasses is to understand why viscosity and relaxation timescale increase approximately 10 orders of magnitude in a narrow temperature window as the glass transition is approached, yet without a substantial change in structure.[6]

1.2. Bulk glass dynamics

At high enough temperature in the liquid state, a single relaxation mode governs the dynamics and transport is collisional.[2,7] At lower temperature in the supercooled liquid regime, the dynamics is governed by collectively activated motions and the relaxation is split into two modes, primary α-relaxation and secondary β-relaxation. α-relaxation is slower, is responsible

for the glass transition and vanishes (slows down to become immeasurably slow) near the glass transition temperature T_g where the relaxation time (viscosity) reaches 100 s (10^{12} Pa.s or 10^{13} poise). Faster β-relaxation is thought to be the precursor of α-relaxation and continues below T_g (Fig. 1.3). Understanding the structural and dynamical origins and correlations of the α-relaxation and β-relaxation is the key step in understanding glasses and the glass transition.[2]

1.2.1. Primary α-relaxation

The temperature dependence of the α-relaxation time and viscosity is non-Arrhenius as shown in Fig 1.3 and is often described by the Vogel-Fulcher-Tammann (VFT) law:[2]

$$\log_{10}(\tau_\alpha / s) = A + B/(T - T_0) \qquad (1.1)$$

where A and B are constants and B is material dependent. At the temperature T_0, the relaxation time and viscosity diverges. The kinetic temperature T_0 equals to the extrapolated thermodynamic Kauzman temperature T_K below which the enthalpy of the supercooled liquid is lower than the crystal,[8] as shown in Fig. 1.1. Both T_0 and T_K signify an "ideal glass" transition where a glass without structural relaxation and lowest enthalpy or volume is formed.[2,3,9]

The degree of deviation of α-relaxation from the Arrhenius dependence is quantified by fragility *m* which is the slope in a $\log_{10}(\tau_\alpha / s)$ versus T_g / T plot at T_g:[10,11]

$$m = \partial \log_{10}(\tau_\alpha / s) / \partial (T_g / T) \text{ at } T = T_g \qquad (1.2)$$

The smaller the value of fragility *m*, the more Arrhenius the α-relaxation is. Fragility is also used to classify glasses as strong (low fragility *m* and more Arrhenius) and fragile (high fragility *m* and more non-Arrhenius). Covalent network materials such as SiO_2 usually form strong glasses while glasses formed from small organic molecules are fragile.[10]

The non- Arrhenius nature of α-relaxation is explained using cooperativity.[2,7] α-relaxors are cooperatively rearranging regions (CRRs ≡ clusters) that have a compact shape with a length scale of ~1-4 nm[12,13] or ~ 5 glass forming units according to the random first order transition (RFOT) theory.[7] As the temperature decreases, α-CRRs grow in size and thus activation barriers.[7,14] The growing length scale of α-CRRs accompanying the glass transition results in the non-Arrhenius dependence. At the glass transition, the activation barrier for bulk α-relaxation is ~ 35 $k_B T_g$.[7,15]

The temporal evolution of α-relaxation at constant temperature is non-exponential and follows a stretched exponential dependence:[2]

$$\phi(t) = \phi_0 \exp[-(t/\tau_\alpha)^\beta], \ \beta < 1 \quad (1.3)$$

where $\phi(t)$ is the response function to a perturbation, such as stress inducing a delayed deformation, or the natural relaxations of individual α-relaxors if they could somehow be imaged. The stretching parameter β measures the deviation from the exponential case. β depends on the materials and degree of crystallinity contamination.

The non-exponential behavior of α-relaxation is explained using spatial and temporal heterogeneities.[2,7] In the spatial heterogeneity picture, each α-CRR follows an exponential relaxation, but with different time constants τ_α leading to the overall stretched exponential behavior. In the temporal heterogeneity picture, the time constant of an α-CRR varies over time and each α-CRR follows a stretched exponential relaxation. Recent studies show that spatial heterogeneity is more dominant on times scales accessible to experiment,[16] partially due to long time required to observe temporal heterogeneity.

α-relaxation is non-ergodic.[17] As the glass transition is approached, the α-relaxation timescale diverges. Thus, the material cannot response to further fast decreasing in temperature and falls out of equilibrium, as the glass is formed. In the glassy state, the relaxation is termed "aging". Because of the aging, spatial averaging and temporal averaging are no longer equivalent.

1.2.2. Secondary β-relaxation

Determining characteristic behaviors and origins of β-relaxation is more challenging because of its overlap with α-relaxation above T_g, and the long observation time required below T_g where β-relaxation is the main relaxation mode.[17,18] The microscopic origin of the β-relaxation is highly debated.[17] Theory predicts that β-relaxation arises from random fluctuation in free energy and the diversity of the CRR shapes.[15] In contrast, β-relaxation is found to originate from local rearrangements of the larger "solvent atoms" in metallic glasses.[19] Thus β-relaxation is a less collective dynamics than α-relaxation, and the only residual dynamics that happens below T_g in the bulk glass. Despite of the difficulties and discrepancies, several common behaviors of β-relaxation have been observed. For example, the temperature dependence of β-relaxation below T_g is Arrhenius[2] (Fig. 1.3) with an activation barrier of ~ 10 $k_B T_g$.[15] In contrast to α-relaxation,

CRRs for β-relaxation have a string-like shape.[15] More investigations are required to unambiguously determine whether β-relaxation is non-exponential and non-ergodic.

1.3. Surface glass dynamics

Surface glass dynamics is even less understood than bulk dynamics, both experimentally and theoretically. Relaxations on the free surface of glasses are not necessary similar to the bulk. In fact, it deviates significantly from the bulk behavior.

On the glass surface, the classification of α- and β-relaxations is not as clear as in the bulk. One of the reasons is the different temperature dependence of the surface relaxation.[20,21] Fig. 1.4 shows an example of temperature dependence of surface relaxation in comparison with the bulk for polystyrene.[20] The surface relaxation time is similar to the bulk α-relaxation time near the bulk T_g. However, below T_g the surface relaxation is much faster than the bulk α-relaxation, but slower than β-relaxation. The temperature dependence of surface relaxation is much weaker than the bulk α-relaxation and often an Arrhenius dependence is observed[20,22] which is similar to β-relaxation.[2] This enhanced surface mobility results from reduced constraints on the free surface. Theory predicts that activation barrier for α-relaxation is reduced by a factor of 2 on the surface,[23] thus the surface has much higher mobility than the bulk. Enhanced surface mobility also manifests as a lower surface T_g compared to the bulk T_g.[24] In contrast, higher surface T_g is also sometimes observed, mainly because of strong interaction of the glassy layer with the substrate.[25]

The shape of surface CRRs may also be different from the bulk. Theory predicts that, the surface CRRs for α-relaxation have a compact shape, similar to the bulk.[23] Our study shows that surface CRRs for β-relaxation also have a compact shape, in contrast to the bulk.[26] This will be discussed in Chapter 2.

Surface glassy dynamics is heterogeneous.[27-30] Spatial heterogeneity is more dominant as observed on metallic glass surfaces.[31] However, both exponential[20] and non-exponential[31] behaviors have been observed for surface relaxations. Ergodicity has not been investigated for surface glass dynamics.

1.4. Scanning tunneling microscopy

Scanning tunneling microscopy (STM) is employed to investigate surface glassy dynamics at sub-nm resolution. STM operates on the quantum tunneling phenomenon in which electrons tunnel quantum mechanically through the vacuum gap between a conducting tip and a conducting or semiconducting sample when the separation is in the order of ~ 1 nm.[32,33] The tunneling current is established by applying a bias voltage to the sample and keeping the tip grounded. In one-dimension case at low voltage, the tunneling current depends linearly on the local density of states of the surface being probed and exponentially on the separation between the tip and the sample.[33,34] The tunneling current is given by:[33]

$$I_t \sim \rho e^{-2\kappa z} \tag{1.4}$$

and

$$\kappa = \frac{\sqrt{2m_e\phi}}{\hbar} \tag{1.5}$$

where I_t is the tunneling current, ρ is the local density of states of the probed area which is set by the sample bias voltage, *z* is the separation between the tip and the sample, m_e is the mass of the electron, $\hbar$ is the reduced Planck constant and ϕ is the average work function of the tip and the sample. Given the typical value of the work function ϕ of ~ 4 eV,[33] κ is in the order of ~ 10 nm^{-1}. Thus the tunneling current is reduced by one order of magnitude when the separation between the tip and the sample is increased by just 0.1 nm. This exponential dependence explains the ultrahigh resolution of STM in *z* direction. Resolution better than 0.1 nm is routinely achieved.[32,33]

STM can be operated in two modes based on Eq. 1.4. The first one is constant height mode in which the height of the tip is kept constant in the *z* direction and I_t is monitored. This mode is rarely used because large changes in topography will cause the tip to crash into the surface. The second one is constant current mode and is much more often used. The tunneling current, I_t, is kept constant and the *z* position of the tip is monitored. Up and down motion of the tip reflects the local density of states available for tunneling on the surface, which may differ from surface topography given by van der Waals repulsion (as obtained from atomic force microscopy).

In Eq. 1.4, the tunneling current is proportional to the local density of states. Thus STM is widely used to measure the density of states of the surface. This technique is called scanning tunneling spectroscopy (STS).[33] In STS, the tip is held at constant separation from the surface and the tunneling current is measured as a function of the sample bias voltage. The resulting I-V curve and its derivative dI/dV-V provide information about density of states and electronic structures of the surface.

We use a homebuilt ultrahigh vacuum STM in our experiments with based pressure $\leq 7 \times 10^{-9}$ Pa.[35] The lateral drifting rate is $\leq$ 0.1 nm/h. This ultrahigh stability is crucial in for observing surface glassy dynamics in an extended period of time.

1.5. Figures

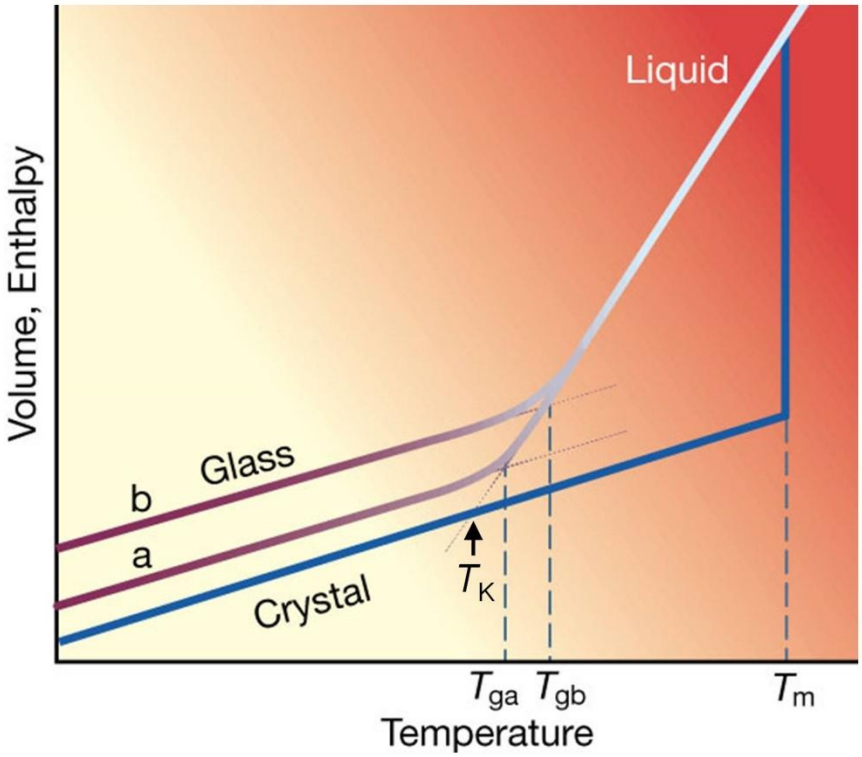

Figure 1.1: Temperature-dependence of enthalpy or volume of a liquid at constant pressure. When a liquid is cooled slowly, a crystal is formed at the melting temperature T_m. Fast cooling rate avoids crystallization and a glass is formed at T_{ga-b}. The cooling rate in curve b is faster than in curve a. Kauzman temperature is extrapolated from the supercooled liquid regime. Adapted by permission from Macmillan Publishers Ltd: NATURE[2], copyright 2001.

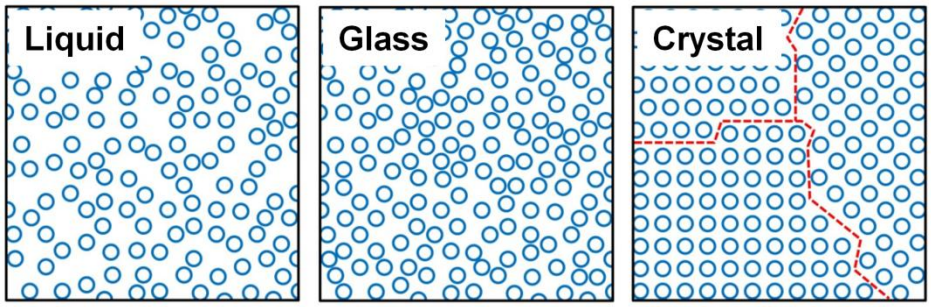

Figure 1.2: Schematic structures of liquid, glass and crystal. Glass has a random structure similar to liquid, but with higher density.

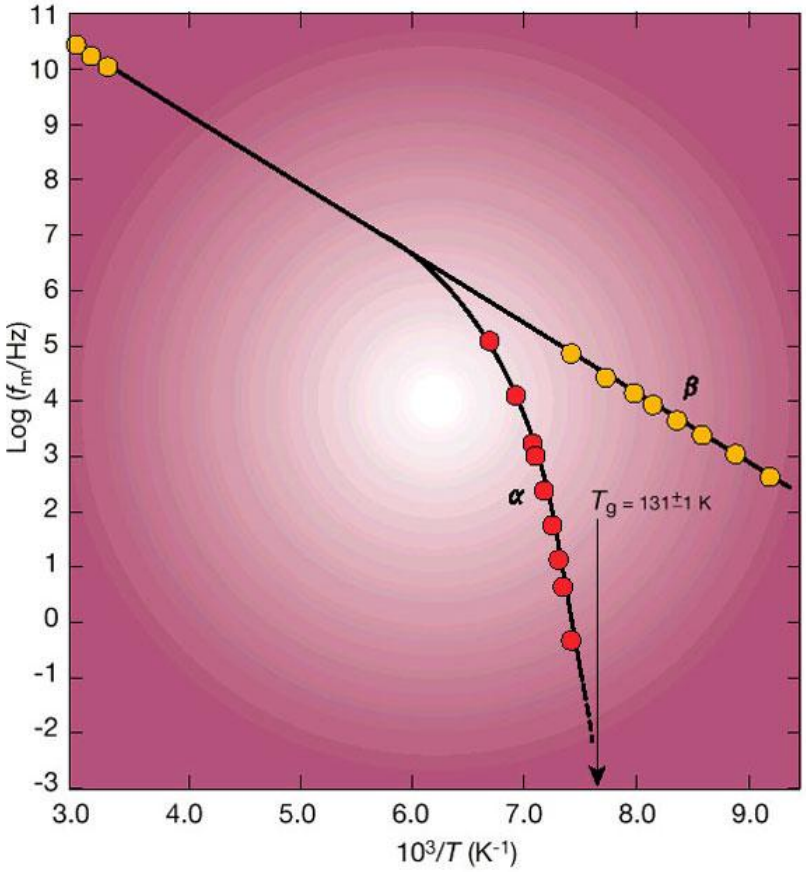

Figure 1.3: Temperature-dependence of the peak dielectric relaxation frequency (or inverse relaxation time) of the glass former cholorobenzene/cis-decalin (17.2 : 82.8). Adapted by permission from Macmillan Publishers Ltd: NATURE[2], copyright 2001.

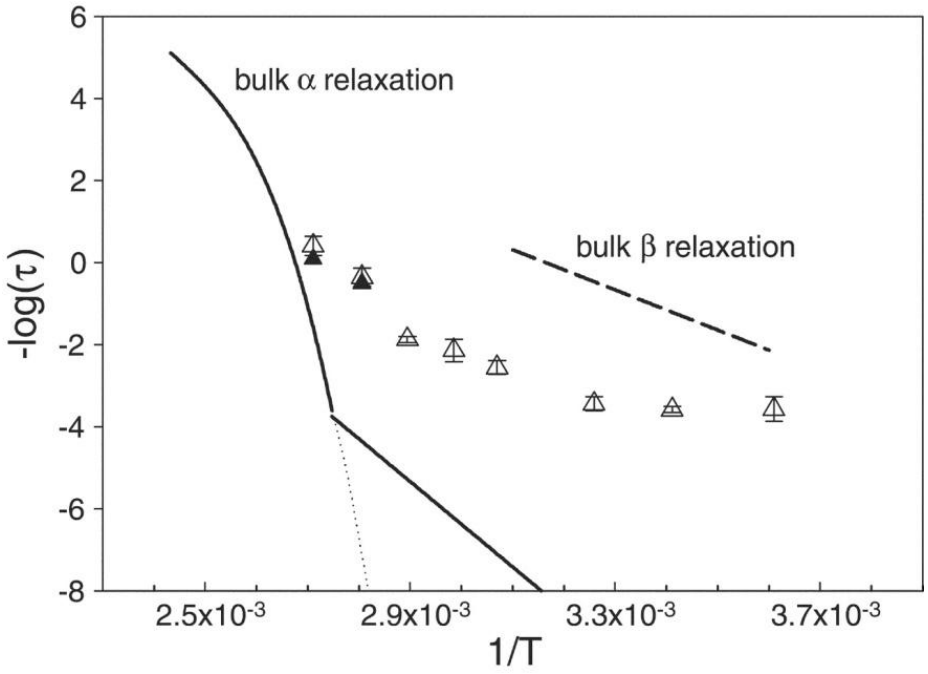

Figure 1.4: Surface relaxation times (open and filled triangles) for polystyrene in comparison with bulk α-relaxation times (solid curve) and β-relaxation times (dashed curve). $1/T_{g,bulk}$ ~$2.75x10^{-3}$ K^{-1}. Figure is adapted from ref. 20. Reprinted with permission from AAAS.

1.6. References

1. E. Axinte, Mater. Des., 35, 518–556 (2012).
2. P. G. Debenedetti and F. H. Stillinger, Nature, 410, 259–267 (2001).
3. F. H. Stillinger, Science, 267, 1935–1939 (1995).
4. L. Berthier and G. Biroli, Rev. Mod. Phys., 83, 587–645 (2011).
5. A. L. Greer, Science, 267, 1947–1953 (1995).
6. P. W. Anderson, Science, 267, 1615–1616 (1995).
7. V. Lubchenko and P. G. Wolynes, Ann. Rev. Phys. Chem., 58, 235–266 (2007).
8. W. Kauzmann, Chem. Rev., 43, 219 (1948).
9. T. R. Kirkpatrick, D. Thirumalai and P. G. Wolynes, Phys. Rev. A, 40, 1045–1054 (1989).
10. C. A. Angell, Science, 267, 1924–1935 (1995).
11. L.-M. Wang, C. A. Angell and R. Richert, J. Chem. Phys., 125, (2006).
12. M. T. Cicerone, F. R. Blackburn and M. D. Ediger, J. Chem. Phys., 102, 471 (1995).
13. U. Tracht, M. Wilhelm, A. Heuer, H. Feng, K. Schmidt-Rohr and H. W. Spiess, Phys. Rev. Lett., 81, 2727–2730 (1998).

14. L. Berthier, G. Biroli, J. P. Bouchaud, L. Cipelletti, D. El Masri, D. L'Hote, F. Ladieu and M. Pierno, Science, 310, 1797–1800 (2005).
15. J. D. Stevenson and P. G. Wolynes, Nat. Phys., 6, 62–68 (2010).
16. A. Deres, G. A. Floudas, K. Müllen, M. Van der Auweraer, F. De Schryver, J. Enderlein, H. Uji-i and J. Hofkens, Macromolecules, 44, 9703–9709 (2011).
17. P. Lunkenheimer, S. Kastner, M Kohler and A. Loidl in Structural Glasses and Supercooled Liquids: Theory, Experiment, and Applications, ed. V. L. Peter G. Wolynes, Wiley, First., pp. 115–150 (2012).
18. H.-B. Yu, W.-H. Wang and K. Samwer, Mater. Today, 16, 183–191 (2013).
19. Y. H. Liu, T. Fujita, D. P. B. Aji, M. Matsuura and M. W. Chen, Nat. Commun., 5, 3238 (2014).
20. Z. Fakhraai and J. A. Forrest, Science, 319, 600–604 (2008).
21. Y. Chai, T. Salez, J. D. McGraw, M. Benzaquen, K. Dalnoki-Veress, E. Raphaël and J. A. Forrest, Science, 343, 994–9 (2014).
22. Z. Yang, Y. Fujii, F. K. Lee, C.-H. Lam and O. K. C. Tsui, Science, 328, 1676–1679 (2010).
23. J. D. Stevenson and P. G. Wolynes, J. Chem. Phys., 129, 234514 (2008).
24. J. S. Sharp and J. A. Forrest, Phys. Rev. Lett., 91, 235701 (2003).
25. C. J. Ellison, R. L. Ruszkowski, N. J. Fredin and J. M. Torkelson, Phys. Rev. Lett., 92, 095702 (2004).
26. D. Nguyen, J. Mallek, A. N. Cloud, J. R. Abelson, G. S. Girolami, J. Lyding and M. Gruebele, J. Chem. Phys., 141, 204501 (2014).
27. S. Ashtekar, G. Scott, J. Lyding and M. Gruebele, J. Phys. Chem. Lett., 1, 1941–1945 (2010).
28. S. Ashtekar, G. Scott, J. Lyding and M. Gruebele, Phys. Rev. Lett., 106, 235501 (2011).
29. H. K. Nguyen, D. Wang, T. P. Russell and K. Nakajima, Soft Matter, 11, 1425–33 (2015).
30. Y. H. Liu, D. Wang, K. Nakajima, W. Zhang, A. Hirata, T. Nishi, A. Inoue and M. W. Chen, Phys. Rev. Lett., 106, 125504 (2011).
31. S. Ashtekar, J. Lyding and M. Gruebele, Phys. Rev. Lett., 109, 166103 (2012).
32. G. Binnig, H. Rohrer, C. Gerber and E. Weibel, Phys. Rev. Lett., 49, 57–61 (1982).

33. C. J. Chen, Introduction to scanning tunneling microscopy, Oxford University Press, Oxford, (1993).
34. J. Tersoff and D. R. Hamann, Phys. Rev. B, 31, 805–813 (1985).
35. J. W. Lyding, S. Skala, J. S. Hubacek, R. Brockenbrough and G. Gammie, Rev. Sci. Instrum., 59, 1897–1902 (1988).

2. The energy landscape of glassy dynamics on the amorphous hafnium diboride surface

This chapter is reproduced from D. Nguyen, J. Mallek, A. N. Cloud, J. R. Abelson, G. S. Girolami. J. Lyding and M. Gruebele, The energy landscape of glassy dynamics on the amorphous hafnium diboride surface, *J. Chem. Phys*., 2014, 141, 204501, with the permission of AIP Publishing.

2.1. Abstract

Direct visualization of the dynamics of structural glasses and amorphous solids on the sub-nanometer scale provides rich information unavailable from bulk or conventional single molecule techniques. We study the surface of hafnium diboride, a conductive ultrahigh temperature ceramic material that can be grown in amorphous films. Our scanning tunneling movies have a second-to-hour dynamic range and single-point current measurements extend that to the millisecond-to-minute time scale. On the a-HfB_2 glass surface, two-state hopping of 1–2 nm diameter cooperatively rearranging regions or "clusters" occurs from sub-milliseconds to hours. We characterize individual clusters in detail through high-resolution (<0.5 nm) imaging, scanning tunneling spectroscopy and voltage modulation, ruling out individual atoms, diffusing adsorbates, or pinned charges as the origin of the observed two-state hopping. Smaller clusters are more likely to hop, larger ones are more likely to be immobile. HfB_2 has a very high bulk glass transition temperature T_g, and we observe no three-state hopping or sequential two-state hopping previously seen on lower T_g glass surfaces. The electronic density of states of clusters does not change when they hop up or down, allowing us to calibrate an accurate relative z-axis scale. By directly measuring and histogramming single cluster vertical displacements, we can reconstruct the local free energy landscape of individual clusters, complete with activation barrier height, a reaction coordinate in nanometers, and the shape of the free energy landscape basins between which hopping occurs. The experimental images are consistent with the compact shape of α-relaxors predicted by random first order transition theory, whereas the rapid hopping rate, even taking less confined motion at the surface into account, is consistent with β-relaxations. We make a proposal of how "mixed" features can show up in surface dynamics of glasses.

2.2. Introduction

Understanding the structural transformation of an atomic or molecular liquid into glass is considered one of the grand challenges of chemical physics. Although some structural insights have been provided by simulations despite their limited time scale and finite size,[1,2] and direct observations on colloids as macroscopic glass analogs give structural information,[3,4] laboratory experiments that resolve structure and dynamics at or near the atomic level in structural glasses are still scarce.[5–7] What is the shape of the cooperatively rearranging regions in glasses and what does their free energy landscape look like? These are questions we would like to answer quantitatively here.

Simple mode coupling theories predict that upon cooling a glass-forming liquid, the liquid-phase diffusion time scale lengthens and ultimately diverges.[8,9] Below the temperature T_c, instead a rapidly slowing process does occur, signaling the emergence of activated events. Experiments show that the slower α-relaxation process appears to "freeze out" below the glass-transition temperature T_g, where the rapidly increasing glass viscosity precludes further observations of macroscopic change on the laboratory time scale.[10] Motion still does occur. β-relaxations, faster than the α process, can be observed even below T_g in the bulk,[10] and are associated with motions on a more local scale than α-relaxation.[11] Nevertheless, it is clear based on experiments[12,13] and modeling[14,15] that the "global" α-relaxation and the "local" β-relaxation are both collective and connected to one another.[16,17] Ideas about this structural connection have been untested because atomic level structural detail has been unavailable on the laboratory time scale, while atomic level simulations on the ms or longer time scale remain a decided luxury.[18]

Two kinds of approaches have been explored for structural dynamics of glasses. In themodynamically motivated theories such as random first order transition theory (RFOT),[19] the collective α-relaxation occurs through structurally compact, collectively moving clusters that increase in size as the glass is aged (i.e., as the experiment allows more relaxation time when $T \approx T_g$).[19] In the bulk, the RFOT distribution of enthalpic barriers for α-relaxation peaks at $\sim 30–36 k_B T_g$,[15] for fragile glasses, but is smaller for strong glasses (fragility describes how quickly the liquid viscosity is recovered upon heating a glass[20]). Beneath T_g, the clusters get stuck below barriers roughly proportional to the cluster surface area, and hop at best between two states, or most likely do not hop at all. Within the RFOT picture, β-relaxations correspond to more elongated strings of glass forming units[15] (the units being SiO_2 for window glass, a pair of

atoms for a bimetallic glass, or a HfB_2 unit for hafnium diboride). These strings can move among the α-cooperatively rearranging regions and have a much lower barrier distribution, peaked at $\sim 10\, k_B T$ in the RFOT model.[15] The other approach involves kinetic facilitation of "stuck" regions in the glass. In some kinetic facilitation models,[21] local relaxation also corresponds to string-like chains of glass-forming units. These structures can facilitate motion of similar structures of glass formers nearby in the glass matrix, relieving strain, and are thought to lead to global relaxation without compact regions.[22] Both models connect local to global relaxation structurally, but in different ways: in RFOT there is a distribution of shapes of cooperatively rearranging units from compact to elongated, and a distribution of activation barriers that can range from bimodal (β peak and α peak) to just a single dominant peak;[15] in kinetic facilitation, different local rearranging regions interact to facilitate large scale collective structural rearrangements in the glass.[4,22]

Experiments deep in the glassy regime are difficult because slow dynamics tests the experimentalist patience. α-relaxation dynamics is not observable below T_g in the bulk because such events become exceedingly rare: $k(\alpha) \approx 10^{11} e^{-30/(3/4)}\ s^{-1} \approx 4$/year for a low-barrier glass at ¾ of the glass transition temperature. The RFOT theory predicts that on the glass surface, the activation barrier is only half that of the bulk, or 15–18 $k_B T_g$.[23] That brings α-relaxation much closer to the β-relaxation time scale, making it potentially observable at surfaces.

Experiments can directly visualize the motion of cooperatively rearranging regions in structural glasses or amorphous solids when spatial resolution at the level of a single glass forming unit (<0.5 nm) is combined with accelerated glassy dynamics at surfaces.[6,24–26] Like single molecule experiments, such "single cooperatively rearranging region" experiments can make rare slow dynamics visible even against an immense background of immobile glass matrix. We previously imaged dynamics on surfaces of metallic glasses[24] and amorphous silicon[6] by time-resolved scanning tunneling microscopy with <90 s time resolution and <0.5 nm spatial resolution, sufficient to resolve sub-structure in cooperatively rearranging regions. Structural dynamics of a glassy surface is not necessarily identical to that in the bulk, but the ability to directly access the surface motion encourages their comparison with glass theories modified to correct for surface effects.[23] In our experiments we have observed compact clusters of between 3 and 8 glass forming units in width that hop between two structural states at $T \ll T_g$. Hopping clusters are rare compared to immobile clusters. Occasionally, we observed even rarer three-state

motion or concerted two-state motion (where a cluster hops, and soon thereafter another nearby cluster hops).[6,26] The shape of glass surface clusters is more in line with the prediction of RFOT theory for α-cooperatively rearranging regions, while their speed is more in line with the β-relaxation time scale. However, given the much greater number of immobile clusters on the glass surfaces we studied, the ones that move may correspond to the low barrier tail of the activation barrier distribution.[23]

Here we aim to answer the questions posed in the introductory paragraph – What are the shapes and free energy landscapes of cooperatively rearranging regions at the surface of glasses? We do this for the chemical vapor deposited amorphous hafnium diboride surface well below its bulk glass transition temperature. (HfB_2 has a melting temperature $T_m \approx 3200$ K[27] and $T_g \approx 0.6T_m$.[28]) We extend our accessible time scale by a factor $>10^5$ over our past work, by complementing full image scans of the surface (~90 s/frame) with small-image scans (~0.1 s resolution) and single point time traces of cooperatively rearranging regions (~0.1 ms time resolution). We also study the cooperatively rearranging regions at atomic resolution and measure their I–V characteristics to show that they correspond with collectively moving groups of atoms, not to individual atoms or to small molecules diffusing on the surface. Finally, we are able to histogram the glassy surface dynamics to construct quantitative free energy landscapes as a function of vertical displacement from the surface.

In our experiment-based picture of glassy surface dynamics, HfB_2 cooperatively rearranging regions are compact clusters of a few glass-forming units in diameter that move ~0.08–0.12 nm between two structural states. The states are separated by a low barrier (~25 k_BT in room temperature units, 4 k_BT_g in glass transition temperature units) defined by our time window from 0.1 ms to a few hours. We find that immobile clusters have a similar local free energy landscape, but lack access to a second free energy well. Rarity of moving clusters is explained easily: motion corresponds to a collective breaking and making of bonds and dangling bonds at the cluster surface; only a few clusters can move while preserving the net number of bonds and dangling bonds in product and reactant. Clusters that are not nearly thermoneutral are trapped in minima so deep, that they cannot be observed to hop reversibly on our time scale. We do not observe string-like cooperatively rearranging regions in our experiments, although we have the spatial resolution needed to observe them; if "stringy" dynamics is faster than we can

resolve, or if such motions are even rarer than compact clusters, we would not be able to observe it.

We conclude with simulations based on a surface-modified RFOT model, showing that the structural dynamics we observe (cooperatively rearranging regions are compact) and free energy landscapes (rough double wells) are consistent with an RFOT model that has been modified to fit the special feature of a free surface. The model yields α- and β-relaxations having barriers peaked at 10–15 $k_B T_g$, with tails down to a few $k_B T_g$. These barriers are consistent with experiment if we assume that we are observing the low-barrier tail of the activation energy distribution in our time window. Thus, the existence of compact cooperatively rearranging regions moving on an accelerated time scale due to reduced surface friction between two states on a glassy surface seems to be settled by these observations.

2.3. Experimental and computational methods

HfB_2 amorphous thin films were grown by chemical vapor deposition (CVD) on both *n*- and *p*-type silicon (100) substrates (0.01–0.02 Ω·cm resistivity), using $Hf[BH_4]_4$ as a precursor.[29] CVD growth onto a low temperature substrate molecule-by-molecule avoids the presence of any crystalline patches. The precursor was kept at room temperature while the substrate temperature was below 500 °C ($\ll T_g < T_m$) during deposition. The base pressure was below 1 Pa before deposition and ~2000 Pa during the CVD growth. After degassing at ~110 °C for 9–15 h, HfB_2 was cleaned using 2 keV argon ion sputtering for 2–4 h with a dose of ~(1–10) × 10^{16} ions/cm^2. The base pressure of the sputtering chamber was ~2 × 10^{-6} Pa and argon was backfilled to ~3 × 10^{-3} Pa. After sputtering, the samples were immediately transferred to the attached UHV STM chamber to record surface dynamics. X-ray photoelectron spectroscopy showed that the surfaces, of average composition $HfB_{1.55}$ as a result of preferential sputtering, were not contaminated with silicon, and SEM showed that the glassy films were 46–101 nm thick, corresponding to ~130–290 layers of HfB_2 (see Fig. 2.10 in the supplementary material[30]).

We acquired STM topography movies of the surface, and tunneling current traces of individual cooperatively rearranging regions as a function of time, using a home-built ultrahigh vacuum STM[31] with base pressure ≤7 × 10^{-9} Pa and with a thermal drift of <0.1 nm/h. Series of STM images were collected using constant current mode and are presented as topography (piezo *z*-displacement) or spatial derivative images for better contrast of cooperatively

rearranging region dynamics. These STM movies had a time resolution of ~ 90 s, and a maximum duration of several hours. Some movies achieved atomic or near-atomic resolution. We also collected tunneling current *vs.* time traces of individual sites on the surface in constant spacing mode. Due to the current preamplifier band width of 10 kHz, our ultimate time resolution is about 100 μs. Traces were collected with time steps as short as 16.5 μs and up to 33 s in overall duration (see the supplementary material).[30] Thus we were able to capture dynamics from the sub-millisecond to the hour time scale.

HfB_2 is a metallic solid, so we collected I–V traces to verify the nature of both mobile and immobile regions on the glass surface and to check that tunneling characteristics remained unchanged in the course of the observed dynamics. Unchanging tunneling characteristics over a region allowed us to obtain a quantitative distance calibration. To calibrate the reaction coordinate of the energy landscape, a z distance *vs.* tunneling current calibration curve was measured by ramping the current and measuring displacement of the tip piezo from constant height (see the supplementary material).[30] The calibration was confirmed to be accurate to within 2% by comparison with step edges on Si(100) and graphene surfaces (see the supplementary material).[30]

RFOT theory has been modified to make predictions for glassy surface dynamics.[23] To model structural dynamics, free energy barrier distributions were generated using the disordered fuzzy-sphere model of Stevenson *et al.* based on RFOT theory.[14] First, a two-dimensional free energy surface was calculated as functions of the number of particles in the core and the number of particles in the fuzzy halo, following Eq. (10) in Ref. 14. Random fluctuations in free energy were then added in which the strength of fluctuation depends on fragility, as $T\,(\Delta C_p\, k_B)^{0.5}$ where fragility $m = 20.7\,\Delta C_p$.[15] For a-HfB_2, we used a fragility $m \approx 30$ which is typical for inorganic glass-forming materials.[32] To account for the free surface effects, the effective surface area of the core was reduced by a factor of 2, which is consistent with the proposed modification of RFOT theory for glassy surfaces.[23] The disordered free energy calculation was repeated 100 000 times to obtain a distribution of lowest free energy barriers for stable reconfigurations.

2.4. Results

2.4.1. Characterizing individual cooperatively rearranging regions: Size, shape, sub-structure and electronic properties

Fig. 2.1(a) shows frames from a STM topographic movie illustrating the glassy surface dynamics we observed. In this movie the cooperatively rearranging region is a two-state cluster of multiple atoms that is initially slow (transitions occur between frames), that then becomes fast later in the sampled time window (multiple transitions within a frame). The cluster can be resolved clearly in topography mode. In Fig. 2.1(b), the corresponding spatial derivative images are shown. In the derivative mode, "low" and "high" regions of the surface are all visible equally. Thus, derivative mode provides a wider range and better visualization of all clusters while keeping the cluster shape, position, and state unchanged. All STM images are presented in the derivative mode except for Fig. 2.1(a). One of the smallest features resolved in Fig. 2.1(b) (dashed circle) has a diameter of 0.4 nm, the size of a single HfB_2 (0.34 nm[27]) glass forming unit. This length scale defines the upper limit on the lateral broadening and resolution of the STM scan. In this movie as in others, hopping clusters are at least twice as large (1 nm = 3 glass forming units), and usually four to five times larger (Fig. 2.1(c)). Thus clusters are easily distinguished from small molecules or individual atoms.

Fig. 2.1(c) shows the size distributions for hopping and non-hopping clusters. The (peak) average diameters for hopping and non-hopping clusters are (4.0) 4.8 ± 1.2 and (5.0) 5.3 ± 1.8 glass forming units and the standard deviations of the size distributions are σ = 1.2 and 1.8. The hopping clusters are slightly smaller than non-hopping clusters. This result agrees with the intuition that smaller cooperatively rearranging regions should be able to move more easily than larger cooperatively rearranging regions. The larger non-hopping clusters are not necessarily devoid of dynamics; they may hop on a time scale slower than our few hour observation window.

Clusters observed to hop have $K_{eq} \approx 1$ (roughly equal time spent up *vs*. down), thus hopping cannot involve the net closure of dangling bonds or breaking of bonds into dangling bonds, which would be irreversible one-time events (net bond making), or far too endoergic to be observed (net bond breaking). Clusters therefore rearrange by bond breaking and formation that is net nearly neutral in free energy. The great majority of clusters are non-hopping clusters,

which apparently do not have a neutral free energy path at their disposal. We observed only ~0.2% of all clusters moving on our experiment time scale of a few hours or less.

Fig. 2.2(a) shows a two-state cluster with resolved substructure. In addition to having a diameter much larger than the lateral resolution, the substructure of the image reveals that the clusters are collection of atoms, not single atoms or molecules, consistent with our previous study on a metallic glass surface.[26] As the cluster in Fig. 2.2 hops between the same two states, its shape and orientation between hops remains the same in each state. The buckling of a single dangling bond is also position and orientation conserved.[33] Nevertheless, the substructure and size of moving clusters in equilibrium between two states indicates that they are a collection of atoms bonded into a collective structure. The observation of substructure also excludes the possibility that the observed motions are caused by diffusion of a small adsorbate in and out of a favorable site, and I–V curves discussed below further exclude this possibility.

While the diffusion of the smallest constituent atoms in metallic glasses at a similar temperature has been shown to involve string-like cooperatively rearranging regions,[34] we exclusively observed two-state dynamics of compact clusters (aspect ratio ≤ 2) on the surface. The dynamics does not involve the diffusion of the smaller B atoms. It is also worth noting that XPS showed that the boron atoms are not in excess on the surface (1:1.55 stoichiometry), and thus most likely all remain bound to hafnium.

When an STM tip scans over the surface, injected electrons can form stable charge defects. These would show up as a large difference in surface topography when the bias voltage is reversed.[35] Fig. 2.2(b) is a movie taken under successive voltage reversals. The cluster shape and hopping speed do not change when the polarity is reversed, indicating that the observed dynamics is not caused by a charged defect. The cluster in Fig. 2.2(b) is also imaged at tunneling current 10 times smaller than the cluster in Fig. 2.2(a), but its hopping rate is substantially faster. Hopping does not increase with tunneling current and the dynamics is independent of tunneling voltage switching. Movies such as those in Fig. 2.2 show that cluster hopping is structural dynamics, not caused by charging effects.

We also measured I–V curves (scanning tunneling spectroscopy = STS). Fig. 2.3(a) shows what is either a two-state cluster hopping laterally on the glass surface, or two adjacent clusters hopping in anti-correlated motion up and down. Fig. 2.3(b) is the I–V curve measured on top of the cluster(s) shown in Fig. 2.3(a) in state "1" and in state "0." Both scans are

characteristically metallic with nearly identical I–V curves, proving that the local densities of electronic states of the cluster are similar in the two states. The metallic nature of several clusters observed by STS provides additional evidence that the hopping clusters are not adsorbates and that the dynamics is not caused by diffusion or charging effects. Even more importantly, because there is no change in electronic structure upon hopping, the measured tunneling current directly relates to the height of the cluster, and we will make use of this fact in Sec. 2.4.3.

2.4.2. A wide range of hopping rates on the a-HfB_2 surface

We have seen in Figs. 2.1–2.3 that clusters can hop several times as they are being scanned, not just between frames of the STM movies. The very fastest clusters appear as noisy speckles and little can be deduced about their kinetics from the full-image STM movies. Previously we did not study them in detail because few were observed and the time resolution was limited: it takes at least a minute to acquire an image.

To resolve fully the hopping dynamics of fast clusters, we first scanned a frame several times to make a time-lapse movie identifying a repeatedly hopping cluster (an example featuring a slow-hopping cluster is circled in Fig. 2.4(a)). Then, during such a scan, we stop the STM tip on top of the cooperatively rearranging region (red dot), turn off the feedback loop, and measure tunneling current as a function of time at constant tip height. The time required to sample a current point is $\geq 16.5\ \mu$s, with an amplifier bandwidth-limited time resolution of 0.1 ms. We can measure up to 33 s for such a single-point current trace before the tip begins to drift laterally from the cluster being probed. Our dynamic time range is thus improved over our previous work by a factor of $>10^5$. As a cluster hops out of the surface, the tunneling current increases and then decreases when that cluster drops back in. After measuring the tunneling current, we revert to full scans to continue imaging the area and sample the cluster further in full imaging mode (last frame in Fig. 2.4(a)). Fig. 2.4 illustrates that clusters always start in the same state during the movie, where they were at the end of a single-point trace, so the fast hopping while the tip is stopped always correlates with the slow hopping, and thus reflects the same dynamical phenomenon.

We also pushed the scanning procedure to its temporal limit by scanning small areas $\leq$2 clusters in diameter, leading to a time resolution of $\sim$ 5 s/frame of STM movie. The hopping clusters occupy a large fraction of the scanning areas ($\geq$ 50%), therefore we can assume that the

clusters rarely hop during the times they are not being imaged, if they do not hop during the periods they are being imaged. The height profile vertically across the cluster gives us the state trace of the clusters with improved time resolution (~100 ms/line). Thus we have three scan modalities: survey scans at ≥ 60 s/frame, small area scans at ~100 ms/line, and fast single-point detection with sub-ms time resolution. The time scale is thus limited at one end by instrument response and the other end by the life time of the STM tips.

A wide range of two-state dynamics on the a-HfB_2 surface was observed. Fig. 2.5(a) shows a cluster that never hops, but fluctuates around its local position, as captured by the tunneling current in Fig. 2.5(b). Fig. 2.5(c) is a slow cluster that hops in and out in complete scans in hundreds of minutes, with a complete time trace shown in Fig. 2.5(d). Fig. 2.5(e) shows a fast cluster resolved by scanning a single small area. From the height profile, we reconstructed its two-state trace, as plotted in Fig. 2.5(f). Fig. 2.5(g) shows a fast cluster hopping in and out several times in one frame. The tunneling current measured at a single point on top of this cluster shows two-state behavior with multiple hops in a 20 s time window with time resolution of 33 ms/point (Fig. 2.5(h)).

In this system, we observed only two-state hopping, although evidence of a minor fraction of three-state hopping and correlated sequential hopping was reported previously on other glass surfaces.[6,24,26] The lack of any multi-state or diffusive dynamics is consistent with the expected high T_g of HfB_2 surfaces (based on the bulk), putting our observations of this material near room temperature even more deeply below the glass transition than other polymer,[5] metallic[24] or semiconducting glass surfaces[6] that have been observed. On polymer surfaces studied by AFM, similar glassy two-state dynamics was observed.[13]

2.4.3. Constructing a single-cluster energy landscape

Having characterized the clusters in detail and accumulated many two-state current traces from clusters with a variety of hopping rates, we pursued our main goal of extracting a quantitative free energy profile for individual cluster dynamics from the experimental data. This requires three steps. (1) Calibration of the current *vs.* z distance yields a quantitative coordinate for describing cluster motion along the surface normal in nanometers. (2) The shape and free energy of each well is determined by histogramming the distribution of cluster z-coordinates and then calculating the potential of mean force from the normalized histogram $H(z)$ as $-k_BT\ln(H(z))$.

(3) Determination of the Arrhenius prefactor $\nu^{\dagger}$ from temperature-dependent hopping, which then fixes the barrier height $\Delta G^{\dagger}_{01}=k_B T\ln(\tau_{dwell}/\tau^{\dagger})$; we use the value of $\nu^{\dagger} = (\tau^{\dagger})^{-1} = 6 \times 10^{10}\ \mathrm{s}^{-1}$, determined experimentally by us for similar-sized clusters by measuring the temperature dependence of their activation energy.[26] This leaves only the curvature (second derivative of the free energy) of the transition state undetermined.

As discussed in Sec. 2.4.1., the electronic character of the clusters is identical in both states. Thus changes in tunneling current directly translate into changes in vertical distance. To calibrate the *z*-separation between the two different states visited by hopping, we measured the tip-sample distance change as a function of tunneling current for various hopping and non-hopping clusters (Fig. 2.6(a)). The calibration of our STM piezo was verified by measuring an average Si(100) step height of 0.134 ± 0.001 nm (literature value: 0.136 nm; the ± value is the precision of the average, better than any individual measurements). Fig. 2.6(b) is the *z*-*I* calibration curve for a hydrogen passivated Si (100)-2 × 1 surface for comparison. Distance was calibrated with equally good results on graphenized SiC (see the supplementary material).[30]

Fig. 2.7(a) compares the two-state hopping for a fast cluster in HfB_2 with a similar measurement on the crystalline hydrogen passivated Si(100):2 × 1 surface with the same scanning parameters. The calibrated distance trace is shown in red. In addition to the large jumps in current due to hopping between two states, there are smaller fluctuations in tunneling current through individual clusters on the a-HfB_2 surface. These smaller fluctuations are reproducibly ten times larger than those seen on the Si surface (Fig. 2.6(a)). This observation suggests that there is additional cluster motion on faster time scales but with smaller amplitude within each of the two states. Fig. 2.7(b) is the histogram of the complete z trace for the cluster from Fig. 2.5(g). To make certain that the distance distribution within the individual free energy wells is due to actual dynamics and not instrument noise, we measured the instrument noise. Fig. 2.7(a) already shows that the intrinsic *z* noise, measured on a non-hopping Si surface, is much lower than the observed in-state fluctuations. In addition, Fig. 2.7(c) plots the root mean square deviation (RMSD) of cluster motions on a-HfB_2 within a single state, and of the noise background on Si(100) as a function of the averaging time window (from < 0.1 ms to >10 ms). In contrast to the decreasing noise with increasing time window on the Si surface (blue data points and dashed curve in Fig. 2.7(c)), the RMSD for a cluster within a single state is much larger and essentially

independent of time averaging window up to 33 ms, confirming that there is in-state motion on the time scale ~ 33 ms or longer causing fluctuations in tunneling current.

The histogram in Fig. 2.7(b) yields the shape of the free energy landscape projected along the *z*-axis near the two minima, where sampling is good. Fig. 2.7(d) shows the experimentally determined free energy profile of the cluster in Fig. 2.5(g). The separation of free energy minima along the *z*-reaction coordinate is δz_{01} = 0.07 nm. The free energy difference between the two minima is $\Delta G_{01} = 0.26\, k_B T$, and the barrier height obtained from the dwell times in Fig. 2.5(g) is $\Delta G^{\dagger}_{01} = 23.6 k_B T \approx 3.7 k_B T_g$. Fig. 2.15 in the supplementary material shows free energy profiles for additional clusters.[30] The RMSD for hopping clusters and for stationary clusters is similar (Figs. 2.15 and 2.7(c)), suggesting that all clusters on the surface are essentially the same in their basic nature; the stationary clusters simply do not have access to a second low free energy state on the maximum time scale (hours) of our experiment, and therefore jiggle around only in a single free energy well.

The z-axis displacement provides a quantitative description of cluster motion along the free energy profile, but it is clearly not a perfect reaction coordinate. For instance, the in-state dynamics occurs on a time scale $\tau_{micro} \sim 50$ ms, which translates to a barrier height of $k_B T \ln(\tau_{micro}/\tau^{\dagger}) = 21.8\, k_B T$. The "micro" barrier is smaller than the two-state hopping barrier, but it is still much larger than the corrugation within wells in Fig. 2.7(d) and Fig. 2.15 in the supplementary material.[30] Therefore on a one-dimensional free energy profile such as Fig. 2.7(d), the in-well jiggling corresponds to increased friction. This friction is most likely caused by the incipient making and breaking of many local Hf–Hf, Hf–B, and B–B bonds from the cluster to other surrounding clusters on the a-HfB_2 surface. A favorable rearrangement of such bonds then allows the collective motion of Hf and B atoms within a cluster in the vertical direction. Horizontal motion is of course also possible, but is not as sensitively detected by STM.

2.5. Discussion

Glassy surfaces have been shown by Forrest, Ediger and co-workers,[36] and us[24] to have enhanced mobility (either diffusional or two-state). Ediger and co-workers have also exploited this to make particularly well-aged glasses by layered growth,[37] and we have observed direct imaging evidence for such aging on a Ce-based glass surface.[25] We have imaged the structural dynamics of a glassy vapor-deposited HfB_2 surface. As in our previous studies on metallic

glasses and a-Si,[6,24–26] we find that the cooperatively rearranging regions are compact clusters with a mean diameter of 4 glass forming units (mobile on our hours maximum time scale) or 5 glass forming units (immobile on our hours maximum time scale). They hop between two states, or remain stuck in a single state. We characterized the clusters in some detail by scans with ≤0.5 nm lateral resolution, scanning tunneling spectroscopy (I–V curves), and voltage modulation. The rearranging regions undoubtedly are built up from multiple HfB_2 glass forming units. No string-like cooperative motion was observed on the surface on our imaging time scale. We did observe a wide range of two-state rates, fully spanning our time window. This is a strong indication that the actual rate distribution is wide, and the experiment samples only a small window within it. That observation greatly strengthens the notion of a broad distribution of barriers for surface hopping dynamics of compact clusters, which was previously observed in a much smaller time window.[6,24–26]

Those clusters that hop always have an equilibrium constant close to 1 for the two states, indicating that when the cluster motion heals dangling bonds, others are broken to maintain the system nearly thermoneutral. The energy landscape for most clusters on the surface is a single well at low free energy because few cooperative motions allow thermoneutrality to be maintained. For the few two-state clusters, we can map out a free energy surface around each well. There is evidence for barriers ranging from 3.5 to 4.5 $k_B T_g$, although projection along the z coordinate captures only the major hopping barrier, while smaller barrier-limited processes manifest themselves as slow dynamics within the wells due to cluster friction with its glassy environment. In accord with the RFOT proposal of size-dependent friction,[14,23] the mobile clusters are on average smaller in diameter than the immobile clusters. Two-state dynamics was observed previously by Pohl and co-workers at low temperature in the absence of other low-energy excitations;[38] they attributed it to a low density of tunneling of atoms or atom groups in a-Si at low temperature, whereas we attribute our room temperature observations to an activated process.

We can thus propose a simple structural model from our observations. The top view of the unit cell of crystalline HfB_2[27] is shown in Fig. 2.8(a). The unit cell consists of a hexagon of boron atoms and a Hf atom at the middle. We used the size of this unit cell size as the size of a glass forming unit for a-HfB_2. Fig. 2.8(b) illustrates a cross-section of a cluster with diameter of ≈5 glass forming units embedded in the glass matrix, initially at the state "1." We make the

assumption here that the third dimension of the cluster resembles the two that were imaged, i.e., the cluster is spheroidal in shape and not a "buckling pancake" on the surface. As the cluster hops in, it reaches the transition state (Fig. 2.8(c)), in which one bond is partially formed and simultaneously another is partially broken (dashed red). Such cooperative bond formation/breaking allows for a low activation barrier. Clusters without such a transition state are immobile on our time scale. Finally the cluster reaches the state "0" (Fig. 2.8(d)) with the total number of bonds unchanged compared to the initial state "1," although the free energy of the system will not be identical to state "1." Our time scale ranges from sub-milliseconds to hours thus we are only able to observe clusters with activation barrier of ~20–30 k_BT and $K_{eq} \sim 1$ as shown in Fig. 2.8(e), black curve. We cannot resolve the motions of clusters having higher barriers (blue curve) or with K_{eq} far from 1 (red curve).

A comprehensive thermodynamic model for motion of compact clusters has been proposed, and within this random first order transition (RFOT) model[19] specific predictions have been made for glassy surface dynamics, such as might apply to the amorphous HfB_2 surface. In the surface version of the fuzzy-sphere model,[23] the barrier is proportional to the surface area of a cluster in contact with the glassy matrix. That surface area is approximately halved at the glass surface, yielding a barrier approximately 15–18 k_BT_g for compact cluster relaxations (α-relaxations), while string-like or β-relaxations remain near 10 k_BT_g. Our experimental barrier $\Delta G^{\dagger}_{01} \sim 23.6\, k_BT$, determined from dwell time distributions (Fig. 2.5(h)) together with the temperature dependence of the kinetics, is much smaller. In units of the glass transition temperature, $k_BT/k_BT_g \approx (298\ \mathrm{K})/(0.6T_m) \approx 0.15$ and $\Delta G^{\dagger}_{01} \approx 3.5$–$4.5\ k_BT_g$ for the full time range of motions we observe. Thus our observed barriers are small compared to the most probable barriers in the RFOT surface model. Is it nonetheless possible that such fast processes involving compact clusters could be observed?

To answer this question, we computed the activation barrier distributions at T_g for the bulk and surface according to the model described in Refs. 14 and 15 and briefly in Sec. 2.3. In the model the activation barrier freezes in at T_K (the Kauzmann temperature where the extrapolated enthalpy of the supercooled liquid approaches the crystal in an "entropy catastrophe"[39]). The barrier changes only slightly between T_g and T_K, thus our computation of a barrier distribution at T_g is reasonable for comparison with our experiment, although our

experiment occurs at $T \approx 0.15T_g$. In addition, aging takes place on a substantially longer time scale, thus in our time regime of milliseconds to hours, the aging effect is expected to be small. We modified the RFOT model to account for the smaller surface activation free energy as discussed in Ref. 23.

The bulk and surface results for a strong glass (fragility m = 30), typical of ceramics such as HfB_2, are shown in Fig. 2.9. Distributions for others fragilities are shown in Fig. 2.17 in the supplementary material for completeness.[30] Our observed barrier $\Delta G^{\dagger}_{01} \approx 3.5–4.5\ k_BT_g$ falls into the lower β-relaxation tail of the distribution, which is quantitatively in agreement with the small fraction of hopping clusters observed of ~0.2%.

RFOT theory predicts that in the bulk α-relaxation originates from compact clusters while β-relaxation originates from more string-like cooperative regions.[14,15] On the glass surface, we observe dynamics of α-relaxation-like compact clusters deep below T_g, but with an activation barrier that lies in the tail of the β-relaxation distribution. String-like collective relaxations attributed to collective β-relaxation have also have been seen in simulations, and kinetic facilitation models propose "collisions" of string-like relaxors to reduce strain and facilitate global motion. We do not observe events such as these at all in our experiments. We postulate that on the glass surface, string-like clusters have more freedom to reconstruct to more compact shapes, thereby minimizing surface tension while retaining high mobility (low friction with the matrix = low barriers). In our view, α-like shapes combined with β-like low barriers would be universal at the glass surface. If so, our past experiments sampling barriers in the higher free energy 10–15 k_BT_g range[6,24–26] were looking at the β/α cross-over region in Fig. 2.9. It will be interesting to see what detailed thermodynamic and kinetic models developed specifically for the glass surface will say. Experiments in turn can explore a wide range of barrier heights in units of k_BT_g by picking glass-formers with a wide range of glass transition temperatures.

2.6. Supplementary information

2.6.1. Surface characterization

X-ray photoelectron measurements were performed on Kratos Axis ULTRA with a monochromatic Al source after STM data collection. XPS spectra reflected the oxidized samples. Cross-section scanning electron microscopy was carried out on a Philips XL30 ESEM-FEG.

Samples were cleaved manually then transferred to the HV chamber (base pressure $<1.3 \times 10^{-3}$ Pa) for cross-section SEM measurements. Results are shown in Fig. 2.10.

Cluster size analysis was done following the procedure in Ref. 24. To reduce error, only clear clusters were analyzed. For hopping clusters, only clusters that hop at least twice were counted. We used a boron unit cell for HfB_2 crystal[27] which has two hexagonal boron bases and one Hf atom at the middle as the GFU. The GFU diameter is calculated as the average of three perpendicular dimensions to be ~ 0.34 nm.

2.6.2. Individual cluster time traces

To obtain z-displacements as a function of time for individual clusters, we used a modified scanning tunneling spectroscopy protocol. The voltage was ramped over a very small range from 2.0 V to 2.1 V for hafnium diboride and from -2.0 V to -2.1 V for hydrogen-passivated silicon (100)-2x1samples. 1000 steps at various time resolutions yielded the tunneling current from ms to tens of s. At each step, the current was measured a number of times and the average was taken. Thus time resolution is defined as a function of number of points averaged. It takes 16.5 μs to measure a current point thus time resolutions of 16.5 μs, 49.5 μs, 0.495 ms, 8.25 ms, and 33 ms correspond to 1, 3, 30, 500, and 2000 point averages, respectively. Registration with the cluster center was always maintained for at least 20 s, but above 20 s there was sufficient tip drift to lose the alignment with the center of the individual clusters. This effect is illustrated in Fig. 2.11(b), where the amplitude of the current 'telegraph' noise drops after 20 s.

Scanning tunneling spectroscopy (STS) were measured on two-state clusters in state "1" and "0" using variable spacing STS. The voltage was ramped from 2 V to -2 V in 2000 steps while the tunneling current is measured. Furthermore, the tip sample spacing was decreased linearly by 0.2 nm between the ± 2V and 0 V.

The z distance change-tunneling current calibration curve was measured using the spacing-tunneling current STS mode at constant voltage (2 V). The current was increased and the corresponding changes in the z distance were recorded. Data presented in Fig. 2.5(c) is the average of six measurements on six different positions on the surface. The same procedure was applied for the silicon surface except the voltage was -2 V. Calibration on the Si(100) step edge is shown in Fig. 2.16. The reported error ±0.001 nm is the precision of the measurements. The accuracy can be seen from the plot in Fig. 2.16.

2.6.3. Potential of mean force analysis

The separation and free energy differences between two states are calculated from the potential of mean force function $PMF(z) = -k_BT\ln(H(z))$ where $H(z)$ is the histogram of the z values converted from current traces using the calibration curve in Fig. 4b. The histogram bin size is ~ 2.5 times smaller than the RMSD of in-state hopping. We ignored middle-transition points resulting from averaging and limited time resolutions in histogram calculations. The resulting $PMF(z)$ function depicts the shape of the wells. The activation energy from state "0" to "1" is calculated as $\Delta G^{\dagger}_{01}=-k_BT\ln(k_{01}/\nu^{\dagger})$ where $k_{01}=1/\langle\tau_{01}\rangle$, $\langle\tau_{01}\rangle$ is the average dwell time staying in state "0", and the prefactor is $\nu^{\dagger}= 6\text{x}10^{10}$ s^{-1}. Here the faster rate is selected to calculate the $\Delta G^{\dagger}_{01}$ to avoid over-dominating of rate by fast hops. Due to the limit of bandwidth of current preamplifier (10 kHz), there are more "transition points" in the current traces measured at time resolutions < 100 μs. Only current traces with time resolution > 100 μs were used to analyze free energy landscapes.

2.7. Figures and tables

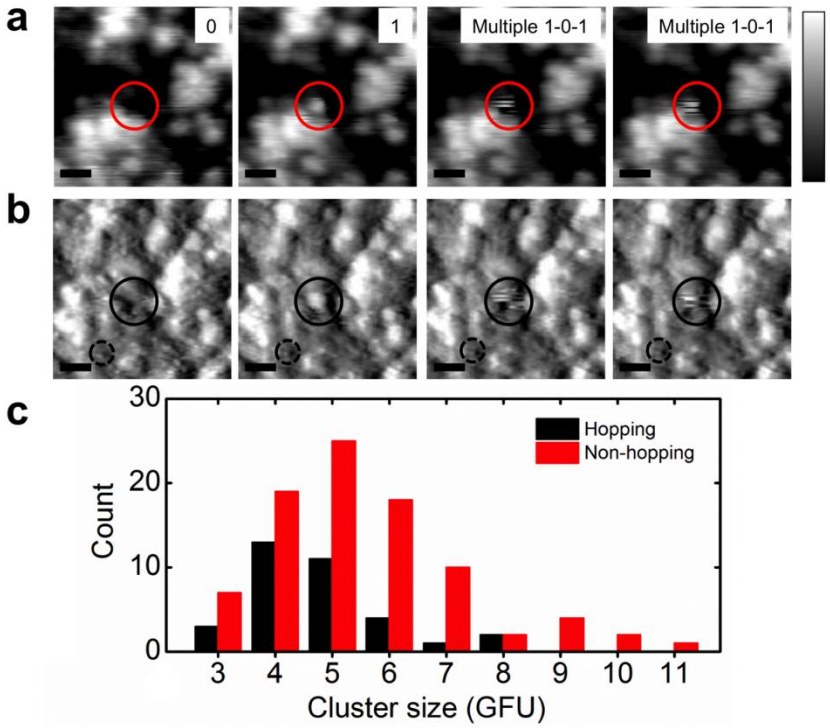

Figure 2.1: Topography, derivative, and cluster size as a multiple of the number of HfB_2 glass forming units (GFU). (a) STM topographic images showing a compact cluster (circled) that is initially slow hopping between complete frames then becomes fast hopping in and out several times in one frame. The full height range is 0–1.0 nm but is narrowed down to highlight the hopping cluster (gray scale bar: 0.4–0.9 nm). (b) The corresponding STM derivative images for frames in (a). The smallest features are comparable to the size of a glass forming unit (dashed circled). Clusters can be resolved in topography mode but are best visualized in derivative mode. See Movies 1(a) and 1(b) for full movies of panels (a) and (b). Scanning conditions: 1 V, 100 pA. Scale bars: 3 nm. (c) Cluster size distributions for hopping and non-hopping clusters. For hopping clusters, only ones that hop at least twice are counted. The average diameters for hopping and non-hopping clusters are 4.8 ± 1.2 and 5.3 ± 1.8 glass forming units, respectively. The hopping clusters are slightly smaller than non-hopping clusters, in good agreement with RFOT theory.[19]

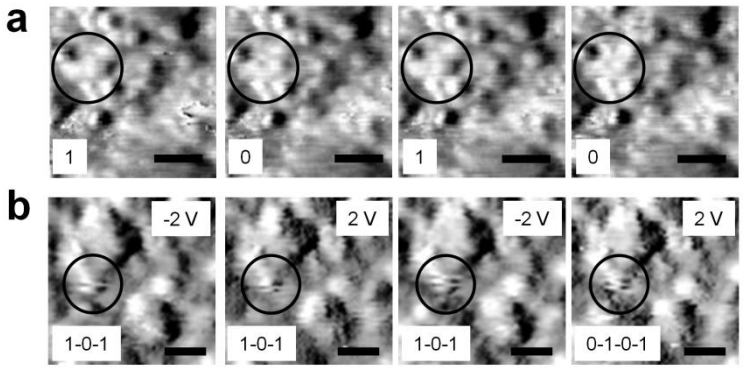

Figure 2.2: Cluster structure (derivative images). (a) Sub-cluster resolution of a cooperatively rearranging region (circled) indicating the cooperative nature of surface glass dynamics. The shape, position, and orientation of the cluster are unchanged during hopping, excluding the possibility that the dynamics is diffusion. Scanning conditions: 2 V, 100 pA. (b) Bias reversal movie scanned at 10 pA tunneling current showing a fast cluster (circled). The tunneling current is 10 times smaller than in (a) but the hopping rate is substantially faster. Movies in (a) and (b) show that hopping rate is independent of bias voltage and tunneling current, thus excluding charging effects observed on semiconducting surfaces. Scale bars: 2 nm.

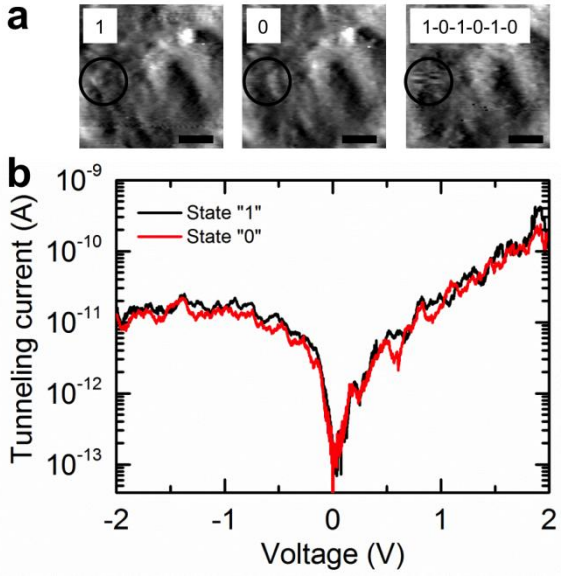

Figure 2.3: Scanning tunneling spectroscopy. (a) Three frames from a two-state cluster STM movie (derivative mode). This cluster either moves laterally or anticorrelated motion of two adjacent clusters takes place. Scanning conditions: 2 V, 100 pA. Scale bars: 3 nm. (b) STS measured on the cluster circled in (a) in state "1" and state "0." Both STS show metallic behavior indicating no significant change in electronic structure. This observation rules out diffusing adsorbates and enables quantitative current-height calibration.

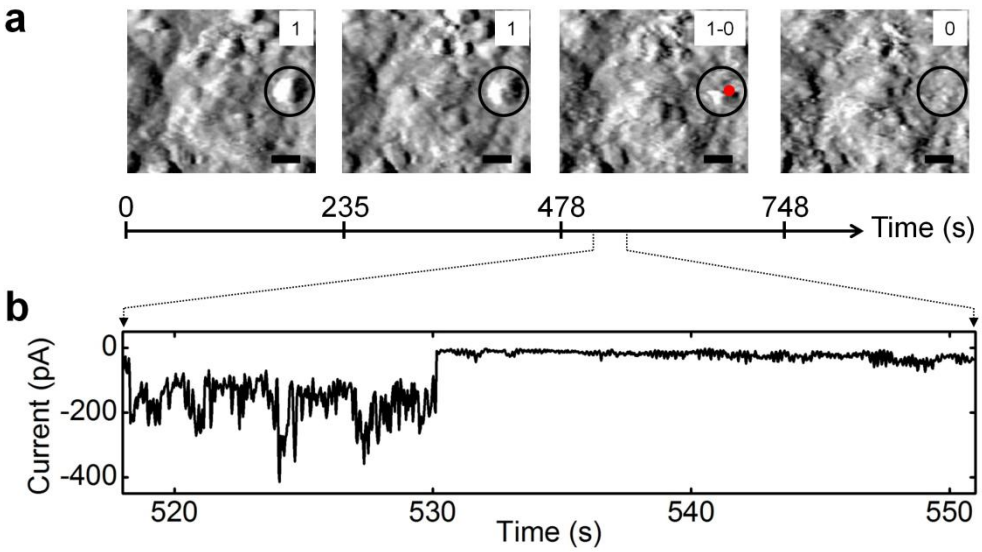

Figure 2.4: Fast cluster dynamics detection methodology. (a) A fast cluster is identified by scanning an area for several frames (circled, derivative mode). Once the fast cluster is selected, the same area is scanned until the tip reaches a predefined point on the top of that cluster (red dot), then the feedback is turned off and the tunneling current is measured. After measuring tunneling current, the tip continues scanning the rest of the image. The scanning direction is from left to right, bottom to top. (b) The tunneling current-time trace of the cluster in (a). During measurement, the cluster hopped in corresponding to a drop in tunneling current at ~530 s in the time trace. Scanning conditions: 2 V, 100 pA. All scale bars: 3 nm. Time resolution: 33 ms/point.

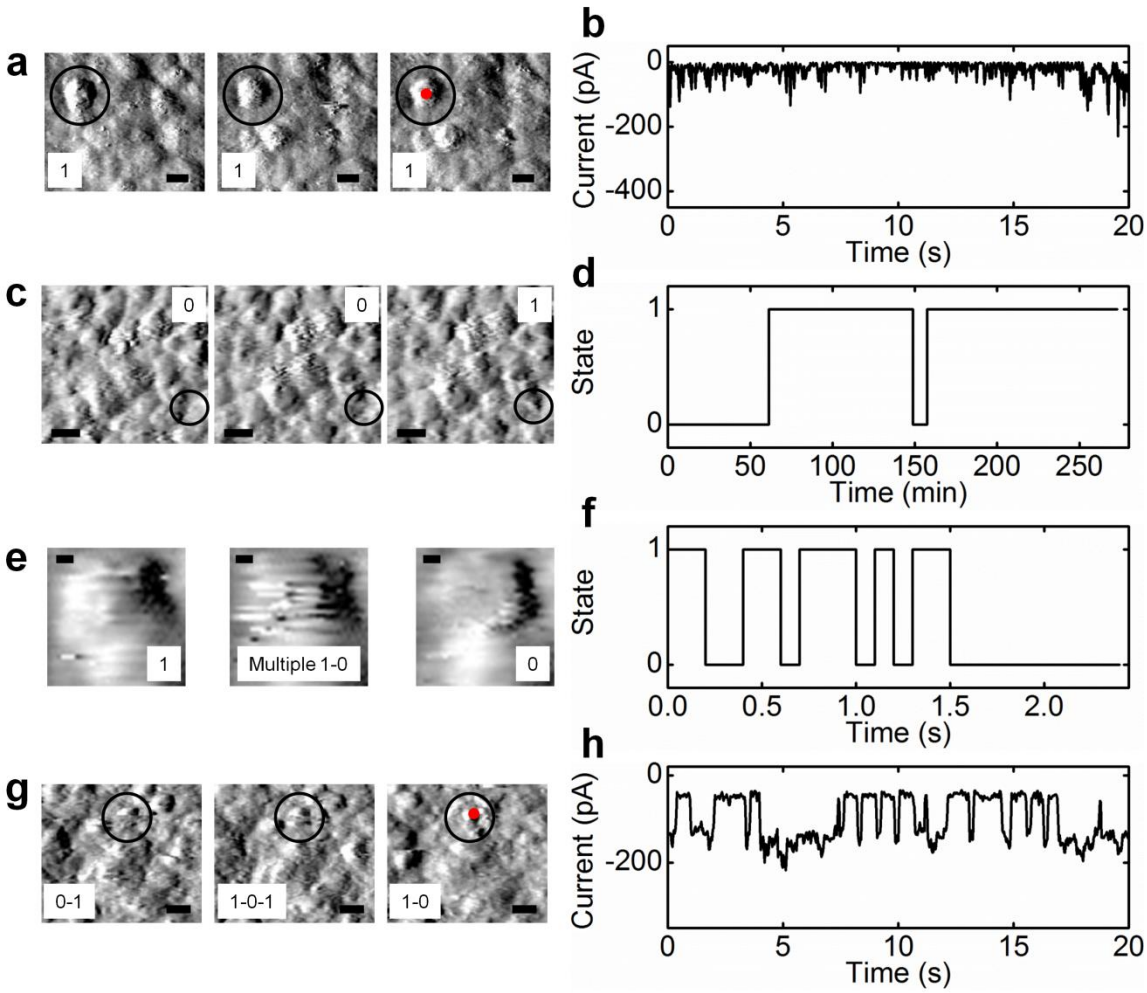

Figure 2.5: Wide range of dynamics on a-HfB_2 surface (derivative images). (a) A slow cluster (circled) that never hops. Scanning conditions: 2 V, 100 pA. Scale bars: 3 nm. (b) The tunneling current measured at a single point on the cluster (red dot) in (a) showing no hopping activity but fluctuation around its local minimum. Time resolution: 33 ms/point. (c) A slow cluster (circled) hopping in and out in complete scans. Scanning conditions: 2 V, 100 pA. Scale bars: 3 nm. Time resolution: 105 s/frame. (d) Two state trace reconstructed for the cluster in (c). (e) A fast cluster resolved by fast scans. Scanning conditions: 2 V, 10 pA. Scale bars: 0.4 nm. Time resolution: 100 ms/line. (f) Two state trace reconstructed for cluster in (e). (g) A fast cluster (circled) showing multiple hops in one frame. Scanning conditions: 2 V, 100 pA. Scale bars: 3 nm. (h) The tunneling current measured on the top of the cluster (red dot) in (g) indicating two-state behavior. Time resolution: 33 ms/point.

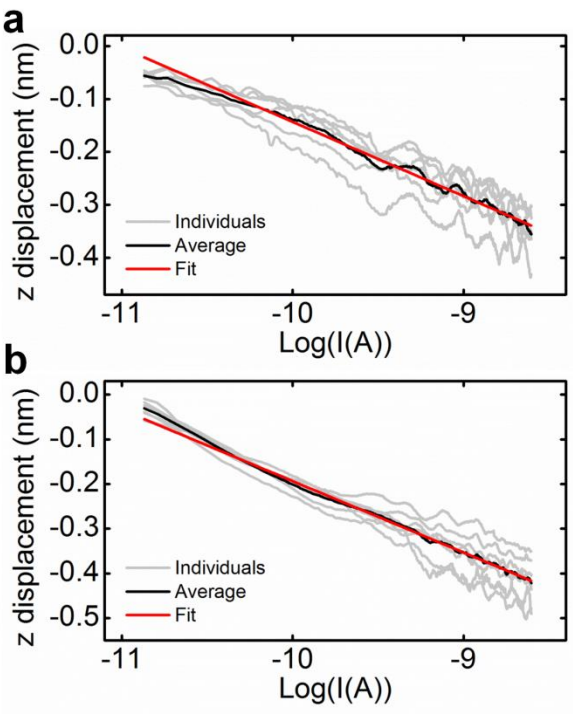

Figure 2.6: Height calibration. (a) Distance as a function of tunneling current for a-HfB_2 and (b) hydrogen passivated Si (100)-2×1 surfaces. Despite the non-uniform nature of the amorphous surface, current fluctuations between measurements are similar to crystalline Si, validating the use of an average calibration curve.

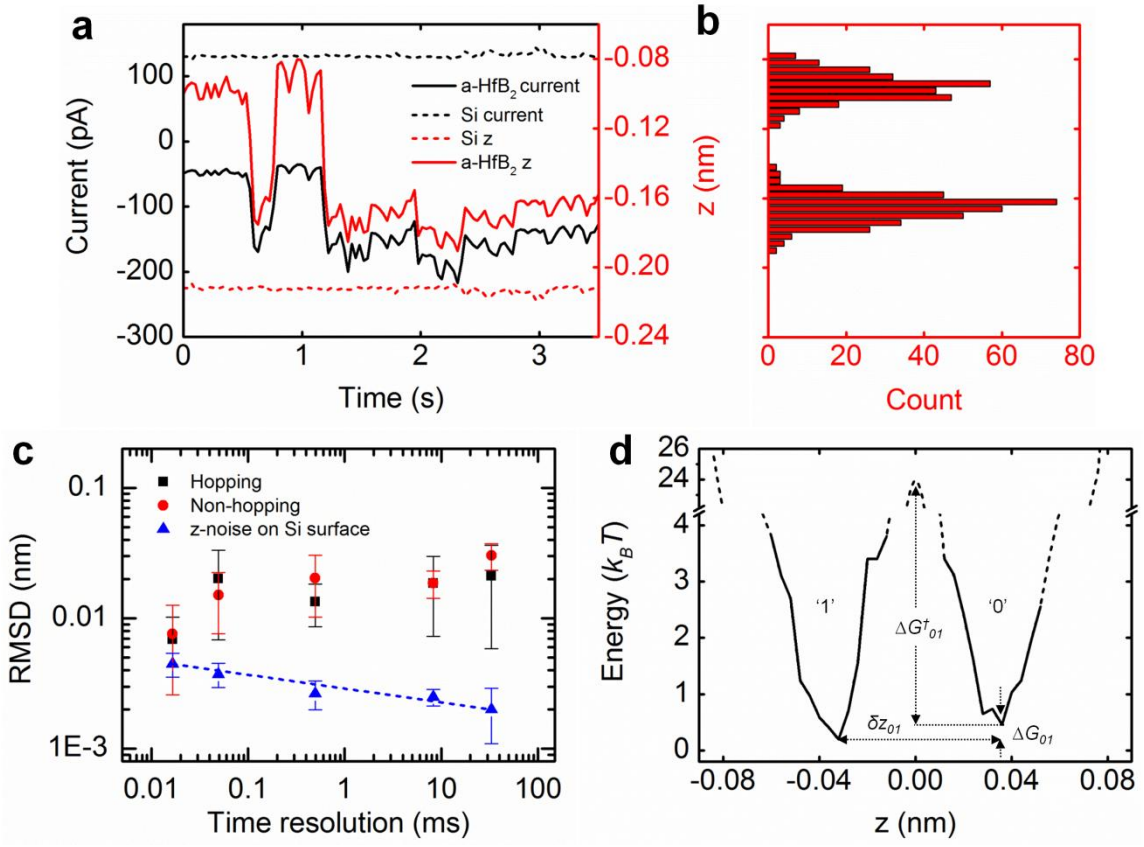

Figure 2.7: Single cluster energy landscape. (a) Tunneling current as a function of time for hydrogen passivated Si (100)-2 × 1 (dashed black) and a-HfB_2 (black, part of the current trace in Figure5(h)). Dashed red and red curves are the converted z distance traces for silicon and a-HfB_2, respectively. Fluctuation in tunneling current and thus on z distance on a-HfB_2 surface is ≈10 times larger than on Si surface. (b) Histogram of the complete z trace corresponding to the current trace in Figure 5(h). (c) RMSD as a function of time resolution. The constant, larger value, and opposite trend of the RMSD from the expected noise indicate the existence of real in-state glassy dynamics. The non-hopping and hopping clusters have similar RMSD values. (d) Two-state free energy landscape in k_BT unit for the cluster in Figure 5(g). Solid line is the potential of mean force calculated from experimental data showing the shape of the wells. Dashed line is the extrapolation assuming a smooth transition between two states. $\delta z_{01} \approx 0.07$ nm, $\Delta G_{01} \approx 0.26\ k_BT$, and $G^{\dagger}_{01} \approx 23.55\ k_BT$.

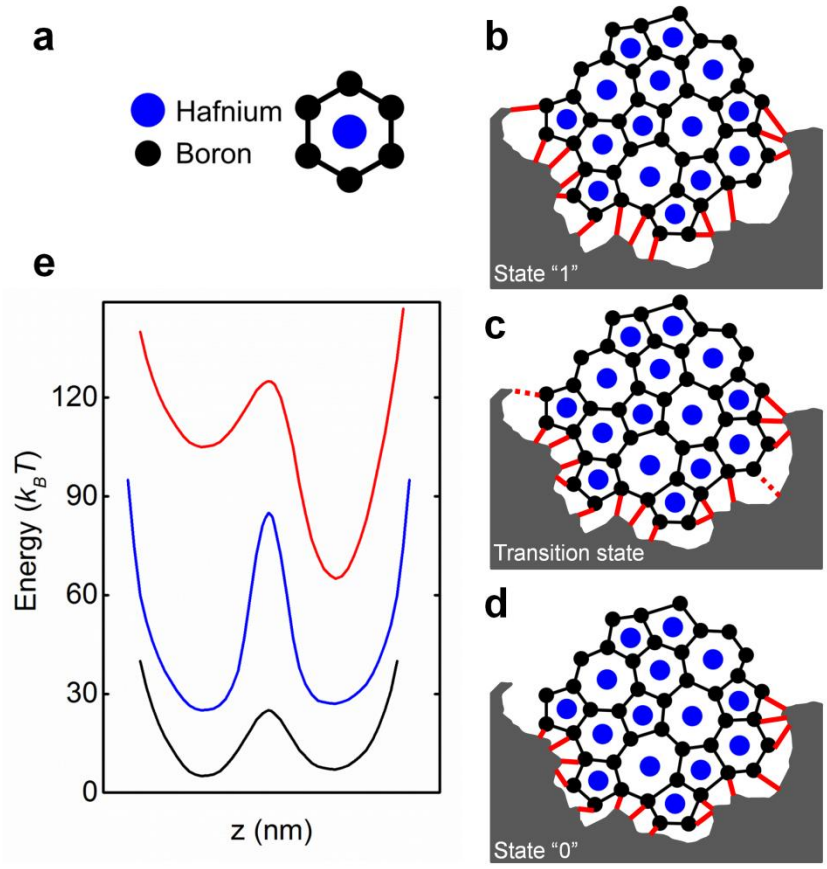

Figure 2.8: Schematic diagram for two-state dynamics on a-HfB_2 surface. (a) Top view of the unit cell of crystalline HfB_2. We take the size of this unit cell as the size of a GFU. (b) A typical CRR of ~5 GFU in diameter embedded in the glass matrix (uniform grey color, but the structure is similar to the CRR), initially at the state "1" when the cluster is "out." (c) The transition state in which most of the bonds (solid red) are remained the same while several bonds (dashed red) are breaking and forming. (d) The final state "0" with the total number of bonds unchanged. (e) In our time scale ranging from sub-milliseconds to hours, we are only able to observe clusters with activation barriers of ~20–30 k_BT and $K_{eq} \sim 1$ (black curve). Observations are unfeasible for clusters with higher activation barrier (blue) or $K_{eq} \gg 1$ (red).

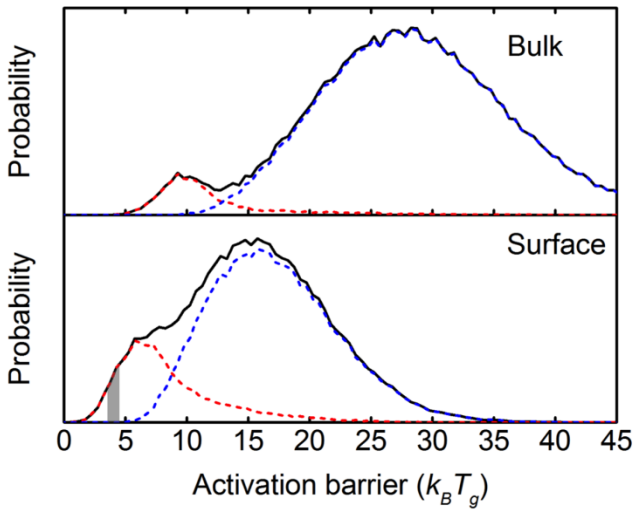

Figure 2.9: Activation barrier distributions at T_g for bulk (top) and surface (bottom) of glasses. The contributions of α- (dashed blue) and β- (dashed red) relaxations to the total distribution (solid black) are shown. The gray region highlights our accessible range of barriers for HfB_2, which has a very high putative glass transition temperature.

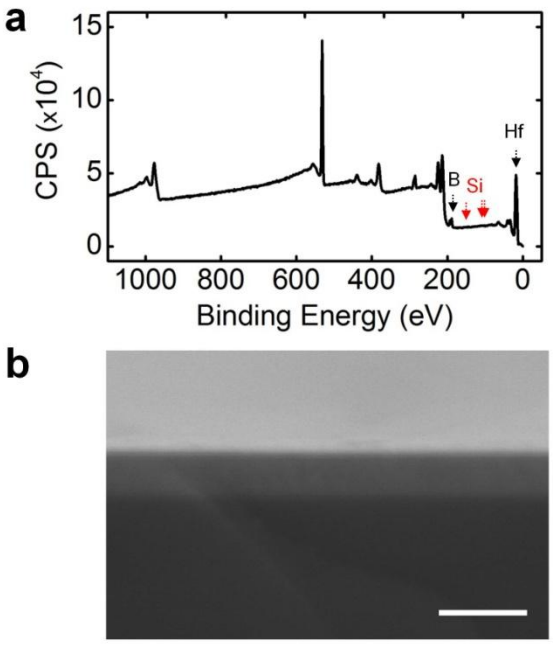

Figure 2.10: Sample characterization. (a) A typical XPS measurement of oxidized sputtered samples showing hafnium peaks at ~15 eV (right black arrow), boron peaks at~189 eV (left black arrow) and no silicon peaks at 99 eV, 103 eV (Si in SiO2) and 151 eV (red arrows) confirming the hafnium diboride nature of the samples. The average Hf:B ratio is 1:1.55 (b) Cross-section SEM image of a ~101 nm (~288 layers of hafnium) hafnium diboride amorphous thin film sample. The thickness ranges from 46 nm – 101 nm. Scale bar: 200 nm200 nm.

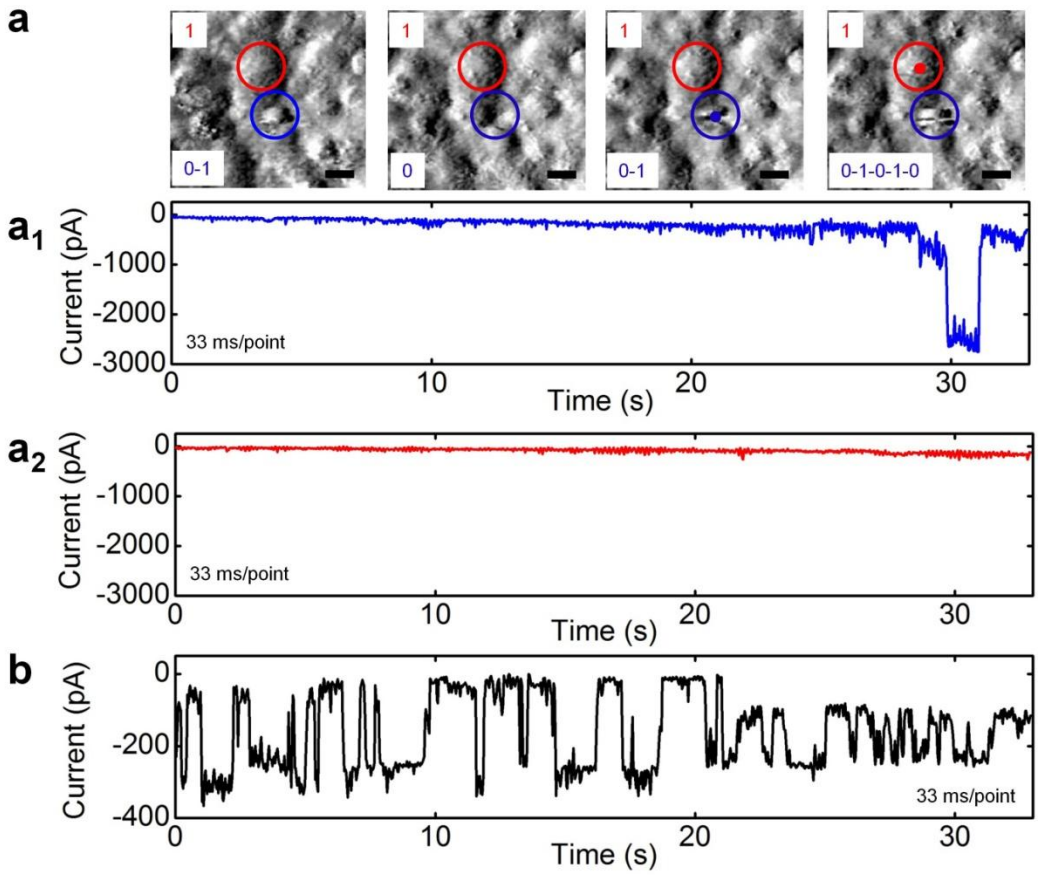

Figure 2.11: Fast cluster and stable cluster in the same area. (a) A stable cluster (red circle) and a fast cluster (blue circle) are indentified in the same area. Scanning conditions: 2V, 50 pA. (a_1), (a_2) The tunneling current collected on the top of the fast cluster (blue dot) shows a two-state behavior while the tunneling current collected on the stable cluster (red dot) is essentially constant. (b) Another example of fast cluster showing multiple hopping. After ~20 seconds, the tip drifted to another part on the cluster but the two-state hopping is maintained. Scale bar: 3 nm.

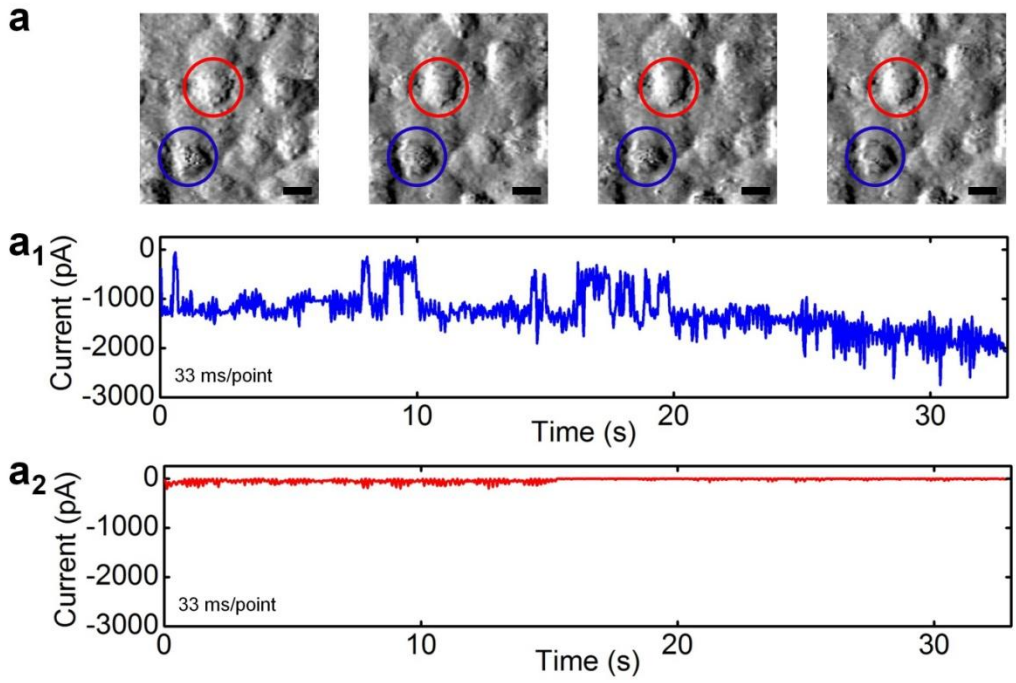

Figure 2.12: Two-state dynamics on noisy cluster. (a) A noisy cluster (blue circle) with noise on the top in many frames and a stable cluster (red circle). (a_1) The tunneling current measured on the top of the noisy cluster shows two-state dynamics behavior. The fast back and forth hopping during scanning causes the noise in the STM images. (a_2) The tunneling current on the stable cluster is constant. Scanning conditions: 2 V, 100 pA. Scale bar: 3 nm.

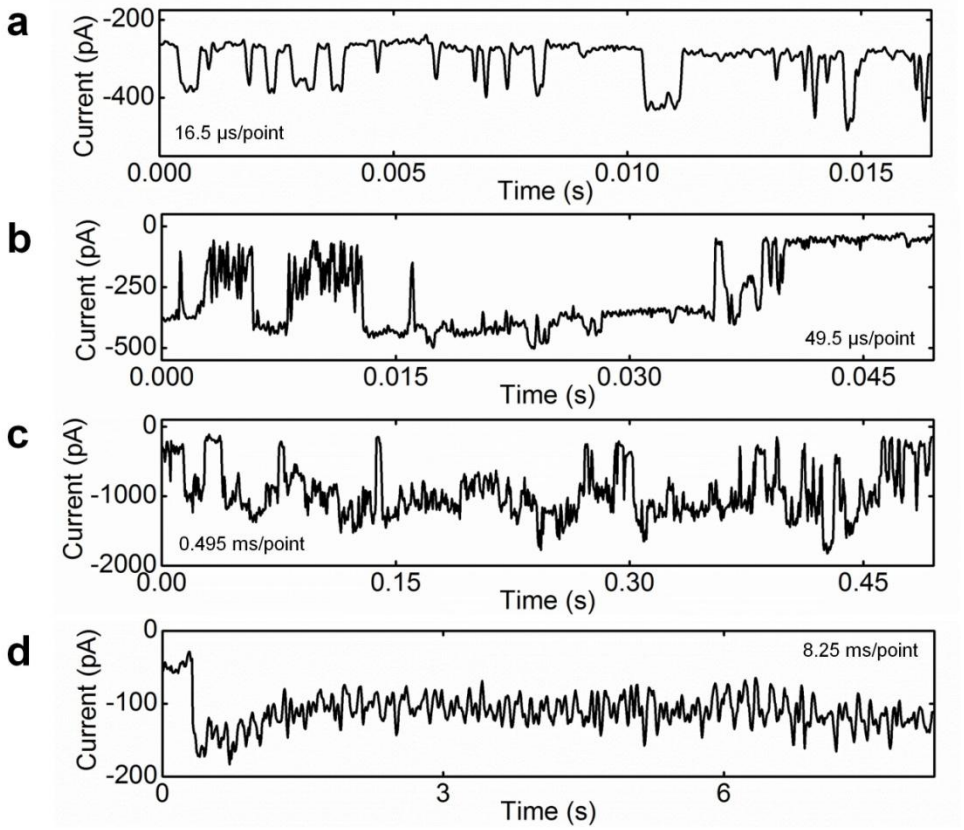

Figure 2.13: Two-state dynamics at different time resolutions (number of point average). (a) 16.5 µs (1 point average), (b) 49.5 µs (3 point average), (c) 0.495 ms (30 point average) and (d) 8.25 ms (500 point average). All scanning conditions: 2 V, 100 pA.

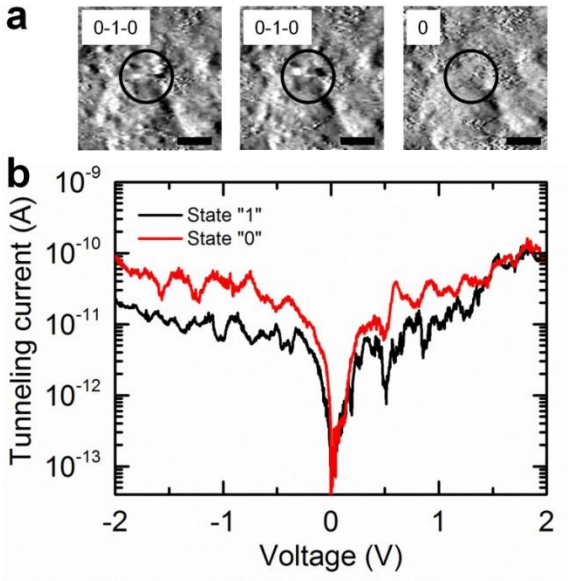

Figure 2.14: Another example of cluster electronic structure. (a) A two-state cluster (circled). Scanning conditions: 2 V, 100 pA. Scale bars: 3 nm. (b) STS measured on state "1" and state "0", both show metallic behavior.

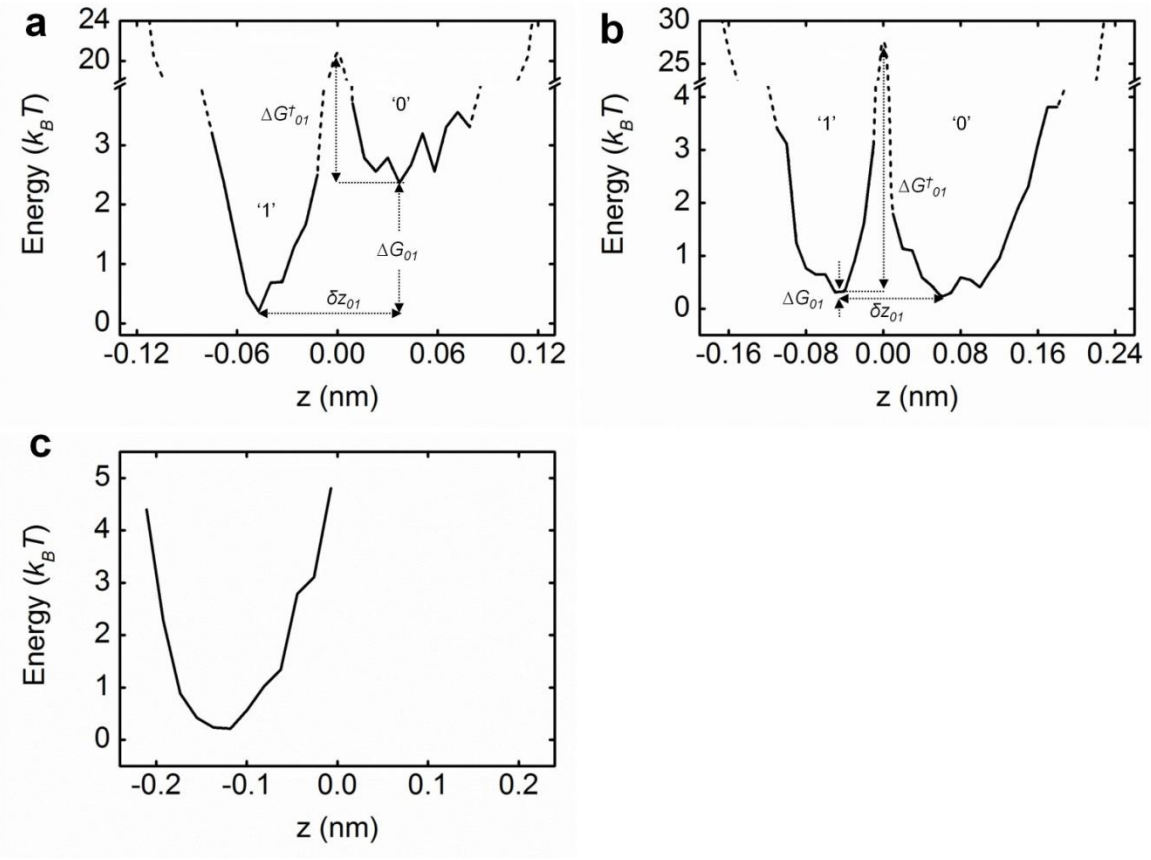

Figure 2.15: More examples of experimentally determined single-cluster energy landscapes. (a) The energy landscape for the cluster in Figure 2.13(c). $\delta z_{01} \approx 0.08$ nm, $\Delta G_{01} \approx 2.17\ k_BT$ and $\Delta G^{\dagger}_{01} \approx 18.46\ k_BT$. (b) The energy landscape for the cluster in Figure 2.4. $\delta z_{01} \approx 0.11$ nm, $\Delta G_{01} \approx 0.09\ k_BT$ and $\Delta G^{\dagger}_{01} \approx 27.29\ k_BT$. (c) The energy landscape for the non-hopping cluster in Figure 2.11(a2).

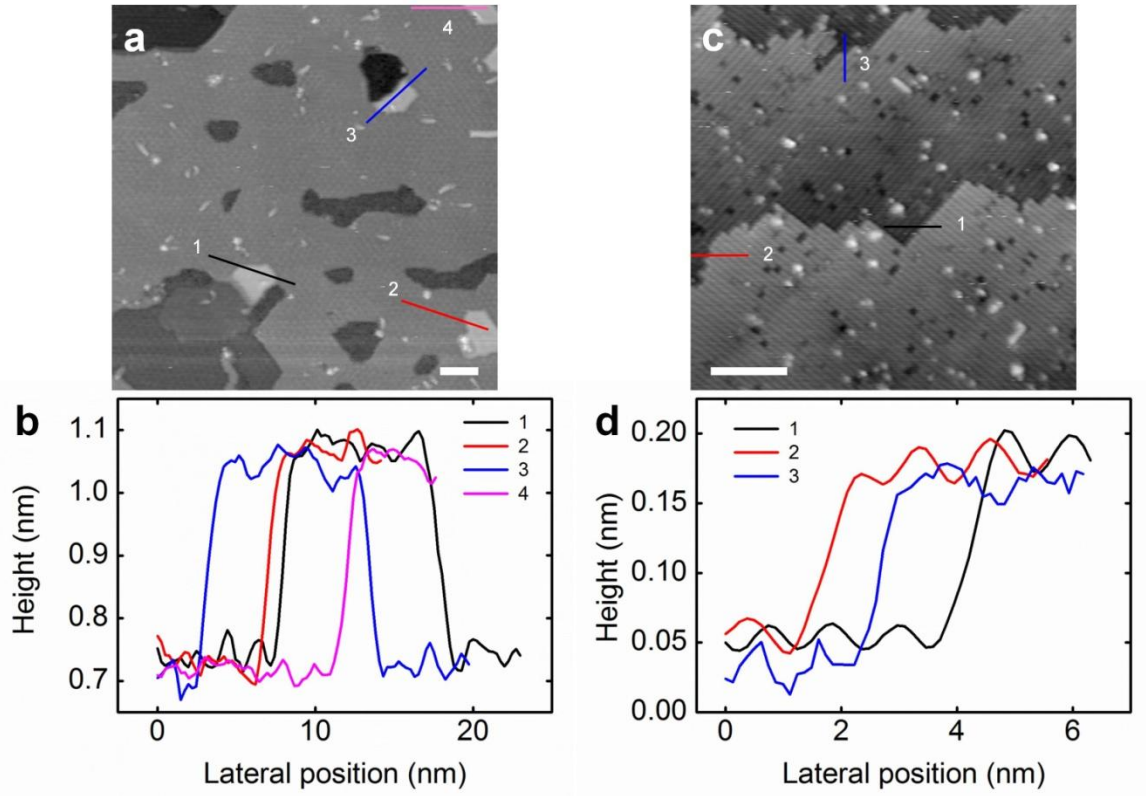

Figure 2.16: STM piezo calibrations. (a) Topographic STM image of graphene on 4H-SiC(0001). Scanning conditions: 2 V, 100 pA. (b) Height profiles of graphene steps spotted in (a). The average measured graphene step height is 0.331 nm ± 0.005 nm. The layer spacing in graphite is 0.335 nm. (c) Topographic STM image of hydrogen passivated Si(100)-2x1. Scanning conditions: -2 V, 50 pA. (d) Height profiles of the steps in (c). The measured height is 0.134 nm ± 0.001 nm (precision) while the step height for Si(100) is 0.136 nm. All scale bars: 10 nm.

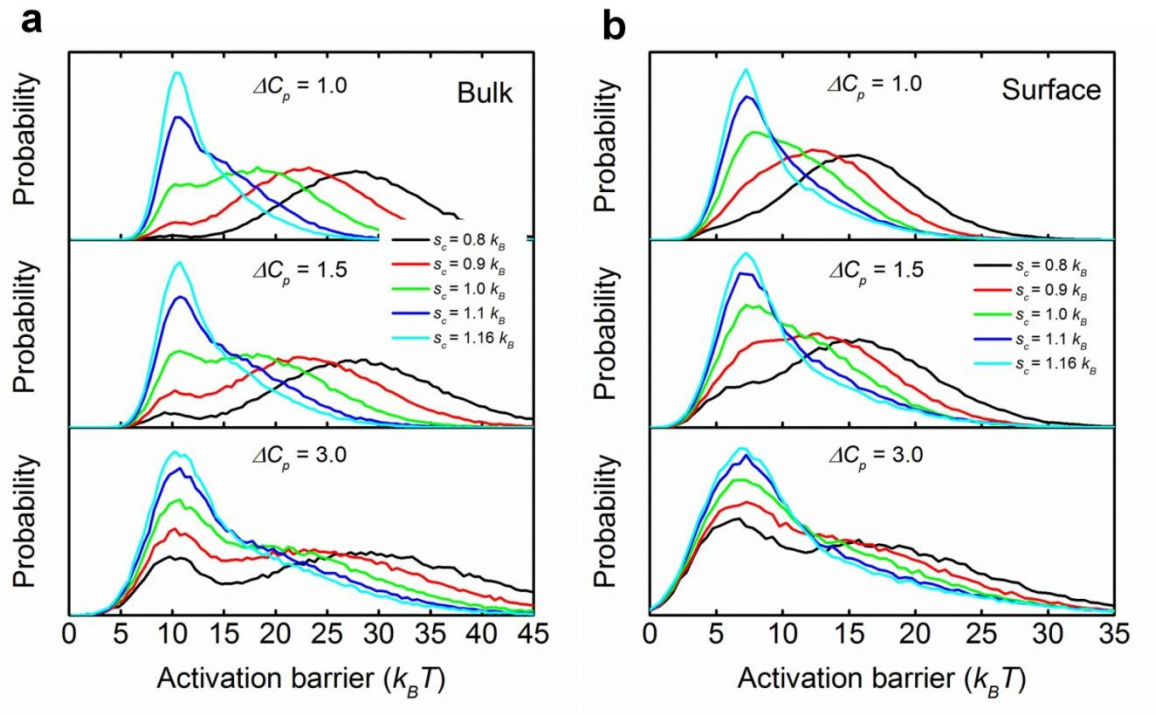

Figure 2.17: Activation barrier distributions for (a) bulk and (b) surface with different fragility and temperature. s_c = 0.8 k_B at T_g and s_c = 1.16 k_B close to crossover T. Fragility m was determined through the correlation $m = 20.7\ \Delta C_p$. The top and bottom of (a) are the same as Fig. 2 in Ref. 15. On the surface, the peak for β-relaxation is stronger relative to the α–relaxation peak.

2.8. Movies

Movie 2.1a: Topographic movie for the cluster in Fig. 2.1a. Scale bar: 3 nm. Time resolution: 106 s/frame.

Movie 2.1b: Derivative movie for the cluster in Fig. 2.1b. Scale bar: 3 nm. Time resolution: 106 s/frame.

2.9. References

1. Y. Cohen, S. Karmakar, I. Procaccia, and K. Samwer, Europhys. Lett. 100, 36003 (2012).
2. J. Horbach, W. Kob, K. Binder, and C. A. Angell, Phys. Rev. E 54, R5897 (1996).
3. E. R. Weeks, J. C. Crocker, A. C. Levitt, A. Schofield, and D. A. Weitz, Science 287, 627 (2000).
4. P. Schall, D. A. Weitz, and F. Spaepen, Science 318, 1895 (2007).
5. Z. Fakhraai and J. A. Forrest, Science 319, 600 (2008).

6. S. Ashtekar, G. Scott, J. Lyding, and M. Gruebele, Phys. Rev. Lett. 106, 235501 (2011).
7. L. M. Leone and L. J. Kaufman, J. Chem. Phys. 138, 12A524 (2013).
8. T. R. Kirkpatrick, Phys. Rev. A 31, 939 (1985).
9. S. P. Das, Rev. Mod. Phys. 76, 785 (2004).
10. F. H. Stillinger, Science 267, 1935 (1995).
11. R. Richert and K. Samwer, New J. Phys. 9, 36 (2007).
12. L. Berthier, G. Biroli, J. P. Bouchaud, L. Cipelletti, D. ElMasri, D. L'Hote, F. Ladieu, and M. Pierno, Science 310, 1797 (2005).
13. E. V. Russell and N. E. Israeloff, Nature (London) 408, 695 (2000).
14. J. D. Stevenson, J. Schmalian, and P. G.Wolynes, Nat. Phys. 2, 268 (2006).
15. J. D. Stevenson and P. G. Wolynes, Nat. Phys. 6, 62 (2010).
16. H.-B. Yu, W.-H. Wang, and K. Samwer, Mater. Today 16, 183 (2013).
17. J. Hachenberg, D. Bedorf, K. Samwer, R. Richert, A. Kahl, M. D. Demetriou, and W. L. Johnson, Appl. Phys. Lett. 92, 131911 (2008).
18. K. Lindorff-Larsen, S. Piana, R. O. Dror, and D. E. Shaw, Science 334, 517 (2011).
19. V. Lubchenko and P. G. Wolynes, Ann. Rev. Phys. Chem. 58, 235 (2007).
20. C. A. Angell, Science 267, 1924 (1995).
21. F. Ritort and P. Sollich, Adv. Phys. 52, 219 (2003).
22. T. Speck and D. Chandler, J. Chem. Phys. 136, 184509 (2012).
23. J. D. Stevenson and P. G. Wolynes, J. Chem. Phys. 129, 234514 (2008).
24. S. Ashtekar, G. Scott, J. Lyding, and M. Gruebele, J. Phys. Chem. Lett. 1, 1941 (2010).
25. S. Ashtekar, D. Nguyen, K. Zhao, J. Lyding,W. H.Wang, andM. Gruebele, J. Chem. Phys. 137, 141102 (2012).
26. S. Ashtekar, J. Lyding, and M. Gruebele, Phys. Rev. Lett. 109, 166103 (2012).
27. W. G. Fahrenholtz, G. E. Hilmas, I. G. Talmy, and J. A. Zaykoski, J. Am. Ceram. Soc. 90, 1347 (2007).
28. S. Sakka and J. D. Mackenzie, J. Non-Cryst. Solids 6, 145 (1971).
29. S. Jayaraman, Y. Yang, D. Y. Kim, G. S. Girolami, and J. R. Abelson, J. Vac. Sci. Technol., A 23, 1619 (2005).
30. See supplementary material at http://dx.doi.org/10.1063/1.4901132 for a description of the simulation program.

31. J. W. Lyding, S. Skala, J. S. Hubacek, R. Brockenbrough, and G. Gammie, Rev. Sci. Instrum. 59, 1897 (1988).
32. L.-M. Wang, C. A. Angell, and R. Richert, J. Chem. Phys. 125, 074505 (2006).
33. K. Hata, Y. Sainoo, and H. Shigekawa, Phys. Rev. Lett. 86, 3084 (2001).
34. H.B.Yu,K.Samwer,Y.Wu,andW.H.Wang, Phys. Rev. Lett. 109, 095508 (2012).
35. G. W. Brown, H. Grube, M. E. Hawley, S. R. Schofield, N. J. Curson, M. Y. Simmons, and R. G. Clark, J. Appl. Phys. 92, 820 (2002).
36. M. D. Ediger and J. A. Forrest, Macromolecules 47, 471 (2014).
37. S. F. Swallen, K. L. Kearns, M. K. Mapes, Y. S. Kim, R. J. McMahon, M. D. Ediger, T. Wu, L. Yu, and S. Satija, Science 315, 353 (2007).
38. X. Liu, B. E. White, R. O. Pohl, E. Iwanizcko, K. M. Jones, A. H. Mahan, B. N. Nelson, R. S. Crandall, and S. Veprek, Phys. Rev. Lett. 78, 4418 (1997).
39. V. Lubchenko and P. G. Wolynes, J. Chem. Phys. 121, 2852 (2004).

3. Composition-dependent metallic glass alloys correlate atomic mobility with collective glass surface dynamics

This chapter is reproduced from D. Nguyen, Z. G. Zhu, B. Pringle, J. Lyding, W. H. Wang and M. Gruebele, Composition-dependent metallic glass alloys correlate atomic mobility with collective glass surface dynamics, *Phys. Chem. Chem. Phys.*, in press, 2016, with permission from the Royal Society of Chemistry.

3.1. Abstract

Glassy metallic alloys are richly tunable model systems for surface glassy dynamics. Here we study the correlation between atomic mobility, and the hopping rate of surface regions (clusters) that rearrange collectively on a minute to hour time scale. Increasing the proportion of low-mobility copper atoms in La-Ni-Al-Cu alloys reduces the cluster hopping rate, thus establishing a microscopic connection between atomic mobility and dynamics of collective rearrangements at a glass surface made from freshly exposed bulk glass. One composition, $La_{60}Ni_{15}Al_{15}Cu_{10}$, has a surface resistant to re-crystallization after three heating cycles. When thermally cycled, surface clusters grow in size from about 5 glass-forming units to about 8 glass-forming units, evidence of surface aging without crystal formation, although its bulk clearly forms larger crystalline domains. Such kinetically stable glass surfaces may be of use in applications where glassy coatings stable against heating are needed.

3.2. Introduction

Glass forms when a liquid is cooled fast enough to avoid crystallization.[1] Viscosity and relaxation timescales increase ~10 orders of magnitude in a narrow temperature window as the glass transition is approached, yet without substantial change in structure.[2] Two main modes of relaxation are often used to classify the dynamics of supercooled liquids and glasses. Slower α-relaxation is frozen as the glass transition temperature (T_g) is approached. Faster β-relaxation, which is thought to be a more localized precursor of the α-relaxation, progresses into the glassy regime and is the main relaxation mode below T_g.[2] β-relaxation manifests itself as a pronounced peak or shoulder at the higher frequency or lower temperature side of the α-relaxation peak in dielectric[3] or mechanical measurements.[4]

The free energy barriers of bulk β-relaxation are generally pegged around 10 $k_B T_g$, while bulk α barriers are closer to 35 $k_B T_g$.[2,5] Relaxation in the bulk of glasses below T_g is therefore extremely slow. On the surface of glasses, relaxation is enhanced due to reduced constraints at the free surface. Enhanced surface mobility enables observations deep below T_g,[6-11] a temperature range inaccessible for bulk measurements. Thermodynamic models of the glass transition predict that the activation barrier for surface relaxation is roughly half of the bulk value.[12] Experiments on polymer glass surfaces have shown that surface mobility is orders of magnitude higher than in the bulk.[13,14] The distinction between α- and β-relaxations does not seem to be as clear on atomic glass surfaces[10] as in the bulk: we observed cooperative rearrangement of round regions (α-like shape), but at a high rate (β-like speed). We attribute this to reduced constraints at the surface favoring more compact shapes of lower free energy, and allowing faster dynamics of those shapes.

Metallic glass (MG) is a prototype atomic glass, ideal for investigating glass dynamics both theoretically and experimentally[15] due to its simple structure. Despite a simple atomic structure, MGs can exhibit more than one mode of bulk β-relaxation,[16] attributed to different mobility of different atom pairs. La-Ni-Al MG alloy in particular has a similar large negative values of mixing enthalpy for all the atomic pairs, and shows a pronounced β-relaxation peak well separated from α-relaxation.[17] Zhu et al.[4] showed that the high mobility of La and Ni atoms drastically lowers the peak β-relaxation temperature. Adding atoms with lower mobility (e.g. Cu) either increases the peak β-relaxation temperature or decreases the peak α-relaxation temperature, making the β-peak a shoulder in thermo-mechanical experiments (Fig. 3.1). The connection of this behavior with nano-scale glass dynamics has not yet been established, so La-Ni-Al-Cu MGs of varying composition are an ideal model system for such studies.

In this paper, we investigate surface dynamics of four La-based MGs well below T_g by systematically varying composition (and β-relaxation behavior). We freshly expose bulk glass at the surface, to study the resulting surface dynamics and aging. We use scanning tunneling microscopy (STM) movies to reveal the nanoscale dynamics of metallic clusters (cooperatively rearranging regions) hopping on the glass surface on a minute to hour time scale. We show that a composition with pronounced β-relaxation peak exhibits substantially faster surface cluster hopping. The hopping slows down when highly mobile atomic species (La, Ni) are replaced by slower ones (Cu), highlighting the correlation across size scales from atomic mobility, to

nanoscale hopping dynamics, and to shifts in β-relaxation peak temperature of bulk dynamical mechanical analysis (DMA) experiments. Adding more elements makes the amorphous surface more stable. One composition was even more stable kinetically than the bulk against crystallization after repeated heating cycles. The freshly exposed bulk surface does appear to age: upon repeated annealing, the hopping rate reduces and the clusters become larger, with a size distribution of clusters extending up to 8 average atomic diameters compared to 5 average atomic diameters for the original surface.

3.3. Experimental methods

3.3.1. Sample preparation and structural characterization

Four La-based MGs were used in this study. The ingots of the alloys were prepared by arc melting the constituent elements in a Ti-gettered argon atmosphere. Each ingot was re-melted at least five times to ensure chemical homogeneity and finally plated with dimension of 1 mm × 15 mm × 60 mm by copper mold suction casting. The amorphous nature of the as-cast alloys was verified by a Bruker D8 Advance X-ray diffraction (XRD) instrument using Cu-K_α diffraction. The thermal behavior of the as-cast alloys was analyzed on a Perkin Elmer differential scanning calorimeter (DSC) 8000 with a heating rate of 20 K/min. After STM characterizations, the crystallinity of the re-melted samples was checked by XRD (Philips X'pert MRD, Cu-Kα) and DSC (TA Instrument Q20, 20 K/min).

3.3.2. Scanning tunneling microscopy characterization

Topographic movies of the surfaces of the as-cast and re-melted La-based MGs were collected using a home-built STM[18] with base pressure $\leq 7 \times 10^{-9}$ Pa. Prior to STM imaging, as-cast glass samples were outgassed at room temperature for two days until the pressure was $\leq 7 \times 10^{-8}$ Pa. Previously it has been shown that sputtering and scraping to expose fresh bulk glass to the surface yields similar glassy dynamics.[8] We scraped the surfaces under UHV to remove oxides and expose fresh bulk glass using an in-situ degassed stainless steel blade. The freshly exposed glass can be tested for thermally-assisted aging. As-cast scraped samples were re-melted near the melting temperature T_m by resistively heating under UHV for cycles of 20 seconds. The current was directly flowed through the samples. The sample temperature was determined to be near the melting temperature T_m when flow (sagging) was observed, at which point the heating

was turned off after 20 seconds. Rapid heating avoided oxidation by keeping the base pressure below $6.7x10^{-6}$ Pa. The same protocol was followed for all alloys to enable direct comparison of surface changes.

3.4. Results

We investigated four systematically varied compositions of La-based metallic glasses (Table 3.1): $La_{60}Ni_{15}Al_{25}$, $La_{50}Ni_{15}Al_{25}Cu_{10}$, $La_{60}Ni_{10}Al_{25}Cu_5$ and $La_{60}Ni_{15}Al_{15}Cu_{10}$ previously have been shown to have different bulk β-relaxation characteristics. For completeness, Figure 3.1 shows the results from ref. 4 of isochronal DMA. In this analysis, a sinusoidal stress at a frequency of 1 Hz was applied to the glass sample at a constant temperature scan rate from below 300 K to above 500 K. The in-phase (G') and 90° out of phase (G") shear modulus were measured. The loss modulus G" of a bulk glass generally peaks near the glass transition temperature T_g. Two broad peaks or shoulders corresponding to β-relaxation (lower temperature) or α-relaxation (higher temperature) were observed (Figure 3.1). Table 3.1 summarizes Kohlrausch–Williams–Watts fits of the approximate temperatures for the α and β peaks.[4] The base composition $La_{60}Ni_{15}Al_{25}$ shows a pronounced β-relaxation peak separated by 116 K from the α-relaxation peak. The β peak becomes a shoulder when lower mobility Cu atoms partially replace La, Ni or Al atoms.

The bulk crystallinity of the as-cast and re-melted samples was checked by XRD and DSC. Figure 3.2a shows the XRD data for the as-cast and re-melted samples. XRD patterns for the as-cast samples (top panel) of the four compositions show a broad hump at ~ 32^o, characteristic of the amorphous state. After one cycle of re-melting, the XRD patterns show many sharp peaks (bottom panel), indicating that all the samples are crystallized in the bulk. Similar observations are made in DSC measurements (Figure 3.2b). Glass transition and crystallization peaks are clearly seen in DSC patterns of the as-cast amorphous samples (top panel) while they have disappeared after one cycle of re-melting (bottom panel). $La_{60}Ni_{15}Al_{15}Cu_{10}$ has the most complex crystallization transition with three DSC peaks (dark blue trace in Fig. 3.2b). For $La_{60}Ni_{15}Al_{15}Cu_{10}$, the bulk XRD pattern for the 1x re-melted sample is similar to the 3x re-melted sample. However, the crystalline grain size grows after successive re-melting as shown in Fig. 3.9.

We investigate the surface dynamics of the four compositions by making STM movies of the as-cast and re-melted surfaces obtained by freshly exposing bulk glass to the surface. Clusters, *ca.* 5 glass-forming units (equal to weighted atomic diameters for MGs) in diameter, hop in a two-state fashion on the as-cast surfaces. Figure 3.3a shows STM images of a two-state cluster (circled) on the $La_{60}Ni_{15}Al_{15}Cu_{10}$ as-cast surface with the complete time trace shown in Figure 3.3b. Examples of two-state clusters on as-cast surfaces of other compositions are shown in Figure 3.7.[19] In contrast to the bulk, which is crystallized after one cycle of re-melting, the surface of $La_{60}Ni_{15}Al_{15}Cu_{10}$ remains amorphous after two re-melting cycles. Clusters on the $La_{60}Ni_{15}Al_{15}Cu_{10}$ surfaces re-melted 1x and 2x still hop in a two-state fashion, as shown in Figure 3.3c-d and Figure 3.3e-f, respectively.

Surface topography and crystallinity were extensively investigated by scanning at least 15 areas, and at least 20 images/area for each sample composition. Typical large scale images of the surfaces before and after re-melting are shown in Figure 3.4. All as-cast surfaces (Figure 3.4a,c,e,g) consist of randomly distributed clusters with diameters of ~4-5 average atomic diameters (Table 3.1), similar to surfaces of other MGs and amorphous materials.[6,9-11] After one cycle of re-melting, the surfaces of $La_{60}Ni_{15}Al_{25}$, $La_{50}Ni_{15}Al_{25}Cu_{10}$ and $La_{60}Ni_{10}Al_{25}Cu_5$ crystallized, as evidenced by regular patterns (Figure 3.4b), ribbons (Figure 3.4d) and flat terraces (Figure 3.4f). The periodicity on the right side of Figure 3.4b is much larger than the size of an atom, and is comparable to the cluster diameter of the as-cast surfaces. Thus we think that this periodicity arises from surface reconstruction of the nanocrystallites into ordered patterns. An example of atomic resolution on an annealed MG surface is shown in ref. 6.

The surface of $La_{60}Ni_{15}Al_{15}Cu_{10}$ is kinetically more resistant to crystallization than its bulk as well as the surfaces of other compositions. The surface remains amorphous after two cycles of re-melting. This observation is consistent with the continued cluster hopping after re-melting observed in Fig. 3.3. Such hopping is not observed on the other surfaces after re-melting. Upon each re-melting, the clusters on the $La_{60}Ni_{15}Al_{15}Cu_{10}$ surface become larger (Figure 3.4g-i). Only after three re-melting cycles do nanocrystallites form on the crystallization-resistant surface (Figure 3.4j).

Figure 3.5a shows the cluster size distributions for as-cast surfaces of all compositions. The clusters on the as-cast surfaces of all compositions are round and have an average diameter of $\approx$ 5 atomic weighted diameters, as shown in Figure 3.5c. This result is consistent with

previous glass surface studies.[6-11,20] The cluster size distributions for as-cast, re-melted 1x and re-melted 2x surfaces of $La_{60}Ni_{15}Al_{15}Cu_{10}$ are shown in Figure 3.5b. Upon re-melting, the cluster size distribution broadens and larger clusters are observed (Figure 3.4g-i). The surface clusters become ≈ 1.4 times bigger on average after two re-melting cycles (Figure 3.5c and Table 3.1). The distribution extends with substantial shoulder in the probability distribution up to 8 average atomic diameters.

The hopping rate (number of hops per unit time and unit area) of clusters for each composition is shown in Figure 3.5d. Each data point is the average rate of ~ 15 movies. The as-cast surface of the base composition $La_{60}Ni_{15}Al_{25}$ with a pronounced β-relaxation peak has a substantially faster hopping rate than the other compositions, ≈ 2.5 times faster than $La_{60}Ni_{15}Al_{15}Cu_{10}$ and ≈ 10 times faster than $La_{50}Ni_{15}Al_{25}Cu_{10}$ and $La_{60}Ni_{10}Al_{25}Cu_5$. Upon re-melting $La_{60}Ni_{15}Al_{15}Cu_{10}$, the hopping rate decreases, suggesting that the surface has been aged. Slower hopping rates are consistent with the increase of the cluster size up to a factor of 1.4 after re-melting.

3.5. Discussion

Surface hopping of compact clusters has now been observed for a wide range of atomic glass formers, including semiconductors, metal alloys and ceramics.[6-11] Telegraph-like hopping also occurs on polymer surfaces, although the shape of the cooperatively rearranging regions has not been resolved.[21] We have also previously observed a glass surface that is stable against annealing and produces larger clusters upon annealing.[8] However, the hopping rate has not been studied systematically as a function of composition, nor has the change in hopping rate after annealing to larger clusters (aging) been quantified.

Our present data shows that the base composition with a pronounced low-temperature β-relaxation peak in Fig. 3.1 has the fastest surface hopping rate. Thus fast surface dynamics correlates with known fast bulk dynamics. In a recent study by Zhu et al.,[4] it is shown that La and Ni have the highest mobility among the four elements used in our glass samples. Atomic mobility correlates well with our average rate data for cluster hopping (Fig. 3.5). First of all, $La_{60}Ni_{10}Al_{25}Cu_5$ and $La_{50}Ni_{15}Al_{25}Cu_{10}$ have the slowest hopping rates at a smaller total concentration of La and Ni (≤70% compared to 75% of the other two compositions). In addition, $La_{60}Ni_{15}Al_{25}$ and $La_{60}Ni_{15}Al_{15}Cu_{10}$ differ only in faster-diffusing Al vs. slower-diffusing Cu

ratio, and $La_{60}Ni_{15}Al_{25}$ has the faster hopping rate. The observed correlation indicates that atomic mobility at cluster surfaces, or in interstitial spaces on the surface, translates into higher mobility of cooperatively moving regions (the clusters). If so, atomic mobility facilitates the relaxation of surface clusters, which have α-like shape, but β-like speed. The two types of dynamics may be indistinguishable at surfaces,[10] or string-like β-relaxations may simply be too fast for us to observe.

$La_{60}Ni_{15}Al_{15}Cu_{10}$ has more elements than $La_{60}Ni_{15}Al_{25}$. Thus it may be expected to have greater glass-forming ability. Indeed, its surface is more stable than the surface of $La_{60}Ni_{15}Al_{25}$ against crystallization. However, its surface is also more stable than that of the two slowest-hopping compositions, which also have more elements (Fig. 3.5d). Counterintuitively, the least mobile cooperatively rearranging regions do not yield the most stable glassy surface state. $La_{60}Ni_{15}Al_{15}Cu_{10}$ has a complex re-crystallization transition (three strong peaks in the blue trace of Fig. 3.2b), and this may kinetically hinder recrystallization of the surface, even though crystallite grain size grows in the bulk upon every heating cycle (Fig. 3.9).

Higher stability of surface glass than bulk glass, observed before in some studies,[8] is contrary to other studies showing that the crystallizations on the surface of glasses is orders of magnitude faster than in the bulk.[22,23] However, in those studies an up to micrometer thick surface layer was considered, whereas we look only within a few nm of the surface by STM. On the other hand, our glass surface stability result is in agreement with Tanaka et al.,[24] who concluded that "crystal formation in a glassy material should induce extensional stress (negative pressure) around a nucleated crystal due to the volume contraction upon crystallization, which should provide the free volume to the particles surrounding the crystal, increase their mobility, and help further crystallization." Thus crystallization could be slower at the surface compared to in the bulk because tension is less important at the exposed surface. Our result of a kinetically stable glass surface also agrees with our previous study on Ce-based MG[8] and Wang's study,[25] although their glass film crystallizes in one cycle when annealing near T_m, while ours will not.

The slower hopping rate (Fig. 3.5d) and larger cluster size (Fig. 3.4g-j) after re-melting of $La_{60}Ni_{15}Al_{15}Cu_{10}$ indicates that the surface is well-aged. We observe an ultimate cluster size of 8 glass-forming units instead of 5 for the freshly exposed bulk surface, or a factor 1.4 cluster size increase in average. This raises the issue as to whether there is an ultimate size limit for cooperatively rearranging regions before they form regular patterns and crystalline areas on the

surface. At sizes ≥8 clusters may build up sufficient strain energy from imperfect bonding that crystal nucleus formation and crystallization are unavoidable, by analogy to a spinodal point for bulk phases. If this is indeed the case, the amplitude of β-relaxation should be reduced. Suppression of β-relaxation upon annealing agrees well with other studies.[26,27] Unfortunately, currently we cannot measure the analog of Fig. 3.1 (in the bulk) for the glass surface.

In summary, systematic compositional variation shows that local atomic mobility and global cooperative mobility are correlated on atomic glass surfaces. One composition, albeit not the one with lowest surface hopping, was even robust against re-melting, and reconstructs to clusters about 1.4x larger than in the freshly exposed bulk, perhaps representing an upper limit before the probability of a crystallization nucleus in or on a cluster becomes too large.

3.6. Supplementary information

3.6.1. Cluster size analysis

Diameters of clusters were measured following the procedure in ref. 10 in the main text. For each surface, 100 random points were generated in the image being analyzed and clusters closest to the points were measured. The cluster diameters were taken as the average of the measured width and length in x and y directions. The diameters in nm were then converted to the atomic weighted diameter (AWD) (or glass-forming unit). For calculations of the AWD, the following atomic diameters were used: 0.187 nm for La, 0.124 nm for Ni, 0.143 nm for Al and 0.128 nm for Cu. The AWDs for $La_{60}Ni_{15}Al_{25}$, $La_{50}Ni_{15}Al_{25}Cu_{10}$, $La_{60}Ni_{10}Al_{25}Cu_{5}$ and $La_{60}Ni_{15}Al_{15}Cu_{10}$ are 0.333 nm, 0.321 nm, 0.334 nm and 0.330, respectively. The cluster size distributions were calculated by histogramming all the measured diameters, with binning of 1 AWD.

3.6.2. Average rate analysis

Average rate was analyzed by counting number of hops per unit time per unit area. For each surface, ≈ 15 movies were analyzed.

3.7. Movies

Movie 3.1: Complete STM movie for the cluster in Fig. 3.3c. Scanning conditions: 10 pA, 1 V. STM image sizes: 10.4 nm x 10.4 nm. 41 s/frame. Playback rate: 1 s/frame.

3.8. Figures and tables

Table 3.1: Four glass compositions used in this study, glass transition temperature, crystallization temperature, melting temperature, location of the alpha and beta peaks from a Kohlrausch–Williams–Watts fit, cluster size, and hopping rate of the as-cast and re-melted surfaces. $T_{\beta,peak}$ and $T_{\alpha,peak}$ are reproduced from ref. 4. All temperatures are in K.

Composition	T_g	T_x	T_m	$T_{\beta,peak}$	$T_{\alpha,peak}$	Cluster size (AWD)	Average rate (hops/μm^2/s)
$La_{60}Ni_{15}Al_{25}$ (ac)	455	507	702	367 ± 1	483	4.5 ± 0.8	117 ± 14
$La_{60}Ni_{15}Al_{15}Cu_{10}$ (ac)	412	464	670	373 ± 2	441	4.7 ± 1.0	48 ± 9
$La_{60}Ni_{15}Al_{15}Cu_{10}$ (re 1x)	-	-	-	-	-	5.5 ± 1.4	21 ± 5
$La_{60}Ni_{15}Al_{15}Cu_{10}$ (re 2x)	-	-	-	-	-	6.4 ± 1.8	20 ± 5
$La_{60}Ni_{15}Al_{15}Cu_{10}$ (re 3x)*	-	-	-	-	-	-	5.2 ± 0.3
$La_{60}Ni_{10}Al_{25}Cu_5$ (ac)	442	493	663	382 ± 2	472	4.6 ± 0.8	13 ± 4
$La_{50}Ni_{15}Al_{25}Cu_{10}$ (ac)	464	537	671	414 ± 3	491	4.8 ± 0.9	13 ± 3

**Crystallized surface. Do not count crystalline movements such as row, big blob hopping. ac = as-cast. re = re-melted.*

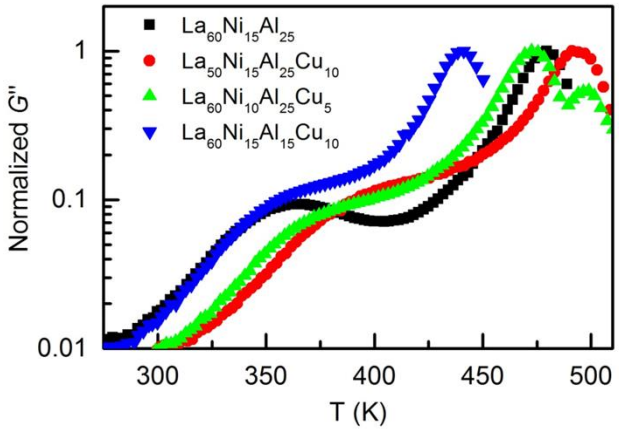

Figure 3.1: Isochronal DMA. The testing frequency is 1 Hz. $La_{60}Ni_{15}Al_{25}$ shows a pronounced β-relaxation peak. The other three compositions $La_{50}Ni_{15}Al_{25}Cu_{10}$, $La_{60}Ni_{10}Al_{25}Cu_5$ and $La_{60}Ni_{15}Al_{15}Cu_{10}$ show a shoulder. Data is reproduced from ref. 4.

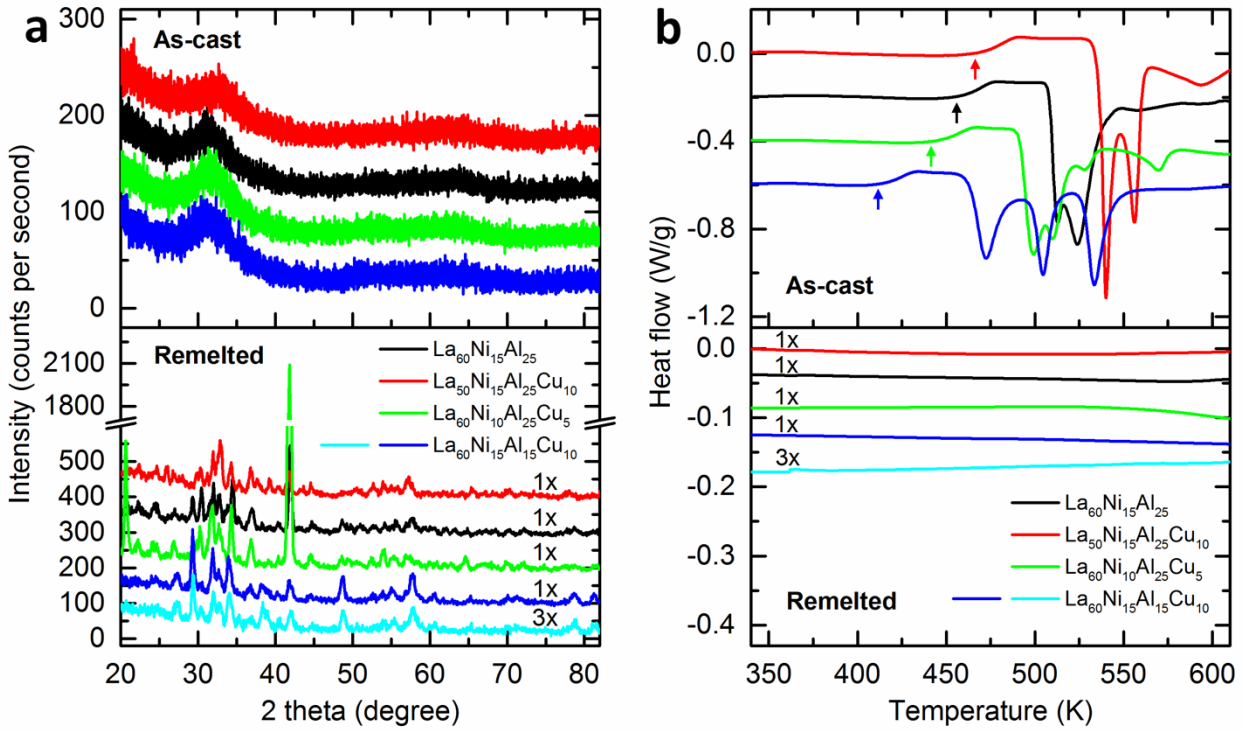

Figure 3.2: XRD and DSC characterizations. (a) XRD of as-cast (top) and re-melted (bottom) samples. After one cycle of re-melting, the bulk is already crystallized for all compositions. For $La_{60}Ni_{15}Al_{15}Cu_{10}$, XRD patterns for the re-melted 1x sample is similar to the re-melted 3x sample. (b) DSC of as-cast (top) and re-melted (bottom) samples. The arrows highlight the glass transition. The glass transition and crystallization peaks disappear after one cycle of re-melting for all compositions.

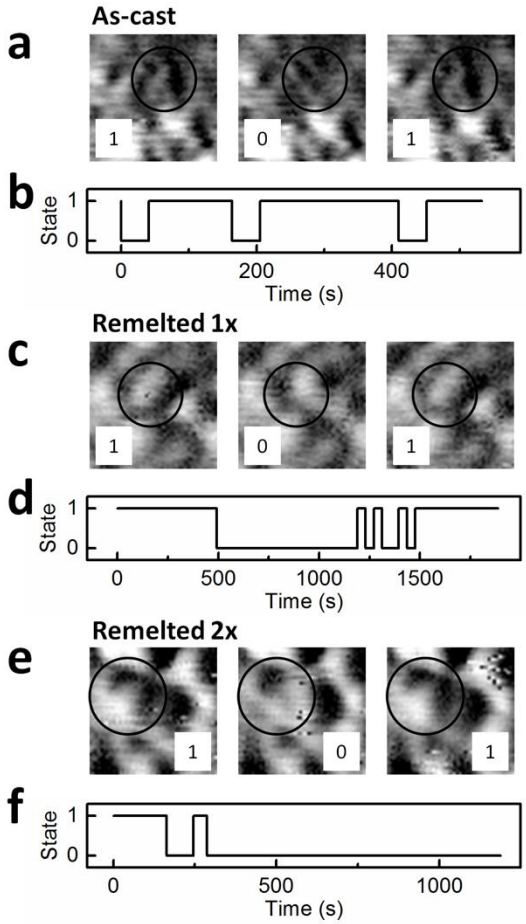

Figure 3.3: Two-state motions on as-cast and re-melted $La_{60}Ni_{15}Al_{15}Cu_{10}$ surfaces. (a), (c), (e) STM derivative images of two-state clusters (circled) with corresponding time traces in (b), (d), (e). Scanning conditions: 10 pA, 1 V. All STM image sizes: 6 nm x 6 nm.

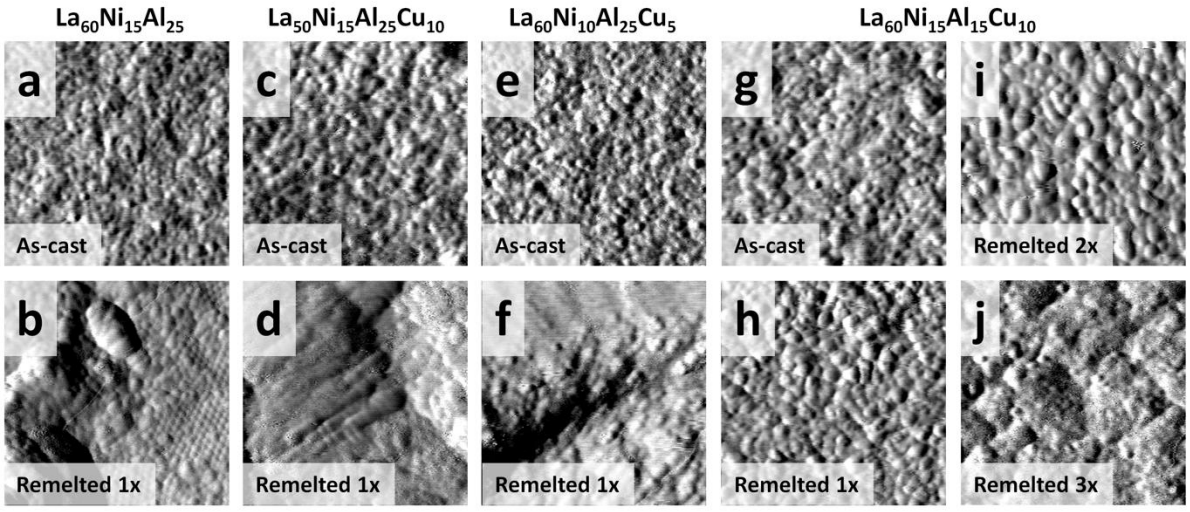

Figure 3.4: Topography of the as-cast and re-melted surfaces. (a)-(b) $La_{60}Ni_{15}Al_{25}$, (c)-(d) $La_{50}Ni_{15}Al_{25}Cu_{10}$, (e)-(f) $La_{60}Ni_{10}Al_{25}Cu_5$ and (g)-(j) $La_{60}Ni_{15}Al_{15}Cu_{10}$. The surface is amorphous in a, c, e, g-i. In b, d, f and j, the surface is crystalline, evidence as regular patches (b), ribbons (d), flat terraces (f) and nanocrystallites (j). Scanning conditions: 50 pA, 1 V. All STM derivative image sizes: 40 nm x 40 nm.

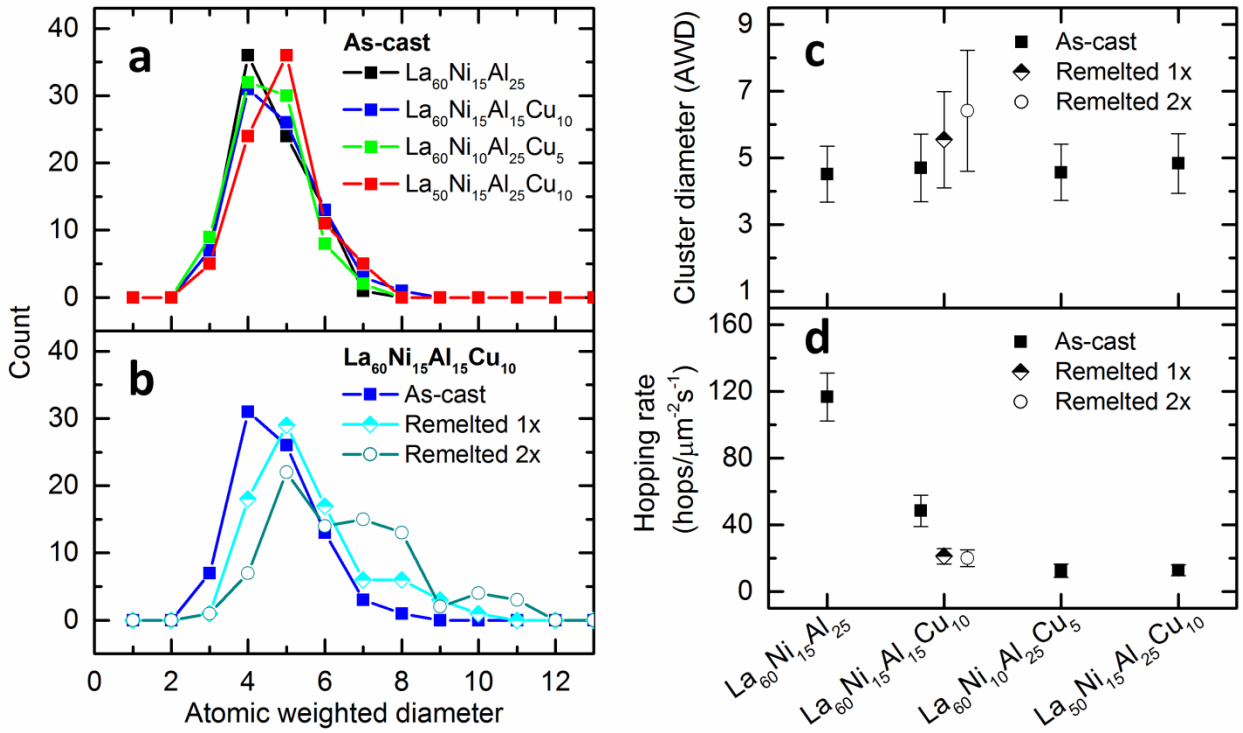

Figure 3.5: Cluster size and rate analysis. (a) Cluster size distributions for as-cast surfaces of $La_{60}Ni_{15}Al_{25}$, $La_{50}Ni_{15}Al_{25}Cu_{10}$, $La_{60}Ni_{10}Al_{25}Cu_5$ and $La_{60}Ni_{15}Al_{15}Cu_{10}$. (b) Cluster size distributions for as-cast and re-melted surfaces of $La_{60}Ni_{15}Al_{15}Cu_{10}$. (c) Average cluster size and (d) average hopping rate as a function of composition.

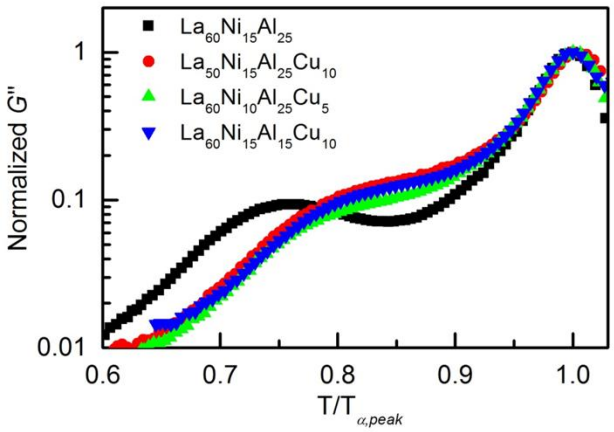

Figure 3.6: Isochronal DMA. Same as in Fig. 3.1 but T is normalized to $T_{\alpha,peak}$.

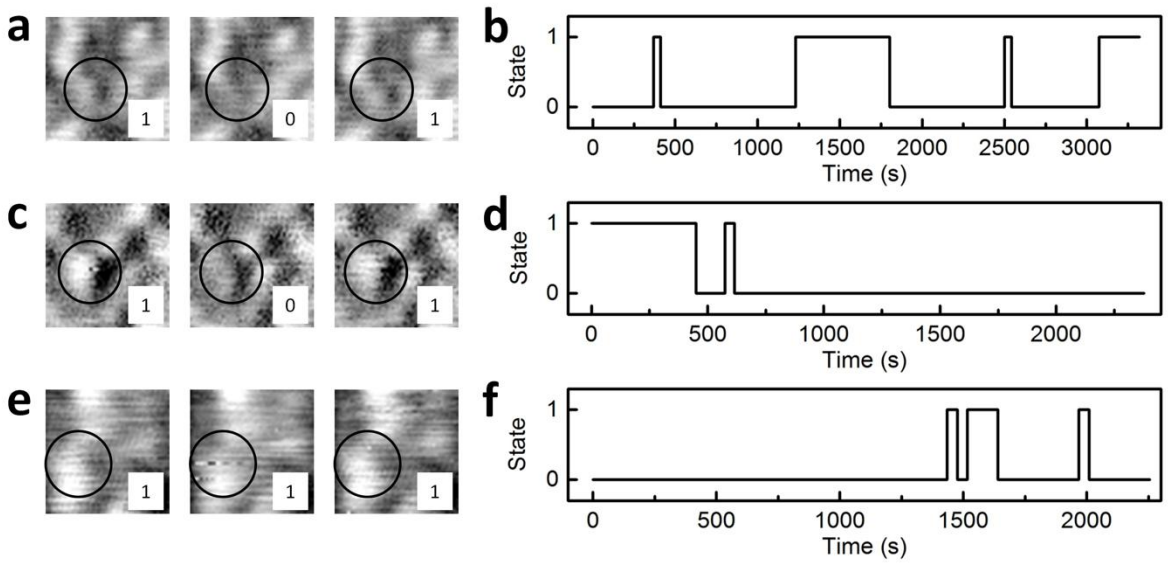

Figure 3.7: Two-state clusters and time traces on the surface of other compositions. (a)-(b) $La_{60}Ni_{15}Al_{25}$ (as-cast), (c)-(d) $La_{50}Ni_{15}Al_{25}Cu_{10}$ (as-cast), (e)-(f) $La_{60}Ni_{10}Al_{25}Cu_5$ (as-cast). Scanning conditions: 10 pA, 1 V. All STM derivative image sizes: 6 nm x 6 nm.

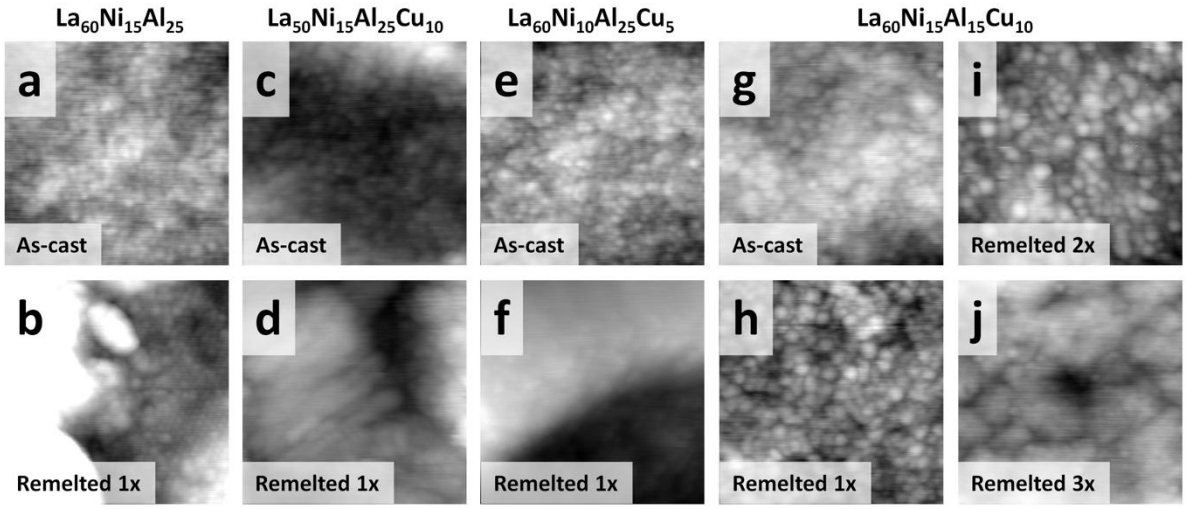

Figure 3.8: The corresponding topographic version of Fig. 3.4.

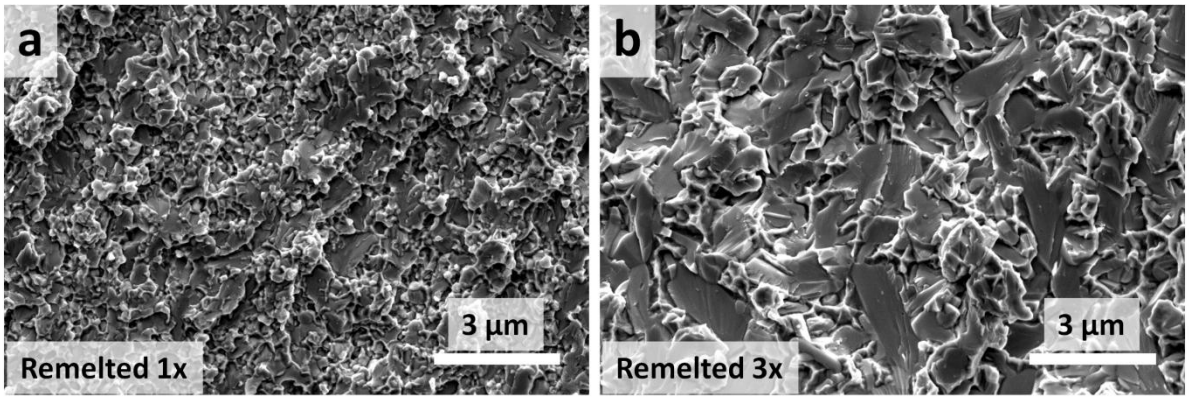

Figure 3.9: SEM images of the bulk fracture surfaces of the $La_{60}Ni_{15}Al_{15}Cu_{10}$ samples after remelting (a) 1 cycle and (b) 3 cycles. The crystalline grain size increases after successive remelting.

3.9. References

1. A. L. Greer, Science, 267, 1947–1953 (1995).
2. P. G. Debenedetti and F. H. Stillinger, Nature, 410, 259–267 (2001).
3. M. K. P. Lunkenheimer S. Kastner, and A. Loidl, in Structural Glasses and Supercooled Liquids: Theory, Experiment, and Applications, ed. V. L. Peter G. Wolynes, Wiley, First., pp. 115–150 (2012).
4. Z. G. Zhu, Y. Z. Li, Z. Wang, X. Q. Gao, P. Wen, H. Y. Bai, K. L. Ngai and W. H. Wang, J. Chem. Phys., 141, 084506 (2014).
5. V. Lubchenko and P. G. Wolynes, Ann. Rev. Phys. Chem., 58, 235–266 (2007).
6. S. Ashtekar, G. Scott, J. Lyding and M. Gruebele, J. Phys. Chem. Lett., 1, 1941– 1945 (2010).
7. S. Ashtekar, J. Lyding and M. Gruebele, Phys. Rev. Lett., 109, 166103 (2012).
8. S. Ashtekar, D. Nguyen, K. Zhao, J. Lyding, W. H. Wang and M. Gruebele, J. Chem. Phys., 137, 141101 (2012).
9. S. Ashtekar, G. Scott, J. Lyding and M. Gruebele, Phys. Rev. Lett., 106, 235501 (2011).
10. D. Nguyen, J. Mallek, A. N. Cloud, J. R. Abelson, G. S. Girolami, J. Lyding and M. Gruebele, J. Chem. Phys., 141, 204501 (2014).
11. D. Nguyen, L. Nienhaus, R. T. Haasch, J. Lyding and M. Gruebele, J. Chem. Phys., 142, 234505 (2015).
12. J. D. Stevenson and P. G. Wolynes, J. Chem. Phys., 129, 234514 (2008).
13. Z. Fakhraai and J. A. Forrest, Science, 319, 600–604 (2008).
14. Y. Chai, T. Salez, J. D. McGraw, M. Benzaquen, K. Dalnoki-Veress, E. Raphaël and J. A. Forrest, Science, 343, 994–9 (2014).
15. W. H. Wang, C. Dong and C. H. Shek, Mater. Sci. Eng. R, 44, 45–89 (2004).
16. Q. Wang, S. T. Zhang, Y. Yang, Y. D. Dong, C. T. Liu and J. Lu, Nat. Commun., 6, 7876 (2015).
17. H. B. Yu, K. Samwer, W. H. Wang and H. Y. Bai, Nat. Commun., 4, 2204 (2013).
18. J. W. Lyding, S. Skala, J. S. Hubacek, R. Brockenbrough and G. Gammie, Rev. Sci. Instrum., 59, 1897–1902 (1998).
19. See supplemental materials for data analysis methods and more examples of cluster dynamics.

20. J. A. J. Burgess, C. M. B. Holt, E. J. Luber, D. C. Fortin, G. Popowich, B. Zahiri, P. Concepcion, D. Mitlin and M. R. Freeman, arXiv:1409.5111, 2014. 10
21. E. V Russell and N. E. Israeloff, Nature, 408, 695–698 (2000).
22. Y. Sun, L. Zhu, K. L. Kearns, M. D. Ediger and L. Yu, Proc. Natl. Acad. Sci. U. S. A., 108, 5990–5995 (2011).
23. C. R. Cao, Y. M. Lu, H. Y. Bai and W. H. Wang, Appl. Phys. Lett., 107, 141606 (2015).
24. H. Tanaka, Phys. Rev. E. Stat. Nonlin. Soft Matter Phys., 68, 011505 (2003).
25. C. R. Cao, K. Q. Huang, N. J. Zhao, Y. T. Sun, H. Y. Bai, L. Gu, D. N. Zheng and W. H. Wang, Appl. Phys. Lett., 105, 011909 (2014).
26. J. Qiao, R. Casalini and J.-M. Pelletier, J. Chem. Phys., 141, 104510 (2014).
27. H. B. Yu, M. Tylinski, A. Guiseppi-Elie, M. D. Ediger and R. Richert, Phys. Rev. Lett., 115, 185501 (2015).

4. Sub-nanometer glass surface dynamics induced by illumination

This chapter is reproduced from D. Nguyen, L. Nienhaus, R. T. Haasch, J. Lyding and M. Gruebele, Sub-nanometer glass surface dynamics induced by illumination, *J. Chem. Phys.*, 2015, 142, 234505, with the permission of AIP Publishing.

4.1. Abstract

Illumination is known to induce stress and morphology changes in opaque glasses. Amorphous silicon carbide (a-SiC) has a smaller bandgap than the crystal. Thus, we were able to excite with 532 nm light a 1 μm amorphous surface layer on a SiC crystal while recording time-lapse movies of glass surface dynamics by scanning tunneling microscopy (STM). Photoexcitation of the a-SiC surface layer through the transparent crystal avoids heating the STM tip. Up to 6×10^4 s, long movies of surface dynamics with 40 s time resolution and sub-nanometer spatial resolution were obtained. Clusters of ca. 3-5 glass forming units diameter are seen to cooperatively hop between two states at the surface. Photoexcitation with green laser light recruits immobile clusters to hop, rather than increasing the rate at which already mobile clusters hop. No significant laser heating was observed. Thus, we favor an athermal mechanism whereby electronic excitation of a-SiC directly controls glassy surface dynamics. This mechanism is supported by an exciton migration-relaxation-thermal diffusion model. Individual clusters take ~1 h to populate states differently after the light intensity has changed. We believe the surrounding matrix rearranges slowly when it is stressed by a change in laser intensity, and clusters serve as a diagnostic. Such cluster hopping and matrix rearrangement could underlie the microscopic mechanism of photoinduced aging of opaque glasses.

4.2. Introduction

Atomic and molecular glasses are as commercially important as they are of fundamental interest: an amorphous structure combines with dynamics so slow that eons would be required to reach equilibrium.[1] Slow dynamics ordinarily requires that bulk supercooled liquids must be studied near their glass transition temperature T_g, below which rapidly increasing viscosity arrests motion and taxes the experimenter's and simulator's patience. In kinetically motivated models of the glass transition, the arrest arises when the density of "soft spots" in the glass drops

below that needed to facilitate motion over adjacent areas of the glass.[2] In thermodynamically motivated models of the glass transition, the arrest arises because particles move in ever larger collectively rearranging compact regions ("clusters") as the temperature drops, until the loss of kinetic energy and the increasing size of clusters leads to a super-Arrhenius slowdown.[3] This is predicted to occur when the collective regions in atomic and molecular glasses reach about 5 particles in diameter.[4]

A simple adaptation of the thermodynamic theory to glass surfaces predicts that similar-size clusters hop much faster on surfaces than in the bulk (surface barrier = 1/2 bulk barrier).[5] Fast hopping 3-5 particle diameter clusters have been imaged at the surface of atomic glass-formers by our group and Freeman and coworkers.[6,7] We proposed that the glass surface promotes compactness of collectively rearranging regions over the bulk because clusters are more malleable at the surface and can minimize dangling bonds by minimizing surface-to-volume ratio as the glass surface becomes arrested.[8] A full connection between glass surface and glass bulk dynamics remains to be made.

There are additional ways to speed up the rearrangements of glassy systems without looking at the surface. One can of course heat the glass;[1] one can apply mechanical stress to the glass, nudging cooperative regions out of local equilibrium;[9,10] or one can photo excite the glass, allowing electronic excitation and/or subsequent relaxation to create mechanical stress or to loosen bonds.

Photoexcitation above the bandgap has been used to "age" glasses (lower their enthalpy towards that of the crystal phase), as shown by calorimetry repeated over a period of many days.[11] Exciton recombination has been implicated in the bond breaking and making of photoexcited Se glass, leading to aging below T_g.[12] Such aging has been taken to the ultimate limit by laser-induced crystallization of SeSb glass.[13] Fragile glasses (with a stronger temperature dependence of viscosity near T_g and a less coordinated bonding network) undergo more extensive photorelaxation and explore a larger number of minima when subject to illumination.[14]

Here, we use sub-nanometer surface imaging to study how laser-photoexcitation speeds up glass surface dynamics. Scanning tunneling movies reveal that photoexcitation induces cluster hopping at the amorphous silicon carbide (a-SiC) surface deep in the glassy regime ($T << T_g$). We quantify the probability distribution of the size of clusters. This shows that immobile clusters

are on average one glass forming unit (GFU) (here, a Si-C tetrahedron as seen in Fig. 4.1(b)) larger than clusters that do hop, irrespective of whether the sample is illuminated or not. We show that clusters switch from being semiconducting to metallic conduction when they are optically excited. This holds true for larger immobile clusters, as well as for smaller clusters that hop between two sites. A long surface movie (6×10^4 s with $>10^3$ frames) shows that the relative stability of the two energy landscape minima that are explored by a cluster changes upon photoexcitation, but not the activation barrier for hopping. We show that photoexcitation activates immobile clusters, rather than speeding up the hopping of already mobile clusters. We measure <1 K laser heating at the surface. Based on these observations, we favor an electronic activation model for the photoexcited glass surface dynamics (Fig. 4.1(c), left) over a purely thermal model (Fig. 4.1(c), right). A numerical calculation that incorporates electronic excitation by the laser, diffusion of excitons, decay into phonons, and heat transport through the a-Si and c-Si shows that the model is plausible.[15] We also see some evidence of cooperative behavior: a laser power threshold in the activation of immobile clusters. This could only be explained by long-lived surface traps for electronic excitation, which have been observed for other semiconductor nanoclusters.[16]

4.3. Methods

n-type 4H-SiC (Cree, Inc., resistivity ≈ 0.013-0.500 Ω cm) was used in this study. To reduce tip heating and thus allow stable imaging under laser illumination, a total internal reflection geometry was used. 45° right angle fused silica prisms were attached to the back of the samples using 302-3M epoxy and cured for 24 h at room temperature. The samples were then degassed at ~380 K for 12-15 h. The amorphous a-SiC surface layer was produced by sputtering with 2 keV argon ions for 22-27 h, with a dose of ~1-10 × 10^{16} ions/cm^2 s^{-1}. Argon base pressure during sputtering was ≤3 × 10^{-3} Pa. Sputtered samples were then immediately transfer to the attached UHV scanning tunneling microscopy (STM) chamber.

XPS shows that the C:Si ratio on the surface is 0.58:0.42 after sputtering,[15] which is in good agreement with a previous study.[17] This surface composition corresponds to an optical gap of ~2.2 eV.[18,19] There is less than 3% of Ar embedded into the surface.[15] There is also less than 1% of Fe contamination in the sputtered samples due to sample handling and preparation. Cross

section SEM shows that the thickness of the amorphous layer is ~1.27 μm,[15] much deeper than the size of the cooperative clusters discussed below.

Movies of glass surface dynamics were collected by repeatedly scanning over about the same area for about 40 s by a home-built, ultra-stable UHV STM[20] with base pressure $\leq 7 \times 10^{-9}$ Pa and electrochemically etched tungsten tips. Achieving high stability is important in order to make movies as long as ~20 h of areas as small as 13 nm × 13 nm with sub-nm resolution. We verified that hopping rates at 10 pA and 50 pA tunneling current are similar, indicating that the cluster motion is independent of the scanning current. 532 nm laser light was absorbed by the amorphous layer[15] after passing through the transparent crystalline substrate, with total internal reflection at the surface virtually eliminating tip heating. The calibrated laser power density[15] can be tuned slowly from ~150 to ~1500 mW/mm^2 while scanning image frames of the STM movie. The laser spot size on the sample is approximately 0.1 mm in diameter. We have noted field enhancement factors up to $f \approx 4$ from tungsten tips in the past, so the surface laser intensity near the tip may be somewhat enhanced.[21]

To check the plausibility of our proposed model, we numerically simulated exciton diffusion and heat transfer using the following two equations:

$$\frac{\partial \rho_{ex}(z,t)}{\partial t} = \frac{\partial}{\partial z} D_{ex}(z) \frac{\partial \rho_{ex}(z,t)}{\partial z} - \frac{\rho_{ex}}{\tau_{ex}} + \frac{I_0}{(hc/\lambda)} e^{-z\alpha(I(z))} \alpha_0 \frac{I_s}{I(z)+I_s} \tag{4.1}$$

and

$$\frac{\partial T(z,t)}{\partial t} = \frac{1}{\rho c_p} \left(\frac{\partial}{\partial z} k(z) \frac{\partial}{\partial z} T(z,t) + \frac{\rho_{ex}}{\tau_{ex}} \frac{hc}{\lambda} \right). \tag{4.2}$$

ρ_{ex} is the exciton density. Equation (4.1) describes exciton diffusion (first term on right side), exciton decay into phonons (second term), and exciton generation by optical excitation (third term). D_{ex} is the exciton diffusion coefficient ($\approx 10^{-3}$ m^2 s^{-1} in c-SiC and a-SiC),[22] τ_{ex} is the bulk exciton lifetime (≈1 ps),[23] I_0 is the incident laser intensity, I_s is the saturation intensity (≈1000 mW/mm^2), and α_0 is the absorption coefficient obtained from transmission measurements ($\approx 5.33 \times 10^5$ m^{-1}).[15] The third term takes into account optical saturation. Equation (4.2) describes the temperature gradient resulting from thermal diffusion. k is the thermal conductivity measured by the 3ω method (330 W m^{-1} K^{-1} in c-SiC and a-SiC). Boundary conditions were exciton density ρ_{ex} = 0 excitons/nm^3 and T = 295 K in the vacuum above the sample and in the c-SiC far

from the absorbing a-SiC layer. Further details of the numerical integration are given in the supplementary material.[15]

4.4. Results

We observed two-state dynamics on the surface of a-SiC with or without photoexcitation. Fig. 4.2(a) shows a cluster (ca. 3 GFU in diameter) hopping between two states "1" and "−1" when the laser is off. Its single-particle time trace is shown in Fig. 4.2(b). Another two-state cluster (ca. 4 GFU in diameter) imaged under photoexcitation is shown in Fig. 4.2(c). Reproducible cluster substructure is resolved over the course of several hops, indicating the cooperative nature of the motion of multiple GFUs within a cluster. The time trace for the cluster in Fig. 4.2(c) is shown in Fig. 4.2(d).

The bandgap of our c-SiC substrate surface is ∼2.8 ± 0.1 eV (bottom panel of Fig. 4.2(e)). The observed surface bandgap of c-SiC is smaller than the bulk value of ∼3.2 eV as a result of surface reconstruction.[24] Both c-SiC bandgaps are larger than the excitation laser energy (2.33 eV at 532 nm wavelength), so the substrate is transparent to the laser. The measured surface bandgap of a-SiC is only 1.8 ± 0.3 eV, also smaller than the reported value for bulk a-SiC (∼2.2 eV),[18] possibly due to surface reconstruction or dangling bonds. The a-SiC bandgaps are smaller than the laser excitation energy, so only the 1 μm thick surface a-SiC layer absorbs light (Fig. 4.1(a)).

The a-SiC surface can be photoexcited and subsequently relaxes reversibly over a few illumination cycles (Fig. 4.2(e)). The excitation and relaxation are monitored by scanning tunneling spectroscopy (STS). a-SiC is an indirect gap material and therefore has semiconducting STS characteristics. When it is excited, the STS becomes metallic due to free conduction band carriers. Fig. 4.2(e) shows a series of STS measured on the same cluster area, with the light off-on-off-on and the STS going semiconducting-metallic-semiconducting-metallic.

Fig. 4.3 shows hopping of a two-state cluster (ca. 3 GFU in diameter) imaged while under 532 nm laser illumination (a = topographic mode, b = derivative images). The two-state single particle trajectory for this cluster is shown in Fig. 4.3(c) (black trace), along with the time-dependence of the laser power (red trace). The cluster motion was imaged while the power density at the surface was decreased from ≈390 to ≈190 mW/mm^2. At higher power density, the

cluster visits both states "1" and "−1" with about equal probabilities p_1 and p_{-1} and dwell time ratio $R = p_{-1}/p_1 \approx 1.23$. The dwell time ratio R of this optically driven out-of-equilibrium system is the analog of the equilibrium constant K_{eq} in an equilibrium system. The relaxation rate is given by $k_{obs}=\langle 1/t_{-1}\rangle+\langle 1/t_1\rangle\approx 0.02$ s^{-1}, where $t_{\pm 1}$ is the dwell time in state ± 1.[15] After decreasing the illumination power density, the cluster visits mostly state "−1" with $R \approx 5.32$, but $k_{obs} \approx 0.02$ s^{-1} remains unchanged. Both relaxation rates are somewhat faster than 0.02 s^{-1} because the tip misses transitions while scanning elsewhere in the image, an effect we have considered quantitatively elsewhere.[6]

Fig. 4.3(d) shows the dwell time distributions for the cluster in Fig. 4.3(c) at 390 mW/mm^2 (0–12 000 s). The kinetics appear to be homogeneous, and the dwell time distributions are fitted well by single exponential decays. The Kolmogorov-Smirnov test[25] can be used to decide whether two segments of the time trace during constant illumination have the same underlying rates and dwell time ratios.[15] When we divide the trace from 0 to 12 000 s into 0-6000 and 6000-12 000 halves and apply the Kolmogorov-Smirnov test, a single dwell-time distribution accounts for the two halves of the data with fairly high probability ($p = 0.17$). The dwell time distributions of clusters at constant laser power (including zero power) are all consistent with activated kinetics crossing over a single barrier between two states of constant relative free energy (see supplementary material[15] for further examples).

The relative free energy of states "−1" and "1" changes when the laser power is changed. The single cluster trace in Fig.4.3(c) is obviously different in the ranges from 0 to 12 000 s (390 mW/mm^2) and from 25 000 to 58 000 s (190 mW/mm^2). Fig. 4.4(a) shows the result of the Kolmogorov-Smirnov test. The probability distributions of $\ln(R)$ and $\ln(k_{\text{obs}})$ for the high power and low power segments of the trace in Fig. 4.3(c) are well separated. The probability that these two parts of the trace arise from a common underlying distribution is $p < 10^{-10}$.

Illumination changes the dwell time ratio, but not the relaxation rate of the cluster in Figs. 4.3 and 4.4(a). This result is general. Fig. 4.4(b) shows the hopping rate averaged over several surface areas (black circles). Above a threshold laser intensity, the average rate increases by a factor of 2.5-3 and eventually saturates at high laser intensity. However, the average rate simply tracks the number of newly hopping clusters (blue circles). Photoexcitation mobilizes formerly immobile clusters, rather than speeding up already mobile clusters. In addition, for the cluster in Fig. 4.3(c), the measured surface temperature decrease after the power drop is <1

K.[15] The lack of laser heating and the constant hopping rate of individual clusters when laser intensity changes indicate an athermal activation mechanism.

Some clusters are mobile, but most clusters remain immobile. One might expect larger clusters to have slower kinetics, so we examined the cluster size distributions for mobile and immobile clusters on the a-SiC surface. The distributions for our samples are shown in Fig. 4.4(c). The hopping clusters have an average diameter of 3.8 GFUs with a spread of 0.9 (standard deviation). Non-hopping clusters are about 1.1 GFU larger (4.9 GFUs with a spread of 1.2). Is that enough of a difference on average? According to the glass surface version of the random first-order transition (RFOT) model, for example, the surface activation barrier is proportional to $(r^*)^{1.5}$ where r^* is the length scale of activated motions.[3,5] For a 3.8 to 4.9 GFU size increase, that scaling raises the average barrier height from $\approx 4.25\, k_B T_g$ (observed in Fig. 4.4(a)) to $\approx 6.3\, k_B T_g$. $T_g \approx 2000$ K for a-SiC, so at room temperature, a 1.1 GFU size increase accounts for $\sim 10^6$ times slower hopping. That would indeed make the larger clusters seem immobile within our experimental measurement range. Previous bulk experiments,[26] as well as cluster-resolved experiments,[27] have also showed such a slow-down of kinetics for more "aged" glasses or larger surface clusters.

However, the size distributions of mobile and immobile clusters in Fig. 4.4(c) overlap. Some smaller clusters do not move while some larger ones do. a-SiC is a network material and thus a strong glass former. The relevant bond energies are roughly 3.6 eV (C–C), 3.3 eV (Si–C, with strong charge exchange[28] $Si^{+1.4}C^{-1.4}$), and 2.3 eV (Si–Si). Cooperative clusters of 3-5 GFU diameter (containing ca. 30-120 Si and 30-120 C atoms) cannot move if even a single net bond to the surrounding matrix must be broken completely, or replaced by a much weaker bond. Thus, we believe that cluster-specific bonding plays a role in mobility also, and net bond breaking with high endothermicity prevents clusters from moving even if they are small.

Does a cluster's mobility depend on that of other nearby clusters? As a step towards computing the four-point correlation function for the dynamics of a pair of clusters, each hops between a pair of positions, we examined the simultaneous hopping of two nearby clusters. Fig. 4.12[15] shows the dynamics of a cluster ca. 1.0 nm from the cluster in Fig. 4.3(a) (closest pair found). If the traces are completely correlated, their product would have an average value of 1; if anticorrelated, −1. Instead, the product has an average of 0.08 (*vs.* −0.33 and −0.25 for the traces themselves, which favor the "−1" state), indicating no significant correlation. Since the cluster in

Fig. 4.12[15] hops more slowly than the one in Fig. 4.3, we also investigated whether the rate of the faster-hopping cluster is modulated by the state the slower cluster is in. The number of switches per frame of the fast cluster is 0.34 ± 0.04 while the slow cluster is down, 0.33 ± 0.04 while it is up, again without a statistically significant difference. Thus, we conclude that the motions of these two clusters are not correlated significantly over short timescales ~(1/k). Of course, there could still be long-term correlation, say over hours.

An additional more speculative observation from the data in Fig. 4.3(c) (another example is shown in Fig. 4.11 in the supplementary material[15]) is the existence of hysteresis for 0.5-2 h. After the laser power was dropped, the cluster continued to hop for quite a while as though nothing happened, and only then did its dwell time ratio shift from state "1" towards "−1". We believe that changing the laser power density induces a small mechanical stress on the glass surface. The whole surface then takes 0.5-2 h to structurally settle, but with small structural shifts distributed over a large surface area. These are hard to detect directly by STM. The change of cluster dwell time ratio could be a sensitive diagnostic for settling of the surface subject to stress, so photoexcitation-cycling could be useful for studying aging at the atomic level through stress-relaxation cycles.

4.5. Discussion

Based on our observations, clusters of diameter 3-5 GFUs hop on the a-SiC surface in a two state fashion. The clusters do switch from semiconducting to metallic when the laser is turned on during scanning tunneling spectroscopy, in keeping with excitation of carriers to the conduction band. Laser surface heating is negligible (<1 K), but we observe a shift in the two state equilibrium of individual clusters when the illumination intensity is changed. The number of hopping clusters also increases with laser intensity, even if individual clusters are not hopping significantly faster.

These observations favor an athermal model of cluster activation, as illustrated in Fig. 4.1. Laser light produces an electronic excitation (e.g., an exciton). Bulk excitons decay rapidly into phonons ($\tau_{ex} \approx 1$ ps),[23] but with a diffusion coefficient of $D_{ex} \approx 10^{-3}$ m^2 s^{-1},[22] excitons can diffuse tens of nm before being relaxed. Thus, excitons easily can reach a cluster surface and activate bonds. The measured temperature increases at the a-SiC surface is negligible, ruling out the heating mechanism.

To test whether this model is plausible, we performed numerical simulations of exciton formation, diffusion, and decay, as well as the resulting heat diffusion through the c-SiC and a-SiC. Assuming uniform illumination, we integrated the one-dimensional model (z-axis in Fig. 4.1(a)) in Eqs. (4.1) and (4.2) by using the literature values for diffusion coefficients and decay times listed above and in Sec. 4.3. The steady-state solutions with I_0 = 2240 mW/mm^2 entering the prism in Fig. 4.1(a) (corresponding to ≈1120 mW/mm^2 at the a-SiC front surface) give an exciton density of $\sim 10^{-10}$ excitons/nm^3 and a temperature increase of ≪1 K at the surface. Even increasing the intensity by $f^2 \approx 16$ to account for tip field enhancement does not raise the temperature by >1 K.[15] The small increase of temperature is in good agreement with the experimental data for average surface heating in Fig. 4.8.[15] The calculated steady-state exciton generation rate is $\sim 10^2$-10^3excitons/nm^3 s^{-1}.[15] Thus, many excitons will visit each cluster surface during the >40 s time between hopping events, making activation of surface bonds by electronic excitation plausible.

The model in Eqs. (4.1) and (4.2) predicts saturation of the rate with laser intensity, but it does not predict an intensity threshold. We fitted the data in Fig. 4.4(b) to a simple saturation model,

$$k_{\text{obs}} = k_0 + \alpha I^n / (I_s^n + I^n) \tag{4.3}$$

with n = 1 and I_s = 1000 mW/mm^2. The model roughly represents the trend in the hopping rate with laser intensity (solid curves in Fig. 4.4(b)). Although the data in Figure 4.4(b) are noisy, the simple saturation model seems to fall outside the measurement uncertainty. There is a threshold in the laser intensity dependence. A correspondingly better fit was obtained with n = 4 and I_s = 600 mW/mm^2 (dashed lines). One interpretation of the better fit is that roughly 4 excitons formed upon laser illumination are required for a cluster to hop. This is sensible in terms of several bonds requiring activation at the surface for hopping to occur, but it is implausible with a calculated exciton formation rate of ≈1 exciton per cluster per millisecond and an exciton relaxation time of τ_{ex} = 1 ps. The probability of even just two excitons existing simultaneously in a cluster would be $p < 10^{-9}$. However, experiments have verified the existence of long-lived excitons, trapped at the surface of semiconductor nanocrystals for several seconds.[16] If millisecond electronic traps existed on the surface of our SiC nanoclusters, more than one exciton contributing to a cluster hop would be plausible. We have no direct evidence for such

traps other than the threshold-saturation behavior of the hopping rate vs. laser intensity in Fig. 4.4(b).

Athermal photoenhanced hopping is consistent with previous bulk studies on chalcogenide glasses. Lucas *et al.*[29] have shown that laser irradiation causes a decrease in the glass configurational entropy or "aging." The bulk effect is strong for fragile glasses and is negligible for strong glasses, but here we can look at individual moving clusters out of hundreds that are not moving. We did not observe a considerable shift in cluster size distribution with laser on vs. off (Fig. 4.4(c)), which is consistent with the expected strong nature of a-SiC as a network material. Tanaka and Hisakuni[30] proposed two mechanisms for observed photoinduced fluidity in chalcogenide glasses: interchange and weakening of the bonds. Both mechanisms are in accord with our model of nanometer scale hopping dynamics. Lucas[14] proposed that photoinduced effects such as photodarkening or photoexpansion are "seen as a dynamic sum of local excitations or defect creations." He proposed two mechanisms: bond twisting and generation of charge defects called valence alternation pairs. One would be a phonon-mediated mechanism, the other due to migration of electronic excitation, which is the mechanism we favor here.

In conclusion, our interpretation is that mobile clusters break and remake bonds without net change in bonding over an activation barrier of $\approx 4.25\ k_B T_g$ (Fig. 4.4(a)). Immobile clusters are either too large to hop on our time scale, or their hopping is not thermoneutral. The spatial heterogeneity we note here (some clusters hop fast, others slowly, many not at all) has also been noted for metallic glasses[6] and near T_g for an organic glass probed in different local environments by Kaufman and coworkers.[31] Photoexcitation does not heat the sample sufficiently to increase the hopping rate by much, but it does produce carriers that migrate to cluster surfaces and activate bonds. Although 532 nm excitation (2.33 eV) is hardly sufficient to make up the energy of a Si–Si bond or a switch from C–C/Si–C to Si–Si, it is possible that several long-lived excitations (>ms lifetime) are trapped at cluster surfaces. The local energy landscape of a cluster does not change instantly when laser intensity changes. The stress resulting from laser perturbation takes some time to settle after illumination is changed; the delay is caused by slow structural rearrangement of the matrix (other clusters) surrounding the cluster. These structural changes are too small to observe directly, but the mobile cluster's ratio of dwell times could be a sensitive local probe of surface relaxation subsequent to photoinduced stress.

4.6. Supplementary information

4.6.1. Sample composition

Cross-section Scanning Electron Microscopy was performed on a Philips XL30 ESEM-FEG with back scattered electron detection mode. Fig. 4.5(a) shows a typical SEM image of the a-SiC samples. The c-SiC which has higher density appears to be brighter than the lower density a-SiC. Film thickness is in the order of ~ 1.27 μm.

Angle-resolved X-ray Photoelectron Spectroscopy (XPS) measurements were done on a Kratos Axis ULTRA with an monochromatic Al source after STM imaging and thus reflect the oxidized samples. XPS for a-SiC and c-SiC samples were collected at 15° and 90°. Typical XPS spectra as show in Fig. 4.5(b). The surface compositions calculated from peak areas are shown in Table 4.1.

There were contaminations of Fe, Na, Zn, Ca on the c-SiC surface and most of them were cleaned after sputtering except Fe. The concentration of Fe remained unchanged and was less than 1.00 percent. We also observed less than 3.00 percent of Ar on sputtered samples.

The C concentration in the 15° angle of incidence measurements was overestimated because of the adsorbed hydrocarbons from atmosphere and oil from turbo pump. Thus we use the 90° measurements to calculate C-Si ratio for the a-SiC films. The C-Si ratio is ~ 0.58:0.42, with richer C on the surface as a result of preferential sputtering and in good agreement with G. Ecke *et. al.*.[17] The stoichiometry ratio is gradually recovered as we go deeper and deeper inside the samples. [17]

Scanning Tunneling Spectroscopy was measured using the constant-spacing mode. The voltage was ramped from -3 V to 3 V in 4000 steps while the tunneling current was measured. The constant-spacing STS usually overestimates the electronic bandgap, thus provides an upper limit for the optical gap of the surface. We performed STS measurements to check the laser alignment before making movies.

4.6.2. Optical characterization

Transmission measurements were done using Varian CARY 5G. A typical transmission curve for a-SiC samples is shown in Fig. 4.6 (black) with c-SiC (red). The a-SiC layer shows an

absorption of ~ 30% at 532 nm. We used that absorption factor of 0.3 to correct for the surface laser power density in our data analysis.

The saturation intensity to achieve n excitations among completely uncoupled chromophores can be estimated as follows. The excited state population change is given approximately by Einstein's relation $\partial x/\partial t = -B\rho x + B\rho\,(1-x) - x/\tau_r$, where τ_r is the excited state relaxation rate, B the Einstein coefficient, and ρ the density of the electromagnetic field at resonance. From this follows in steady-state ($\partial x/\partial t=0$) that $x=B\rho/(2B\rho+\tau_r^{-1})$, $x_{max}=1/2$ and $\rho=x/(B\tau_r(1-2x))$.[32] The saturation field density is defined when $x=x_{max}/2=1/4$, so $\rho_s=(2B\tau_r)^{-1}$ and in SI intensity units for a Gaussian profile, I_s (W/m^2) $= 2^{3/2}hc/(f^2\pi\tau_r\lambda^3)$ for the saturation intensity of a single excitation.[32] Here $f^2 I_s$ is the actual intensity in the sample, which includes a local tip-sample field enhancement factor (Baur). If $n>1$ independent excitations are required to stimulate a subsequent reaction, $p=x^n$ where x is the probability of an independent excitation, and the probability of all n occurring simultaneously is at most $p_{max}= (1/2)^n$. The cooperative saturation intensity occurs when $p = 1/2\ p_{max} = (1/2)^n/2$, and thus $x = (1/2)^{1/n}/2$. This requires a saturation radiation density relative to the single-excitation saturation radiation density of $\rho_{sc}/\rho_s= \{x/(B\tau_r(1-2x))\}/\{(2B\tau_r)^{-1}\} = 2x/(1-2x) = (2^{1/n}-1)^{-1}$. Thus for n≥1, I_{sc} (W/m^2) $= 2^{3/2}hc/((2^{1/n}-1)f^2\pi\tau_r\lambda^3)$.

Surface enhanced fields can vary over orders of magnitude in the vacuum of a tip-surface junction. For a silver tip 45 nm radius 1 nm above a silver surface, the field enhancement can exceed f=2000.[21] For a 50 nm tungsten sphere (our tip material) 1 nm above a metallic surface (our tunneling height), the enhancement inside the metallic surface is only 4,[21] and it decreases to about 2 as the radius of curvature of the sphere decreases to 25 nm. Our SiC surface is not metallic, but we adapt 2-4 as an approximate range because Fig. 2 in the main text shows that the clusters have metallic character under illumination. The resulting saturation intensity calculated with a literature $\tau_r \approx 1$ ps (see main text) and f=2-4 is 420-1700 mW/mm^2. Given the uncertainties in the input parameters reported in the literature (τ_r and f), this is in reasonable agreement with the experimental fit 600-1000 mW/mm^2 for the n=1 and n=4 models in Fig. 4b.

4.6.3. Cluster analysis

Cluster size was analyzed using procedure in ref. 33. Only clear clusters were analyzed in order to reduce error. We used the size of the SiC tetrahedron as the size of the GFU which is ~0.3086 nm.

To determine whether two segments of a single cluster time trace are consistent with the same underlying kinetics or not, we performed the Kolmogorov-Smirnov (K-S) test. The Kolmogorov-Smirnov test was performed by using the same procedure as in ref. 6. For each segment we simulated 1000 Markov traces, down-sampled to the STM scan rate and yielding the same length, average k_{obs} and R as the segment of the experimental trace. We then fed these two sets of 1000 traces each into the K-S test. The output of this test are two distributions of k_{obs} and R for the two segments, and a probability p that these two distributions are identical. The observed rate was calculated as $k_{obs}=<1/t_{-1}> + <1/t_1>$ and the dwell time ratio is given by $R=<t_{-1}>/<t_1>$ where t_{-1} and t_1 are the dwell times for the state "-1" and "1", respectively. k_{obs} was then converted to the barrier $\Delta G^{\dagger}$ using the relation $k_{obs}=k_0 exp(-\Delta G^{\dagger}/k_B T)$. The $k_B T$ unit was converted to $k_B T_g$ using room T = 295K and $T_g=2T_m/3$ where T_m is the melting temperature of SiC, 3003 K. The prefactor k_0 = 6x10^{10} s^{-1} was used based on a temperature-tuning study of metallic glass dynamics.[6]

In order to estimate the number of bonds between the surface of a cluster and the matrix, we generated a spherical cluster of 4H-SiC then counted the number of missing bonds of the surface atoms using coordination numbers of 4 for both Si and C. For a 4H-SiC cluster of ~ 5 GFU in diameter, there are ~ 10^2 missing bonds on the surface. That number of missing bonds was then divided by 2 to account for surface clusters and was used for amorphous SiC clusters.

4.6.4. Exciton diffusion and heat transfer

Exciton diffusion and heat transfer are described by the eqs. (4.1) and (4.2) in the main text. In the eq. (4.1), the depth-dependent power density $I(z)$ and power-dependent absorption coefficient $\alpha(I(z))$ were solved self-consistently as

$$\alpha(I(z)) = \alpha_0 \frac{I_s}{I(z)+I_s} \text{ and } I(z) = I_0 e^{-z\alpha(I(z))} \tag{4.4}$$

The last term in Eq. (4.1) gives the exciton generation rate and is plotted in Fig. 4.9 as a function of surface power density.

Eqs. (4.1) and (4.2) were solved numerically using backward time, central space finite difference method with boundary conditions described in the main text. A total depth of 3.66 μm was used in calculation including 2.4 μm of c-SiC substrate, 1.2 μm of a-SiC and 0.06 μm of vacuum. To describe the stepwise changes of the exciton diffusion coefficient D_{ex} (≈10^{-3} m^{2}s^{-1} in

c-SiC and a-SiC and 0 m^2s^{-1} in vacuum) and thermal conductivity k (330 $Wm^{-1}K^{-1}$ in c-SiC and a-SiC and assumed to be 0 $Wm^{-1}K^{-1}$ in vacuum), an error function with the width of 1.8 nm (≈ the size of an exciton) was used. Time step was 0.1 ps. The steady-state solutions with I_0=2240 mW/mm^2 (corresponding to ≈1120 mW/mm^2 at the a-SiC front surface) give an exciton density of $3.61x10^{-11}$ excitons/nm^3 and temperature increase of less than $5x10^{-4}$ K at the a-SiC surface. That small increase of temperature is in good agreement with the experimental data in Fig. 4.8. Laser powers f^2=16 times greater than the macroscopic incident flux, such as may be caused by tip enhancement of the field, still did not raise the calculated surface temperature by more than 1 K.

4.7. Figures and tables

Table 4.1: Surface compositions calculated from XPS.

Angle	a-SiC				c-SiC			
	Name	Position (eV)	Atomic conc. (%)	Std. dev. (%)	Name	Position (eV)	Atomic conc. (%)	Std. dev. (%)
15°	O 1s	529	30.42	1.18	O 1s	530	20.18	0.67
	C 1s	281	41.28	2.24	C 1s	283	55.40	1.87
	Si 2p	98	25.77	1.16	Si 2p	99	22.54	1.07
	Fe 2p	708	1.00	0.36	Fe 2p	712	0.66	0.34
	Ni 2p	843	0.33	0.19	Na 1s	1069	0.00	0.00
	Ar 2p	239	1.19	0.52	Zn 2p	1020	0.51	0.16
					Ca 2p	348	0.72	0.28
90°	O 1s	529	18.62	0.38	O 1s	530	12.11	0.24
	C 1s	281	45.00	0.83	C 1s	283	48.86	0.76
	Si 2p	98	33.09	0.39	Si 2p	99	37.13	0.41
	Fe 2p	708	0.61	0.11	Fe 2p	712	0.60	0.11
	Ni 2p	843	0.06	0.06	Na 1s	1069	0.25	0.09
	Ar 2p	239	2.61	0.19	Zn 2p	1020	0.22	0.07
					Ca 2p	348	0.83	0.10

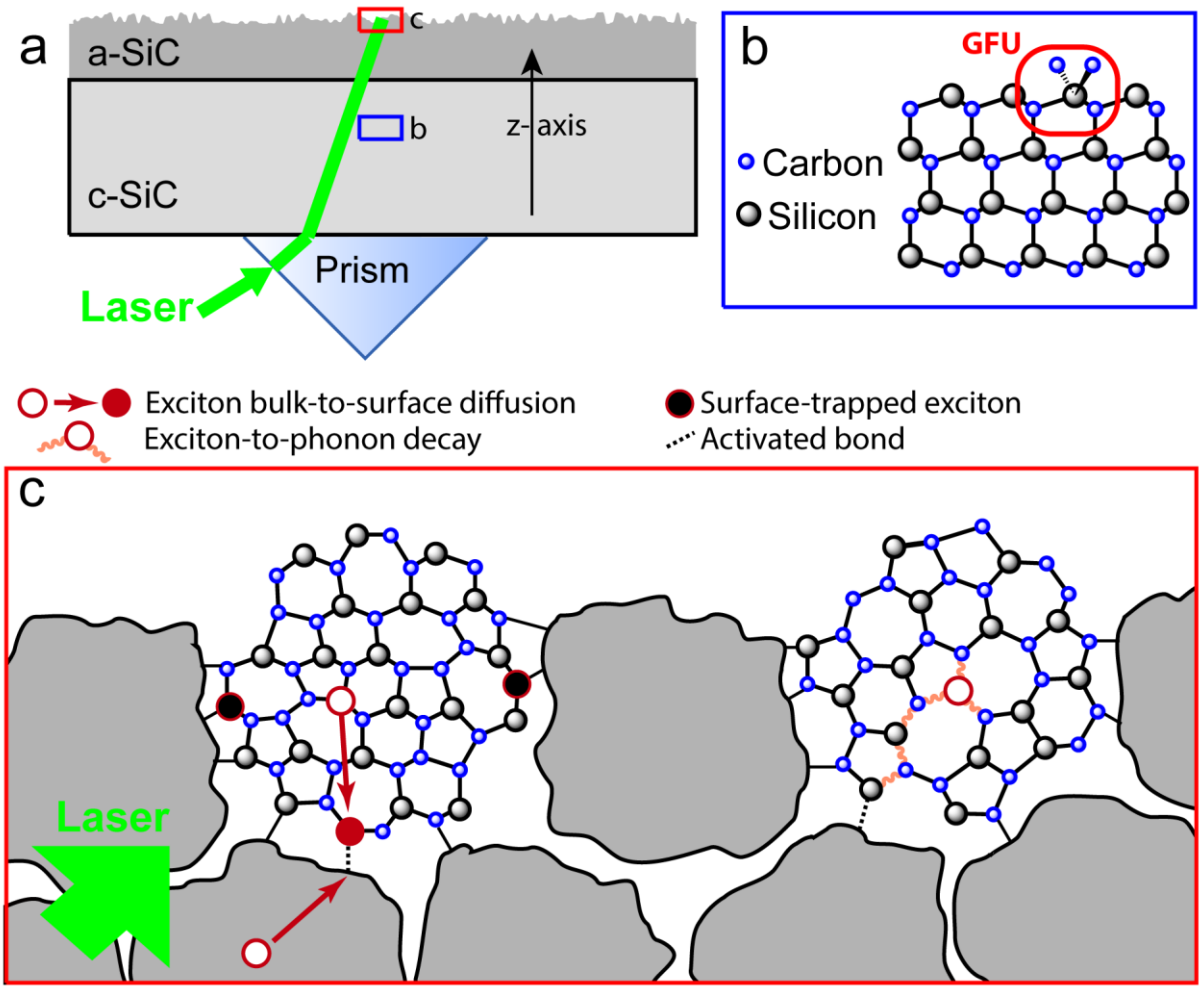

Figure 4.1: Schematic diagram for photoinduced glass surface dynamics. (a) Sample geometry: a-SiC = amorphous SiC; c-SiC = crystalline SiC. The prism allows the light to be total internally reflected. (b) Crystal structure of 4H-SiC. A GFU centered on a Si atom is outlined. (c) When the glass surface is photoexcited, initially excitons form (red open circles mark their center). In the electronic mechanism (left cluster), excitons from inside a cluster or a nearby cluster diffuse to the cluster surface, where they activate bonds. Cooperativity requires long-lived electronic surface-trapped states. In the vibrational mechanism (right), excitons relax to phonons. Their thermal diffusion to the cluster surface provides the energy to activate bonds. In both mechanisms, which are not mutually exclusive, no net bonds are formed or broken (thermoneutral), as we can only observe clusters with a dwell time ratio $R \approx 1$.

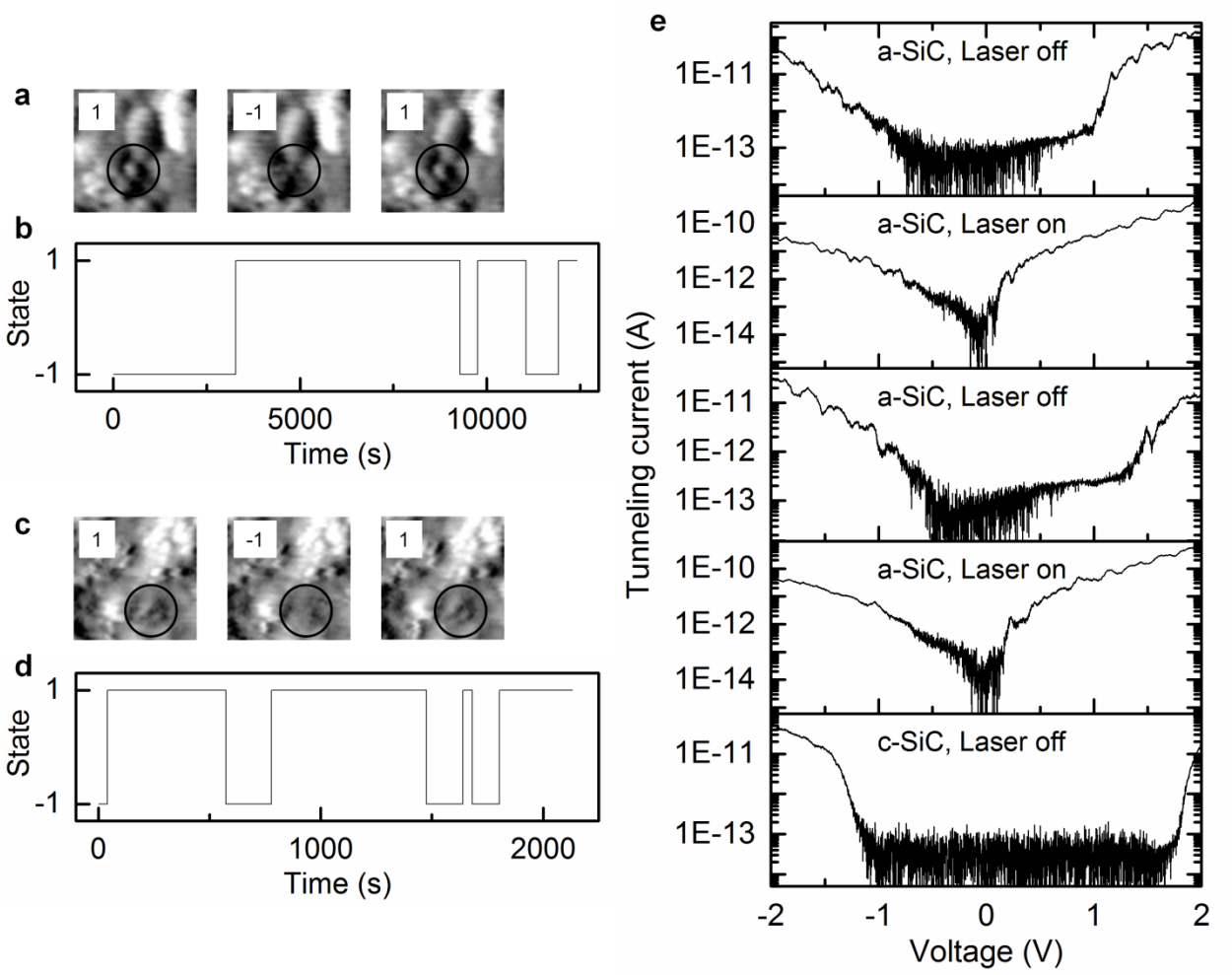

Figure 4.2: Two-state dynamics on a-SiC surface. (a) STM derivative images showing a two-state cluster (circled) without photoexcitation. Image size 6 nm × 6 nm. Scanning conditions: −2 V, 50 pA. (b) Time trace for the cluster in (a). (c) Derivative images showing a two-state cluster (circled) with laser illumination (481 mW/mm^2). Image size 6 nm × 6 nm. Scanning conditions: −2 V, 10 pA. (d) Time trace for the cluster in (c). (e) Series of STS showing reversible changes of the surface upon laser illumination. The STS shows semiconducting characteristics (~1.8 ± 0.3 eV) when the laser is off and metallic characteristics when the laser is on (393 mW/mm^2). The STS of the c-SiC substrate (bottom) shows a large bandgap (~2.8 ± 0.1 eV) which is transparent to the excitation wavelength (2.33 eV).

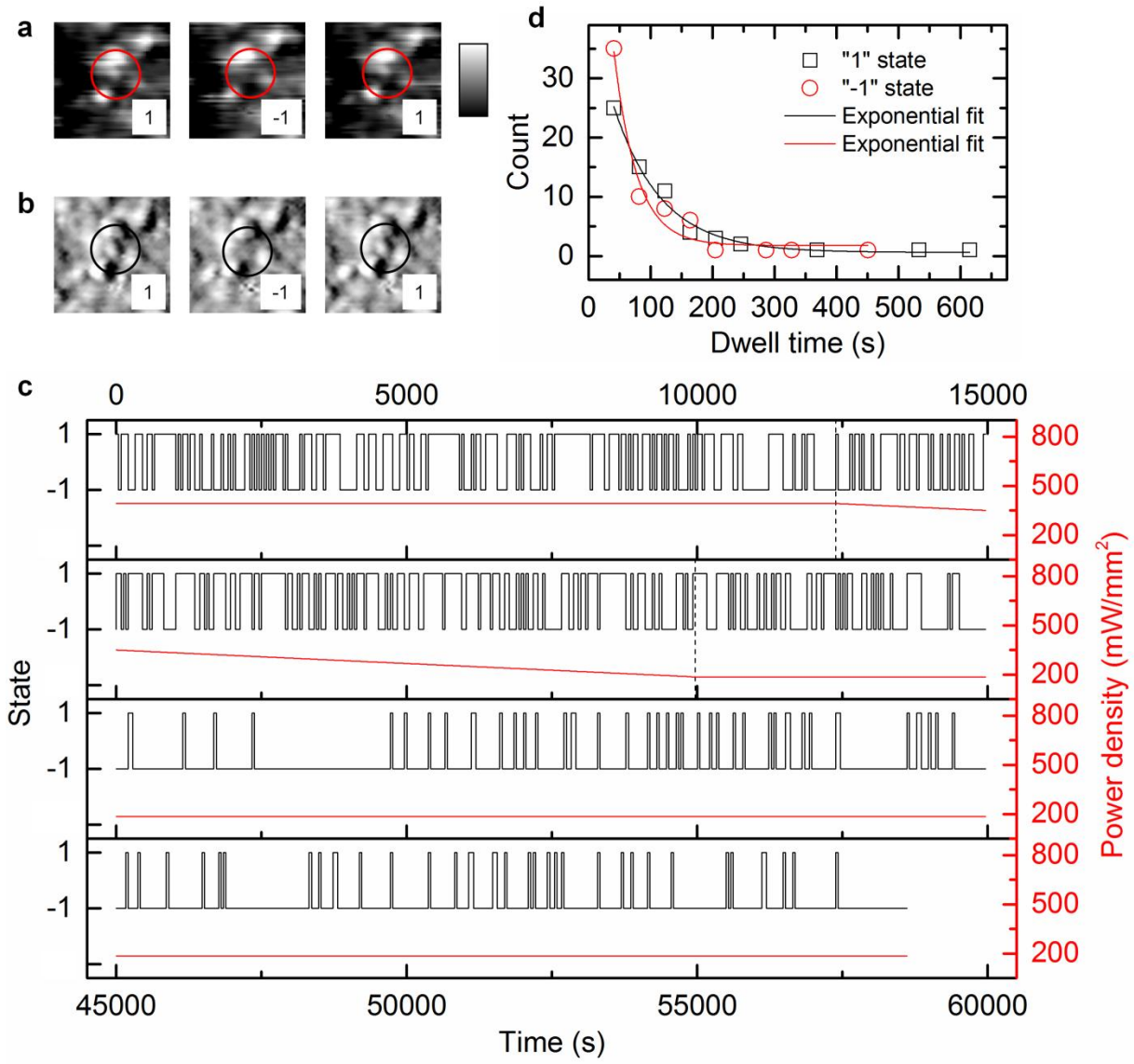

Figure 4.3: Power density-dependent dynamics. (a) Topographic images show a two-state cluster (circled). The full height scale ranges from 0 to 0.28 nm but is narrowed to highlight the hopping cluster. Grey color bar: 0.08-0.25 nm. Image size: 6 nm × 6 nm. Scanning conditions: −2 V, 10 pA. (b) The corresponding derivative images of the cluster in (a). Derivative movies before and after the power density ramp are given in the supplementary material.[15] (c) Laser power density-dependent two-state trace for the cluster in (a). The power density is 393 mW/mm^2 before and 186 mW/mm^2 after the ramp. The initial and final observed rates k_{obs} are similar, 0.02 s^{-1} and 0.02 s^{-1}, respectively. The dwell time ratio shifts from 1.23 to 5.32 and state "−1" is more favored after the ramp. (d) Dwell time distributions for state "1" (black) and "−1" (red) for the cluster in (c) before the ramp.

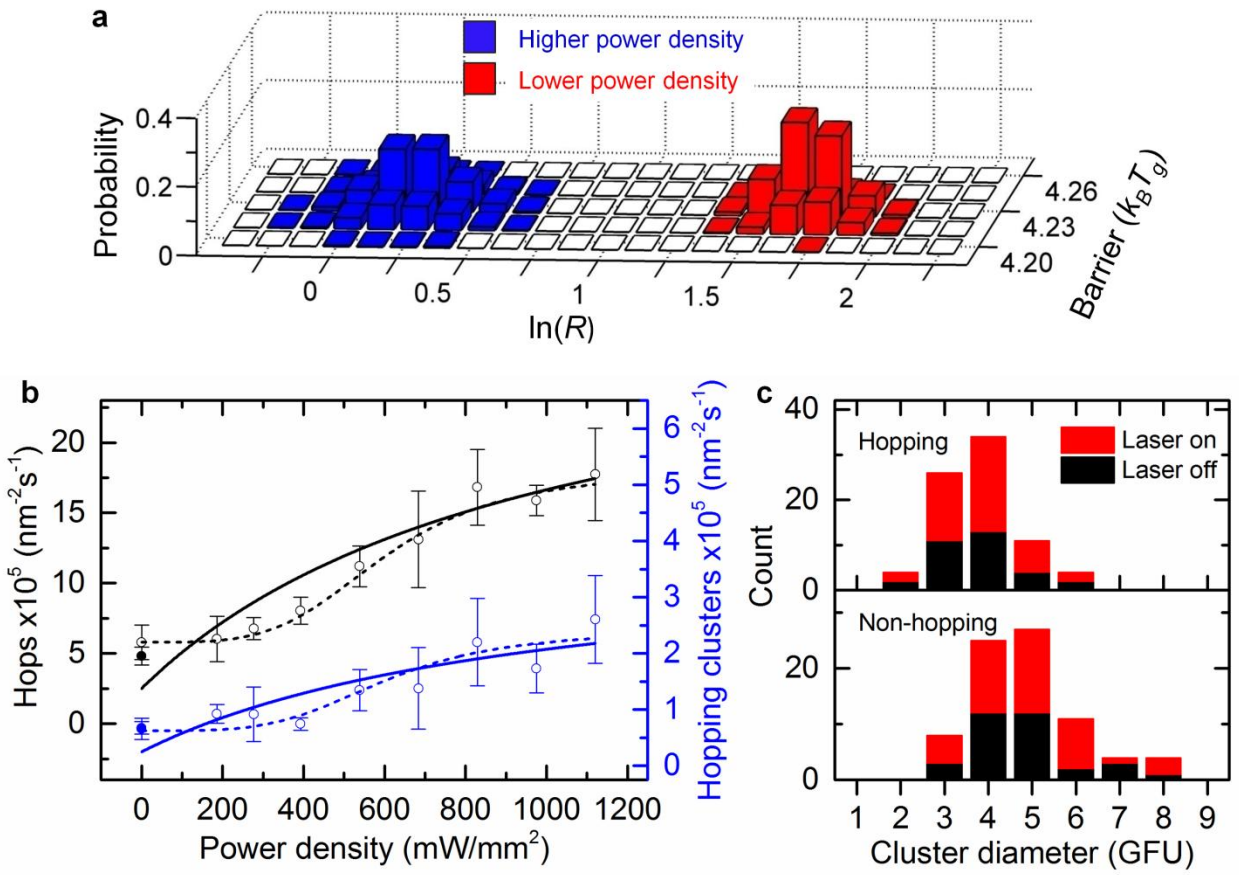

Figure 4.4: Kolmogorov-Smirnov test, average rate, and cluster size analysis. (a) shows two probability distributions of barrier height (~ln k_{obs}, see supplementary material) and ln$R$ for the beginning and ending parts of the trace in Fig. 4.3(c) before (blue) and after (red) the ramp. The two distributions are well separated and the probability that they are identical is extremely small $p < 10^{-10}$. (b) Average rate as a function of the laser power density at 10 pA tunneling current (open, black). The rate imaged at 50 pA (filled black) showing negligible effects of tunneling current on the dynamics. Upon laser illumination, the average rate increases by a factor of 3. The number of clusters that hop at least twice per unit time per unit area is shown in open blue (10 pA) and filled blue (50 pA). The curves are the fit to Eq. (4.3) with coefficient n = 1, I_s = 1000 mW/mm^2 (solid) and n = 4, I_s = 600 mW/mm^2 (dashed). (c) Cluster size distributions. The average sizes for hopping and non-hopping clusters are 3.77 ± 0.87 and 4.89 ± 1.21 GFU, respectively. The non-hopping clusters are slightly larger, in good agreement with theory and previous study.

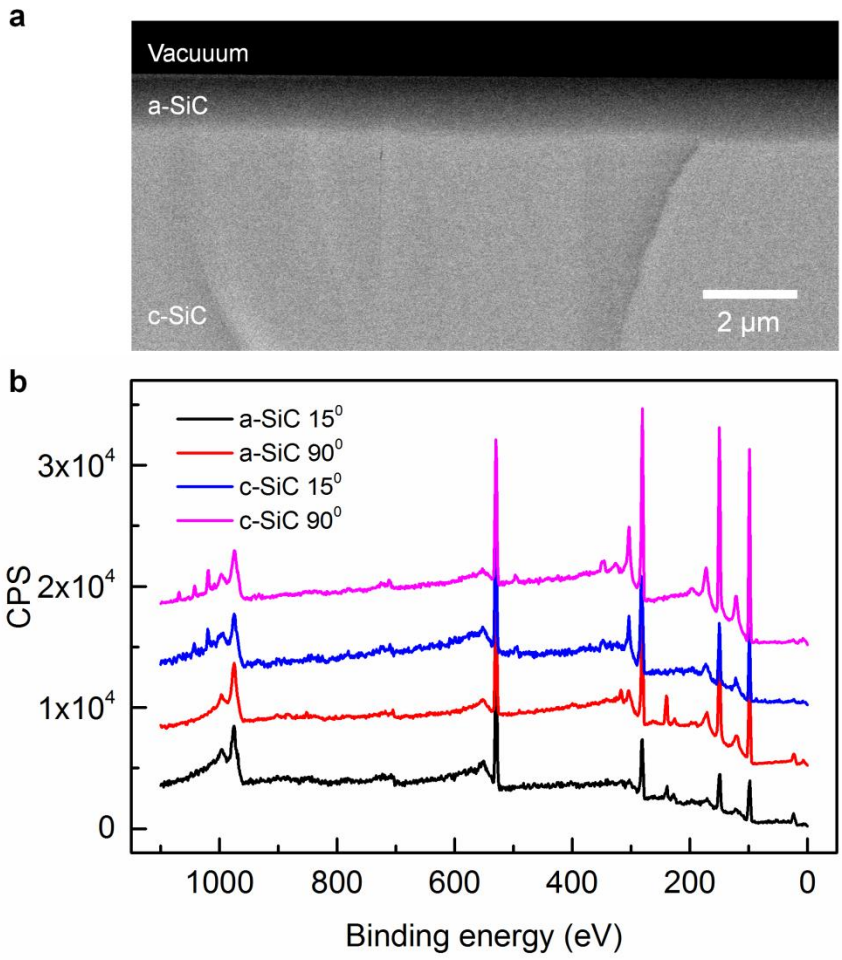

Figure 4.5: Sample characterizations. (a) A typical cross-section SEM image of a-SiC sputtered films on c-SiC substrate. Film thickness is in the order of ~ 1.27 µm. (b) Angle-resolved XPS for a-SiC films at 15° and 90°. XPS for c-SiC is shown for reference.

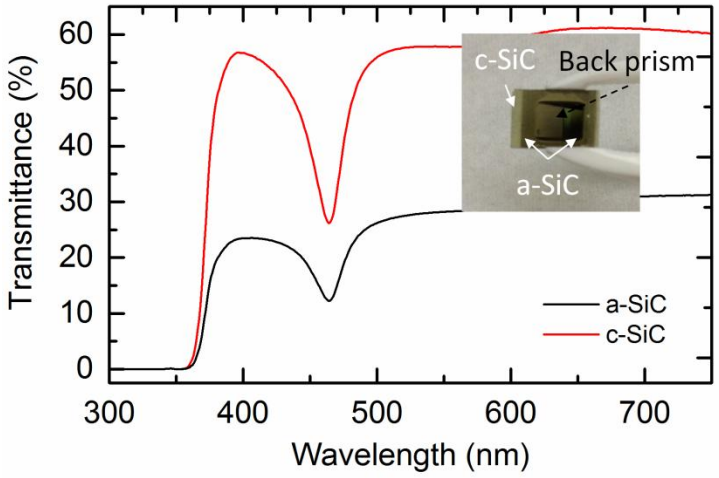

Figure 4.6: A typical transmission measurement of the a-SiC samples. The a-SiC layer shows an absorption of ~ 30%. Inset is an image of a typical sample. For UV-vis measurements, samples without prism were used.

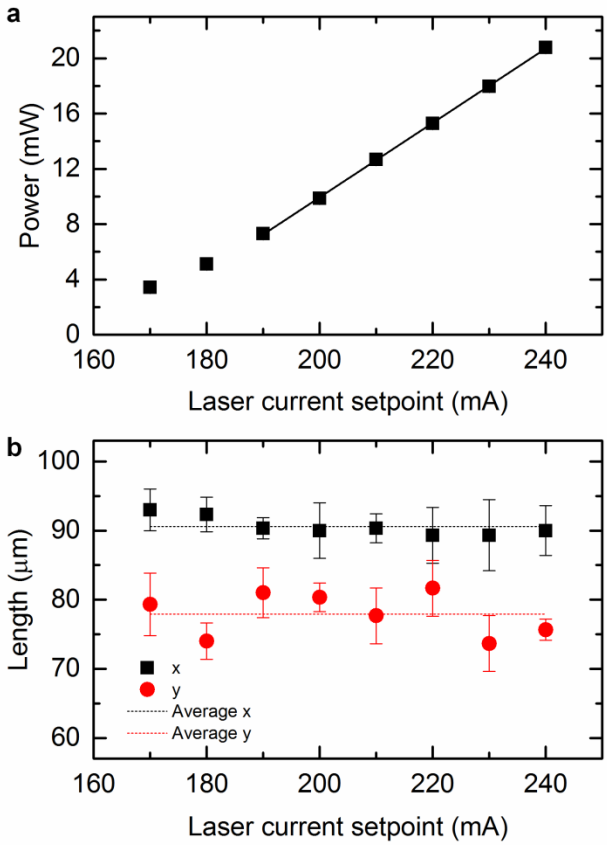

Figure 4.7: Laser calibration. (a) Power as a function of laser current setpoint (LCS). The dependence is linear above 190 mA. For the LCS smaller than 190 mA, the average values were used. (b) Laser beam size as a function of LCS. The average beam size is used for all LCS values in calculation of power density.

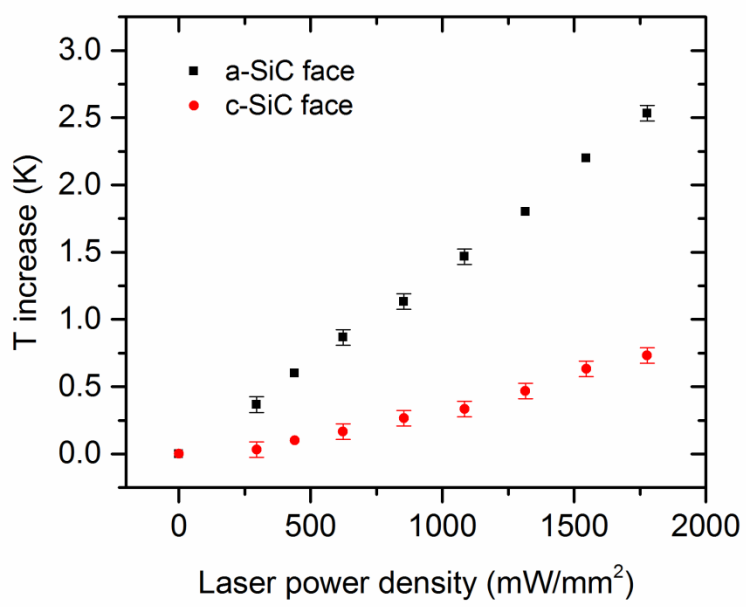

Figure 4.8: Temperature increase at the a-SiC (black) and c-SiC (red) faces as a function of laser power density. The measurements were done ex-situ on samples without prism. The temperature increase is small (< 3^o) ruling out the heating mechanism. The small increase in temperature is consistent with our previous study as we were only able to ramp the temperature up by 3° while maintaining the scanning.[6] Larger ramp resulted in the tip crash with the surface because the z range was reached to the maximum value.

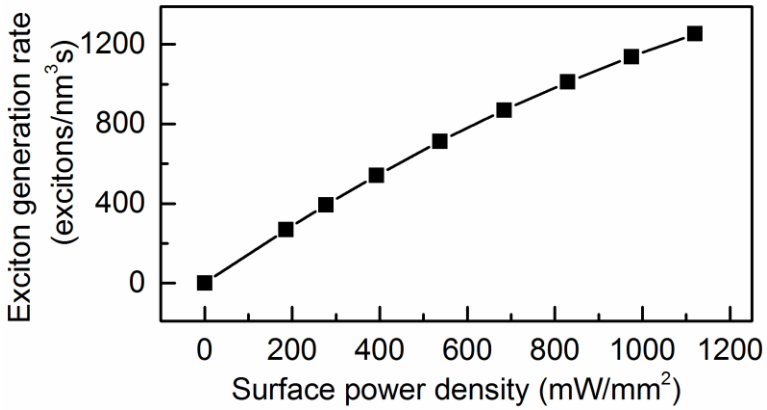

Figure 4.9: Calculated exciton generation rate at the a-SiC surface as a function of power density.

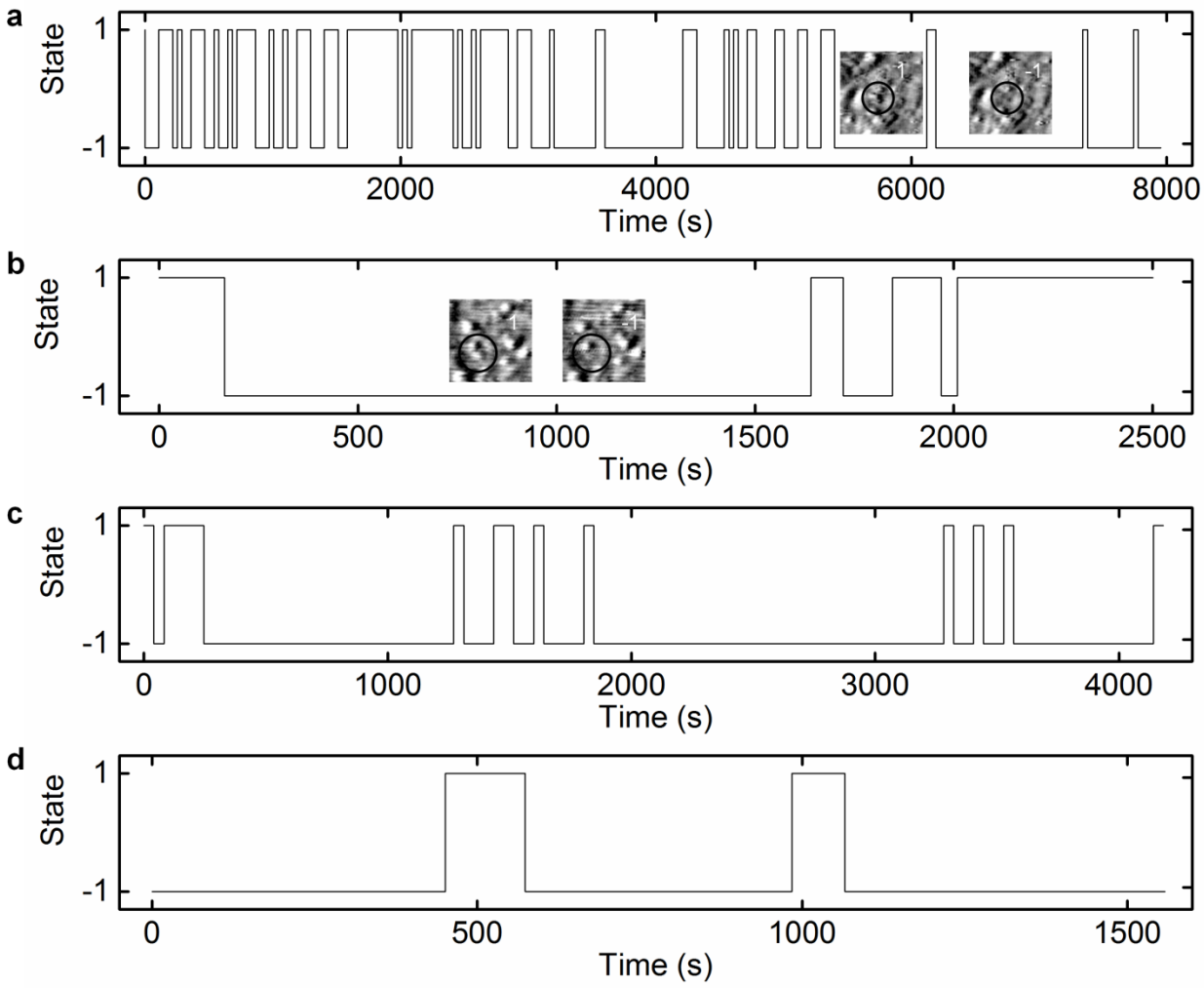

Figure 4.10: More examples of two-state traces with and without laser illumination. (a) Without laser illumination. Inset: two STM images show state "1" and "-1". Scanning conditions: -2 V, 10 pA. STM images size 8 nm x 8 nm. (b) 393 mW/mm^2. Inset: STM images showing the cluster in state "-1" and "1". Scanning conditions: 10 pA, -2 V. STM images 8 nm x 8 nm. (c) 684 mW/mm^2. Scanning conditions: 10 pA, -2 V. (d) 830 mW/mm^2. Scanning conditions: 10 pA, -2 V.

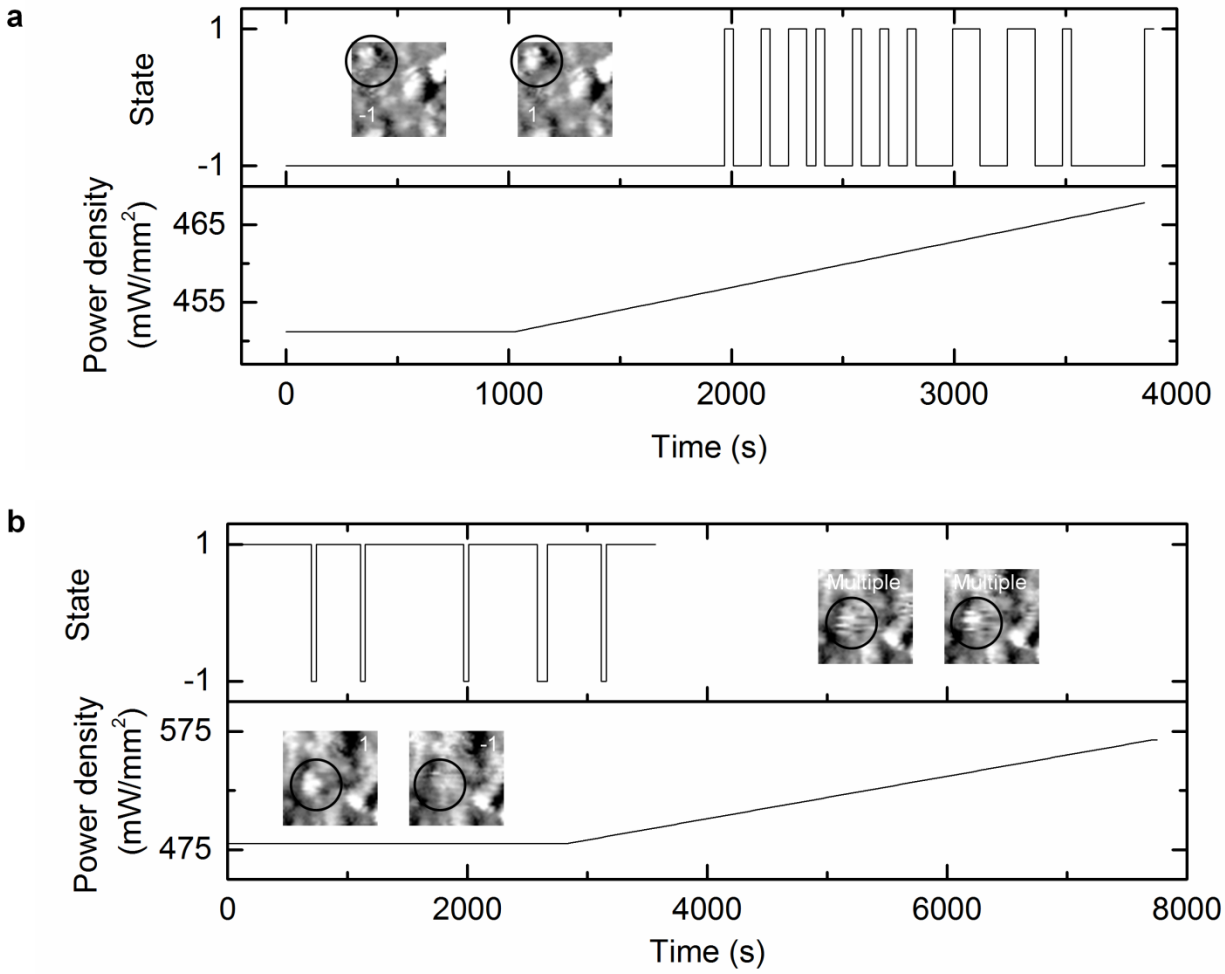

Figure 4.11: More examples of laser power density-dependent two-state traces. (a) A cluster start hopping after the power density is increased. Inset: STM images of the cluster. Scanning conditions: -2 V, 10 pA. STM images 6 nm x 6 nm. (b) A cluster that becomes super fast after ramping laser power density until the end of the movie. The superfast dynamics cannot be plotted after the time the cluster becomes superfast at ~ 3800 s. Inset: STM images of the cluster before the ramp (left) showing complete hops between frames and after the ramp (right) showing multiple hops in one frame. Scanning conditions: -2 V, 10 pA. STM images 6 nm x 6 nm.

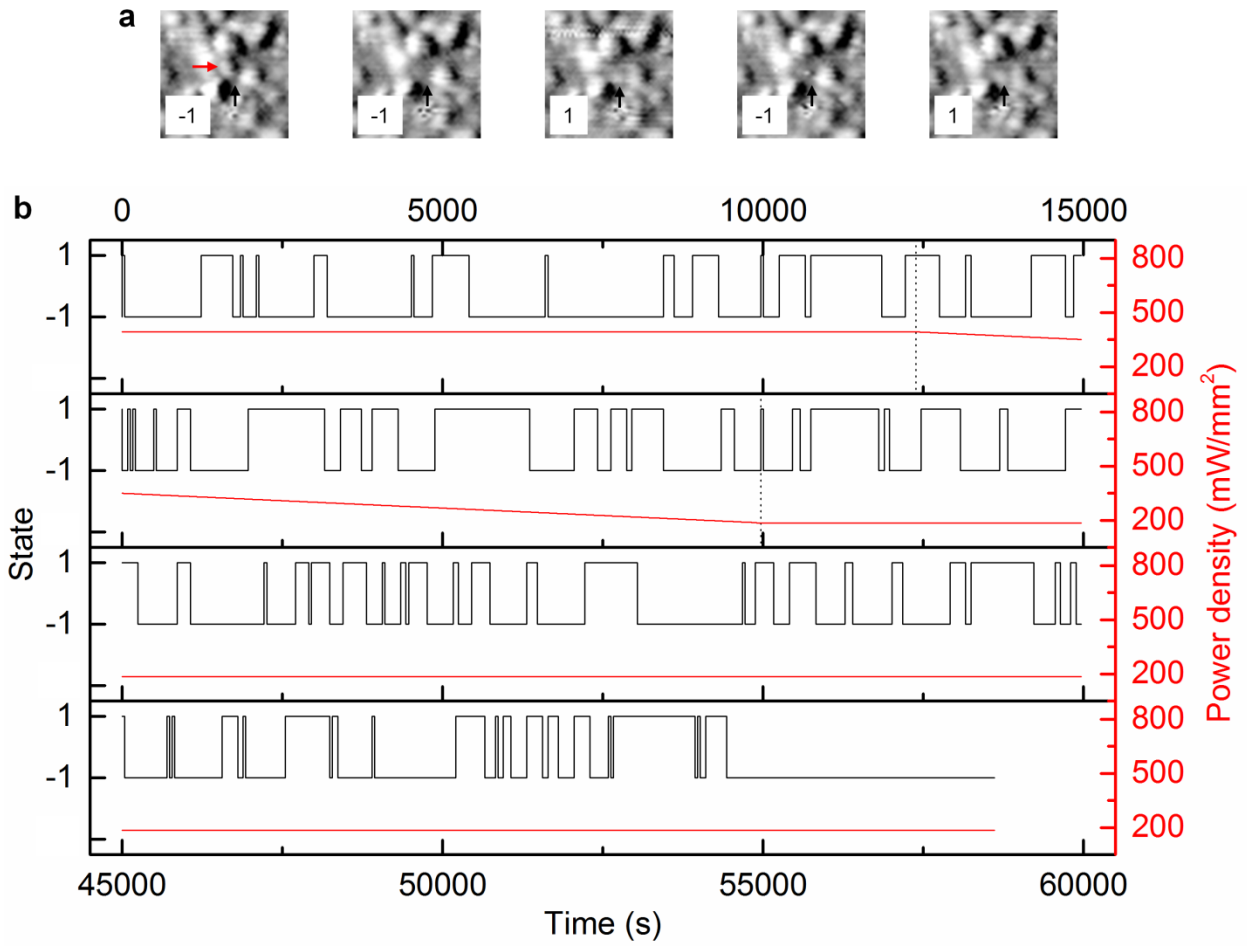

Figure 4.12: Another example of laser power density-dependent two-state traces. (a) STM images showing a cluster (black arrow) adjacent to the cluster in Fig. 4.3 (red arrow). Scanning conditions: -2 V, 10 pA. Image size: 6 nm x 6 nm. (b) The power density-dependent trace for the cluster in (a). To test whether the two clusters in Fig. 4.3 and Fig. 4.12 are correlated or not, we calculate the average state of the traces. The average states for the traces in Fig. 4.3(c), Fig. 4.12(b) and the product of these two traces are -0.33, -0.25 and 0.08, respectively. Thus the motion of the two adjacent clusters is uncorrelated.

4.8. Movies

Movie 4.3b_1 caption: A movie consisting of 100 frames for the cluster in Fig. 4.3(a-b) before the ramp. Scanning conditions: -2 V, 10 pA. Frame size 12.5 nm x 12.5 nm. STM imaging rate 41 s/frame. Playback rate 1 frame/s. The cluster favors both state "-1" and "1". In some frames, the cluster is caught in transition. For those frames, we assigned its state based on the former state. If the former state is "-1" then the state is "1" and reversely.

Movie 4.3b_2 caption: A movie consisting of 100 frames for the cluster in Fig. 4.3(a-b) after the ramp. Scanning conditions: -2 V, 10 pA. Frame size 12.5 nm x 12.5 nm. STM imaging rate 41 s/frame. Playback rate 1 frame/s. The cluster heavily shifts to favor state "-1" after the ramp.

4.9. References

1. P. G. Debenedetti and F. H. Stillinger, Nature 410, 259 (2001).
2. A. S. Keys, J. P. Garrahan, and D. Chandler, Proc. Natl. Acad. Sci. U. S. A. 110(12), 4482 (2013).
3. V. Lubchenko and P. G. Wolynes, Annu. Rev. Phys. Chem. 58, 235 (2007).
4. J. D. Stevenson, J. Schmalian, and P. G. Wolynes, Nat. Phys. 2, 268 (2006).
5. J. D. Stevenson and P. G. Wolynes, J. Chem. Phys. 129, 234514 (2008).
6. S. Ashtekar, J. Lyding, and M. Gruebele, Phys. Rev. Lett. 109, 166103 (2012).
7. J. A. J. Burgess, C. M. B. Holt, E. J. Luber, D. C. Fortin, G. Popowich, B. Zahiri, P. Concepcion, D. Mitlin, and M. R. Freeman, e-print arXiv:1409.5111 (2014).
8. D. Nguyen, J.Mallek, A. N. Cloud, J. R. Abelson, G. S. Girolami, J. Lyding, and M. Gruebele, J. Chem. Phys. 141, 204501 (2014).
9. L. A. G. Gray and C. B. Roth, Soft Matter 10, 1572 (2014).
10. A. Wisitsorasak and P. G. Wolynes, Proc. Natl. Acad. Sci. U. S. A. 109, 16068 (2012).
11. A. Kozdras, R. Golovchak, O. Shpotyuk, S. Szymura, A. Saiter, and J.-M. Saiter, J. Mater. Res. 26, 2420 (2011).
12. J. P. Larmagnac, J. Grenet, and P. Michon, Philos. Mag. B 45, 627 (1982).
13. V. I.Mikla, I. P.Mikhalko, andV.V.Mikla, Mater. Sci. Eng.:B83, 74 (2001).
14. P. Lucas, J. Phys.: Condens. Matter 18, 5629 (2006).
15. See supplementary material at http://dx.doi.org/10.1063/1.4922695 for sample characterizations, data analysis methods, and more examples of cluster dynamics.

16. T. Lundstrom, W. Schoenfeld, H. Lee, and P. M. Petroff, Science 286, 2312 (1999).
17. J. Pezoldt, B. Stottko, G. Kupris, and G. Ecke, Mater. Sci. Eng.: B 29, 94 (1995).
18. P. J. P. Gérault, R.Morancho, and G. Constant, Philos. Mag. B 49, 11 (1984).
19. J. Bullot and M. P. Schmidt, Phys. Status Solidi B 143, 345 (1987).
20. J. W. Lyding, S. Skala, J. S. Hubacek, R. Brockenbrough, and G. Gammie, Rev. Sci. Instrum. 59, 1897 (1988).
21. "Plasmon-induced tunneling currents: The influence of tip modes," Photons and Local Probes, edited by C. Baur, A. Rettenberger, K. Dransfeld, P. Leiderer, B. Koslowski, R.Möller, and P. Johansson (Springer, Netherlands, 1995), Vol. 300.
22. R. Corkish, D. S. P. Chan, and M. A. Green, J. Appl. Phys. 79, 195 (1996).
23. S. S. YasuakiMasumoto, H.Munekata, and H. Kukimoto, J. Phys. Soc. Jpn. 52, 3985 (1983).
24. I. P. Blackwood, K. S. Teng, T. G. G. Maffeïs, J. R. Franks, and S. P. Wilks, J. Appl. Phys. 98, 103528 (2005).
25. J. A. Peacock, Mon. Not. R. Astron. Soc. 202, 615 (1983).
26. S. F. Swallen, K. L. Kearns, M. K. Mapes, Y. S. Kim, R. J. McMahon, M. D. Ediger, T. Wu, L. Yu, and S. Satija, Science 315, 353 (2007).
27. S. Ashtekar, D. Nguyen, K. Zhao, J. Lyding,W. H.Wang, andM. Gruebele, J. Chem. Phys. 137, 141101 (2012).
28. G. L. Zhao and D. Bagayoko, New J. Phys. 2, 16 (2000).
29. P. Lucas, A. Doraiswamy, and E. A. King, J. Non-Cryst. Solids 332(1–3), 35 (2003).
30. H. Hisakuni and K. Tanaka, Science 270, 974 (1995).
31. L. M. Leone and L. J. Kaufman, J. Chem. Phys. 138, 12A524 (2013).
32. W. Demtröder, Laser Spectoscopy, 2nd edition. (Springer, Berlin, 1996).
33. S. Ashtekar, G. Scott, J. Lyding, and M. Gruebele, J. Phys. Chem. Lett. 1, 1941 (2010).

Part II: Single-Molecule Absorption of Quantum Dots

5. Introduction to single-molecule absorption detected by scanning tunneling microscopy of quantum dots

Absorption spectroscopy is a universal technique as all molecules absorb light. By doing absorption spectroscopy at the single-molecule level, richer information can be obtained owing to the absence of averaging. Single-molecule absorption (SMA) is challenging because of the diffraction limiting the resolution to one half of the probe wavelength.[1] In addition, conventional detection by reduced light throughput is difficult and has been achieved only in a few cases.[2] Multiple strategies have been developed to overcome the diffraction including multicolor imaging[3,4] and near-field techniques. Resolution of tens of nanometers has been achieved.[5]

In our group, we use scanning tunneling microscopy (STM) with ultrahigh spatial resolution as the detector to study SMA,[6-8] thus overcoming the diffraction limit. SMA-STM is capable of resolving optical absorption at sub-nm resolution. Examples of optically distinguishing adjacent, similar-shape carbon nanotubes (CNTs) and intramolecular defects[8] have been previously shown by our group. By tuning the electric field, optical properties of CNTs can also be tuned.[9] We apply SMA-STM to investigate SMA spectroscopy of quantum dots (QDs) and intermolecular energy transfer between single QDs and CNTs. These processes are important for applications of QDs in biological imaging, solar cells and photocatalysis.[10-12]

5.1. SMA-STM setup

In a SMA-STM experiment, molecules of interest (QDs) are deposited on a clean, atomically flat, transparent and conducting or semiconducting substrate surface (Fig. 5.1). We use ultrathin conducting PtAu on sapphire,[13] semiconducting crystalline silicon carbide (c-SiC) and amorphous silicon carbide (a-SiC) substrates in our experiments (Fig. 5.2). We have also used c-Si in the past, for molecules or nanostructures with near-IR absorption.[6-8] The substrate is either machined into a -15^{o} wedge (c-SiC and a-SiC) or a prism is attached at the backside in order to obtain total internal reflection (PtAu). Amplitude-modulated light at 2.2 kHz is irradiated from the back of the substrate, with total internal reflection to reduce tip heating effects. In our experiment, we use single wavelengths at 532 or 660 nm to excite the QDs. If the QD absorbs light, the corresponding modulated absorption signal is detected using a lock-in

amplifier (LIA) and STM (Fig. 5.2). We collect both in phase and 90^o out of phase SMA signals. If there is an acceptor close to the QD, for example, a bigger QD or a CNT, energy transfer can happen. We detect energy transfer as a reduction in absorption of the donor (smaller QD) or as an increase in absorption of the acceptor (bigger QD or CNT).

What do we truly detect using SMA-STM? In the simplest scenario, when the laser is off, the QD is at the ground state, for example, with S-like orbital or electron density (Fig. 5.3). When the laser is on with intensity equal to or greater than the saturation intensity, the electron density is the average of the ground state and the excited state. For example, the excited state has a P-like electron density, as shown in Fig. 5.3. The laser is then off, on, off and so on. The modulation of electron density leads to a modulation in the tunneling current and the amplitude and phase of this modulation is detected by STM and LIA. Thus we approximately detect electron density difference between the excited state and the ground state, offset by background electron density change (if there is).[14]

5.2. Quantum dots

QDs or semiconductor nanocrystals with diameter ranging from ~ 1 to tens of nanometers have many interesting properties because of the quantum confinement.[15] For example, the absorption and fluorescence of QDs can be tuned continuously by changing the size of the QDs. Smaller QDs have a higher bandgap, and thus start absorbing light and fluorescing at higher energy.

The quantum confinement arises in QDs when the radius of the QDs is smaller than the Bohr radius of the bulk exciton, which is given by:[16,17]

$$a_{B,ex} = \frac{\hbar^2 \varepsilon}{e^2}\left(\frac{1}{m_e^*} + \frac{1}{m_h^*}\right) = \frac{\hbar^2 \varepsilon}{\mu e^2} = a_{B,H}\left(\frac{m_e}{\mu}\right)\varepsilon \tag{5.1}$$

where $\hbar$ is the reduced Planck constant, e is the charge of the electron, ε is the dielectric constant of the material, m_e^* is the effective mass of the electron in QD, m_h^* is the effective mass of the hole in QD, $\mu = \frac{m_e^* m_h^*}{m_e^* + m_h^*}$ is the reduced mass of the exciton, $a_{B,H}$ is the Bohr radius of hydrogen atom, m_e is the mass of free electron. As a result, the exciton is confined in three

dimensions. The confinement of excitons due to electron-hole attraction is described by a hydrogenic Hamiltonian with the hole of the exciton playing the role of the atomic nucleus:[18,19]

$$\hat{H} = -\frac{\hbar^2}{2m_h^*}\nabla_h^2 - \frac{\hbar^2}{2m_e^*}\nabla_e^2 - \frac{e^2}{\varepsilon \mid r_e - r_h \mid} \tag{5.2}$$

where $\mid r_e - r_h \mid$ is the electron hole separation.

The quantum confined energy of the exciton in QDs is given by a particle in a box energy levels:[18]

$$E_n = \frac{\hbar^2 \pi^2 n^2}{2\mu R^2} \tag{5.3}$$

where R is the QD radius. The lowest excited state energy or the bandgap of QDs is given by:[16-18]

$$E_{g,QD} = E_{g,bulk} + \frac{\hbar^2 \pi^2}{2\mu R^2} - \frac{1.8e^2}{\varepsilon R} \tag{5.4}$$

The first term in Eq.5.4 is the bulk bandgap, the second term is the confinement energy from Eq. 5.3 and the third term is Coulomb interaction between the electron and hole in the exciton from Eq. 5.2. The energy for higher excited states is obtained in a similar way, taking into account higher value of n and Coulomb interaction of higher excited states. Thus, near the band edges, QDs have discrete energy levels resemble to atoms and are usually called artificial atoms. The bandgap of QDs is highly tunable, simply by varying the QD radius R (Eq. 5.4).

QDs in SMA-STM experiments are subject to a very electric field (on the order of ~ 1 V/nm). The resulting quadratic Stark effect on QDs has been well characterized.[20] QDs are highly polarizable with polarizability comparable to the physical volume of the QDs.[20] The quadratic Stark effect is important in our experiments, and is utilized to tune the QD absorption between different transitions, in addition to tuning laser wavelength. QDs are deposited onto clean surfaces using matrix-assisted dry contact transfer.[14]

5.3. Energy and electron transfer mechanisms

In clusters and films of QDs, there is a distribution of bandgaps because of size and shape heterogeneity and defects. As a result, energy and/or electrons can be transferred to the QDs with smaller bandgap. Depending on the interaction and separation between the QDs, different transfer mechanisms may apply in different cases.

5.3.1. Förster resonance energy transfer

Förster Resonance Energy Transfer (FRET) is an incoherent nonradiative energy transfer mechanism resulting from dipolar (Coulombic) interactions.[21] In FRET, the excited state of the donor couples resonantly with the absorbing transition of the ground state of the acceptor, and energy is transferred to the acceptor as the donor relaxes. Fig. 5.4a shows the FRET mechanism. FRET rate is given by:[21,22]

$$k_{FRET} = \frac{9000(\ln 10)\kappa^2 \phi_D J}{128\pi^5 N_A n^4 \tau_D R^6} = \left(\frac{1}{\tau_D}\right)\left(\frac{R_0}{R}\right)^6 \tag{5.5}$$

where ϕ_D is the quantum yield of the donor, τ_D is the fluorescence lifetime of the donor, n is the refractive index of the medium, N_A is the Avogadro number, R is the separation between the donor and the acceptor. κ is the orientation factor which can range from 0 to 4 and the average over all possible orientation is 2/3. R_0 is the Forster radius in which FRET efficiency is 50%:

$$R_0 = \left(\frac{9000(\ln 10)\kappa^2 \phi_D J}{128\pi^5 N_A n^4}\right)^{1/6} \tag{5.6}$$

J is the spectral overlap between the donor emission and the acceptor absorption spectra. The spectral overlap J is given by:[22]

$$J = \frac{\int F_D(\nu)\varepsilon_A(\nu)\nu^{-4} d\nu}{\int F_D(\nu) d\nu} = \int F_{D,norm}(\nu)\varepsilon_A(\nu)\nu^{-4} d\nu \tag{5.7}$$

where $F_D(\nu)$ ($F_{D,norm}(\nu)$) is the fluorescence spectrum (normalized fluorescence spectrum) of the donor and $\varepsilon_A(\nu)$ is the molar extinction coefficient of the acceptor. The FRET efficiency is defined as:[22]

$$E_{FRET} = \frac{k_{FRET}}{k_{FRET} + k_D + \sum_i k_i} \approx \frac{k_{FRET}}{k_{FRET} + k_D} = \frac{R_0^6}{(R_0^6 + R^6)} \tag{5.8}$$

where k_i denotes other relaxation processes and $k_D = 1/\tau_D$ is the fluorescence decay rate of the donor. Because of the R^{-6} dependence, FRET is a long-range energy transfer mechanism. The Forster radius is typically in the range of few nanometers.[22]

5.3.2. Dexter electron transfer

Dexter electron transfer is an electron transfer mechanism based on electron exchange interaction.[23] When the donor and the acceptor are in close proximity, so that their wavefunctions overlap, an electron from the excited state of the donor and another from the ground state of the acceptor can exchange.[23,24] The result is that, the donor relaxes to the ground state and the acceptor is excited. The schematic for Dexter electron transfer is shown in Fig 5.4b. The Dexter electron transfer rate is given by:[23-25]

$$k_{Dexter} = \frac{2\pi}{\hbar} K^2 e^{(-2R/L)} J \tag{5.9}$$

where K is a constant with unit of energy, L is the effective average Bohr radius, R is the separation between the donor and the acceptor. J is the normalized spectral overlap integral:

$$J = \int F_{D,norm}(\nu) A_{A,norm}(\nu) d\nu \tag{5.10}$$

where $F_{D,norm}(\nu)$ is the normalized donor fluorescence spectrum and $A_{A,norm}(\nu)$ is the normalized acceptor absorption spectrum. Because of the exponential dependence (Eq. 5.9) on the donor acceptor separation, Dexter electron transfer is a short-range transfer mechanism, typically within the range of 1 nm.[23-25]

5.3.3. Superexchange transfer mechanism

In the superexchange transfer mechanism, a bridge between the donor and the acceptor mediates the electron and/or hole exchange, resulting in the electron and/or hole transfer from the donor to the acceptor.[26-28] The schematics for the superexchange transfer mechanism is shown in Fig. 5.4c. The superexchange transfer rate also depends exponentially on the separation of the donor and the acceptor R and is given by:[26-28]

$$k_{Superexchange} = k_0 e^{-\beta R} \tag{5.11}$$

where β is the bridge attenuation factor and is in the order of 10 nm^{-1}.[27] Superexchange transfer is a short-range transfer mechanism. One can think of it as two-step Dexter transfer through a high energy bridge that may be populated only as a virtual state, in which case the process can be treated by second order perturbation theory of the coupling that is not too strong.

5.4. Figures

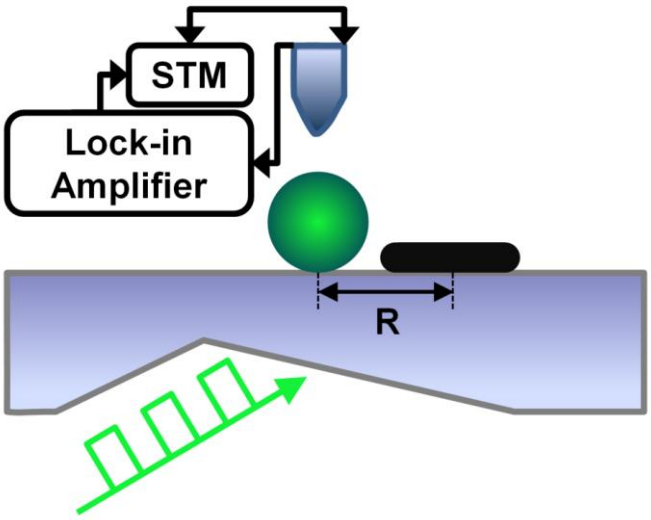

Figure 5.1: SMA-STM experiment setup. QDs and CNTs are deposited onto clean, atomically flat, transparent and conducting or semiconducting substrates. The molecules are excited with amplitude-modulated 532 nm light from the back with total internal reflection to reduce tip heating effects. Absorption is detected using STM and LIA.

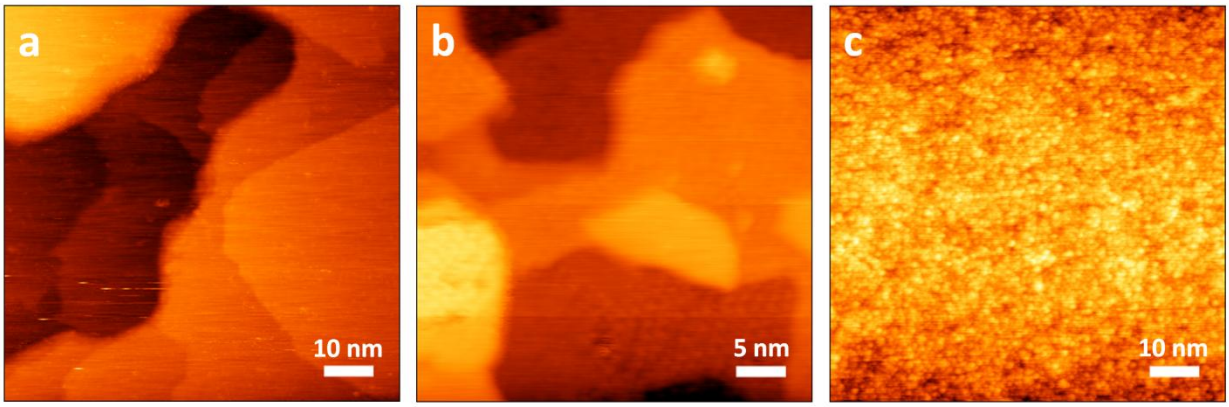

Figure 5.2: STM images of the substrates. (a) 15 nm PtAu on sapphire. (b) Crystalline silicon carbide and (c) amorphous silicon carbide.

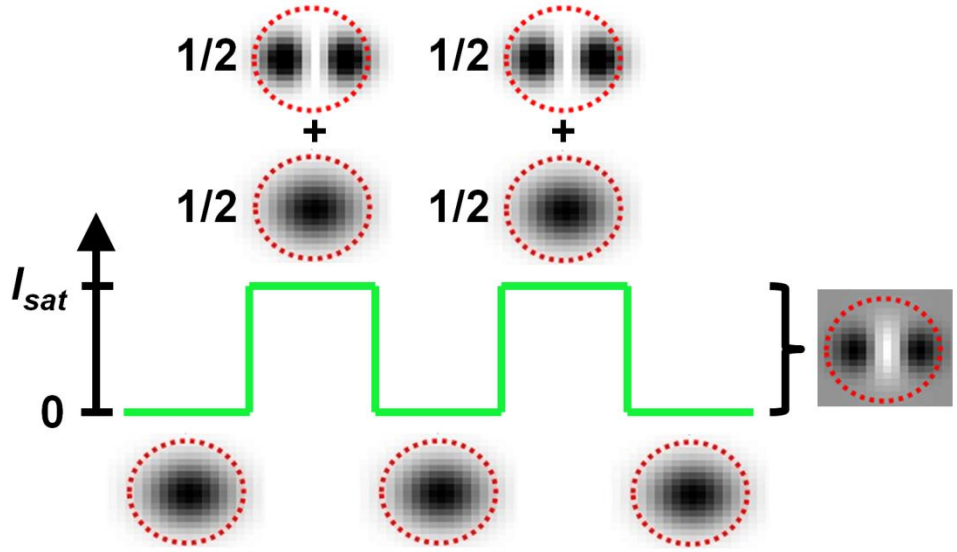

Figure 5.3: SMA signal detection. By cycling the QDs at 2.2 kHz between ground and excited states, SMA signal detected by STM is approximately equal to the electron density difference between the excited and the ground states.

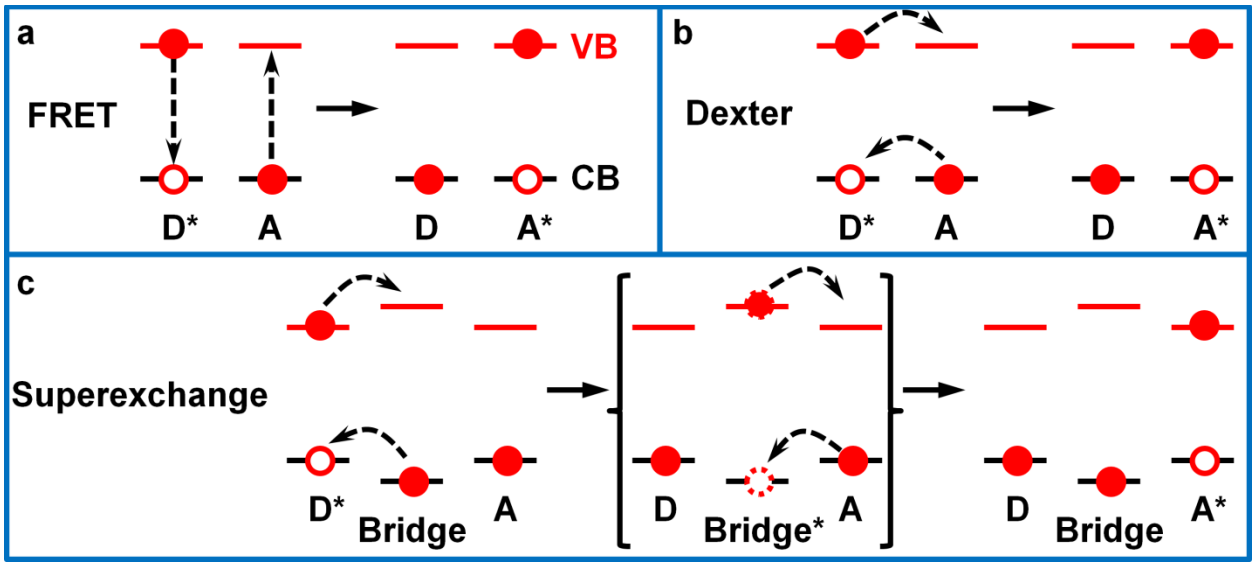

Figure 5.4: Schematics for energy and electron transfer mechanisms. (a) Förster Resonance Energy Transfer. (b) Dexter electron transfer and (c) Superexchange transfer.

5.5. References

1. E. Abbe, J. R. Microsc. Soc., 3, 790–812 (1883).
2. J.-C. Blancon, M. Paillet, H. N. Tran, X. T. Than, S. A. Guebrou, A. Ayari, A. San Miguel, N.-M. Phan, A.-A. Zahab, J.-L. Sauvajol, N. Del Fatti and F. Vallée, Nat. Commun., **4**, 2542 (2013).
3. S. T. Hess, T. P. K. Girirajan and M. D. Mason, Biophys. J., 91, 4258–72 (2006).
4. M. J. Rust, M. Bates and X. Zhuang, Nat. Methods, 3, 793–5 (2006).
5. D. W. Pohl and F. Rohner, J. Appl. Phys., 59, 3318 (1986).
6. J. Ballard, E. Carmichael, J. Lyding and M. Gruebele, Nano Lett., 6, 45–49 (2006).
7. E. Carmichael, J. Ballard, J. Lyding and M. Gruebele, J. Phys. Chem. C, 111, 3314 (2007).
8. G. Scott, S. Ashtekar, J. Lyding and M. Gruebele, Nano Lett., 10, 4897–4900 (2010).
9. L. Nienhaus, S. Wieghold, D. Nguyen, J. W. Lyding, G. E. Scott and M. Gruebele, ACS Nano, 9, 10563–70 (2015).
10. I. Gur, Science, 310, 462–465 (2005).
11. P. V Kamat, J. Phys. Chem. C, 112, 18737–18753 (2008).
12. X. Chen, L. Liu, P. Y. Yu and S. S. Mao, Science, 331, 746–750 (2011).
13. L. Nienhaus, G. E. Scott, R. T. Haasch, S. Wieghold, J. W. Lyding and M. Gruebele, J. Phys. Chem. C, 118, 13196–13202 (2014).
14. L. Nienhaus, J. J. Goings, D. Nguyen, S. Wieghold, J. W. Lyding, X. Li and M. Gruebele, J. Am. Chem. Soc., 137, 14743–50 (2015).
15. A. P. Alivisatos, Science, 271, 933–937 (1996).
16. A. L. Stroyuk, A. I. Kryukov, S. Y. Kuchmii and V. D. Pokhodenko, Theor. Exp. Chem., 41, 67–91 (2005).
17. T. Trindade, P. O'Brien and N. L. Pickett, Chem. Mater., 13, 3843–3858 (2001).
18. L. E. Brus, J. Chem. Phys., 80, 4403 (1984).
19. Y. Kayanuma, Phys. Rev. B, 38, 9797–9805 (1988).
20. S. A. Empedocles, Science, 278, 2114–2117 (1997).
21. T. Förster, Ann. der Phys., 2, 55–75 (1948).
22. D. C. Lamb, Single Particle Tracking and Single Molecule Energy Transfer, Wiley-VCH Verlag (2009).
23. D. L. Dexter, J. Chem. Phys., 21, 836 (1953).

24. M. Inokuti and F. Hirayama, J. Chem. Phys., 43, 1978 (1965).

25. C. B. Murphy, Y. Zhang, T. Troxler, V. Ferry, J. J. Martin and W. E. Jones, J. Phys. Chem. B, 108, 1537–1543 (2004).

26. H. M. McConnell, J. Chem. Phys., 35, 508 (1961).

27 . Y. A. Berlin, A. L. Burin and M. A. Ratner, J. Am. Chem. Soc., 123, 260–268 (2001).

28. N. Renaud, Y. A. Berlin, F. D. Lewis and M. A. Ratner, J. Am. Chem. Soc., 135, 3953–63 (2013).

6. Imaging energy transfer between quantum dots and carbon nanotubes with nanometer resolution

This chapter is adapted from the following manuscripts, with minor modifications.

D. Nguyen, J. Lyding and M. Gruebele, Imaging energy transfer between quantum dots with nanometer resolution, *in preparation,* 2016.

D. Nguyen, J. Lyding and M. Gruebele, Imaging energy transfer between single quantum dots and carbon nanotubes, *in preparation,* 2016.

6.1. Abstract

Quantum dots have applications in photocatalysis and light harvesting because of their broad band absorption spectra and high quantum yield.[1-5] These processes involve the transfer of electrons or energy from one dot to another.[1,2,6] The time dependence of energy transfer processes has been measured.[6-8] but they are difficult to visualize directly. We report single molecule optical absorption detected by scanning tunneling microscopy (SMA-STM)[9] to visualize excited states of quantum dots and energy pooling into acceptor dots with sub-nanometer spatial resolution. We also show that we can tune quantum dots through different states with their own unique electron density signature, roll dots and the corresponding features on the surface, and switch from one acceptor dot to another by pruning away the dominant acceptor dot. Our observations are consistent with models of direct FRET or surface-mediated coupling among the dots.[10-12]

6.2. Energy transfer between single quantum dots

The observation of multiple charge carrier or exciton generation in many different types of quantum dots at sufficiently high excitation energy[13-15] makes quantum dots promising candidates for highly efficient solar cells, photocatalysis, and other photochemical applications. In such applications, a thin film of quantum dots is generally used. A heterogeneous distribution of quantum dot size, shape, and defects can greatly affect the performance of such films.[16-18] While bulk measurements have yielded many insights into energy transport among donor-acceptor dots in clusters as well as films of dots,[6,18] capturing the dot-by-dot heterogeneity of

transport processes is important for understanding how photoexcited energy flows among quantum dots.

Direct visualization of excited states of coupled quantum dots at sub-nanometer spatial resolution can provide such characterization. To do so, we have observed room temperature optical absorption of single PbS, CdSe and CdSe/ZnS quantum dots deposited on gold (Au), crystalline silicon carbide (c-SiC) and amorphous silicon carbide (a-SiC) surfaces using SMA-STM. In contrast to scanning tunneling spectroscopy,[19] the SMA-STM signal measures the weighted electron density difference between two orbitals coupled by optical excitation with sub-nm resolution even when the orbitals are not resonant with the tunneling Fermi level (Figure 6.1 and Figure 6.5). The signal is obtained by rear-illuminating the sample with amplitude-modulated (or frequency-modulated) laser light, and detecting the modulation of the tunneling current at the laser modulation frequency with a lock-in amplifier after minimizing photocurrents and thermal perturbation of the sample.[20]

Figure 6.2 shows topographic STM (orange scale) and SMA-STM (gray scale) images of PbS quantum dots in various configurations on the Au surface. Green light excitation was used in the example shown, with additional examples of CdSe and CdSe/ZnS quantum dots on Au, and PbS quantum dots on c-SiC and a-SiC surfaces shown in Figure 6.7. For PbS quantum dots, 532 nm excitation accesses a regime well above the bandgap, where the exciton pathlength is short and the electronic structure can be approximated as free carrier excitation with a short mean free path.[21] A single PbS quantum dot is shown in Figure 6.2ab. The absorption image has a C-shape, characteristic of optical excitation into an $l>0$ angular momentum state in the presence of a defect near the surface.[20] An example of a quantum dot pair with different diameters is shown in Figure 6.2cd. The localization of absorption signal on the smaller quantum dot is due either to direct absorption without energy transfer, or energy transfer from the larger dot if the smaller dot has in-gap states. The spherically uniform signal indicates that either the directly excited state relaxed, or energy transfer occurred into a manifold of degenerate orbitals with uniform average electron density. An example of a cluster of 3 quantum dots is shown in Figure 6.2ef, where the absorption signal is only observed on the biggest quantum dot at the top, indicative of energy transfer. After a tip change two-thirds of the way through scanning the top dot, (marked by the arrow), the absorption signal disappears. Thus, the absorption is sensitive to the Stark effect from the tip applied electric field (Figure 6.1d). An example of a cluster of 4 quantum dots with nearly

uniform absorption is shown in Figure 6.2gh. The top quantum dot absorbs more strongly. Thus absorption by single quantum dots in many configurations can be observed, highlighting nm-scale electronic structure (e.g. defects, or boundaries between excited and unexcited quantum dots).

We are able to tune the optical absorption between different orbitals by changing the sample bias voltage and thus the applied electric field, a capability previously demonstrated for PbS quantum dots.[20] Figure 6.3a shows a pair of CdSe/ZnS quantum dots with absorption images shown in Figure 6.3b-d. With increasing electric field, the absorption image of the top left quantum dot does not change significantly. In contrast, the image of the bottom right quantum tunes through a transition involving a O-shaped (higher angular momentum) orbital electron density. More voltages are shown in Figure 6.8. After a tip change, by processing the tip at -8 V and 1 nA on a different area of the surface and returning to the two dots, the optical absorption image changes completely (Figure 6.3e). The SMA-STM signal can be Stark tuned either by changing the voltage at constant tip shape (Figure 6.3b-d), or altering the tip shape to change the field ε associated with a given bias voltage V (Figure 6.2f and 6.3e).

The SMA-STM absorption signal of the quantum dots has a 3-D shape that depends on the orbital density difference of the two orbitals connected by excitation. Using the STM tip, we can roll the quantum dots on the surface to image their 3-D absorption projected into the surface plane. Figure 6.3f shows how rolling will lead to different images of a localized absorption feature (e.g. due to a defect). In the topography images of Figure 6.3g, a CdSe/ZnS quantum dot is rolled on the surface along the direction marked by the blue arrow. The quantum dot settles on the new adsorption site (Figure 6.3h). The corresponding absorption images in Figure 6.3i-j show how the SMA-STM signal rolls along. Additional optical absorption images at different voltages are shown in Figure 6.9. Using this rolling tomography, different projections of orbital density differences excited by the laser can be imaged to reconstruct a more complete picture of the electronic structure of the quantum dot.

Finally, the lifetimes associated with quantum dot excited states and laser excitation allow observation of energy transfer. PbS quantum dots are excited well above the bandgap at 532 nm (free carrier or bi-exciton states).[13,21] The intraband relaxation time to the first excited state is sub-ps,[22] and the Rabi cycle time at our laser power is 2 ps for bi-excitons (Methods). The first excited state relaxation time is 700-2000 ns,[7,8] whereas the FRET energy transfer time

is only 130-400 ns,[7,8] Thus PbS quantum dots are most likely relaxed to the first excited state before the first energy transfer occurs, and then energy transfer occurs if an acceptor is available, rather than relaxation all the way to the ground state. (For CdSe and CdSe/ZnS quantum dots: the Rabi cycle time for single excitons is 42 ps at our laser power; the first excited state, which we excite directly at 532, has a 24 ns relaxation time; the FRET time is 0.7-1.9 ns.[6])

Thus energy funneling pathways can be imaged by SMA-STM, with a central acceptor dot expected to show the strongest signal, nearby dots a weaker signal, and farther surrounding donor dots little or no signal, until the next acceptor dot is reached. Since relaxation occurs at each energy transfer step, one expects a uniform SMA-STM signal of the type shown in Figure 6.2df, rather than a localized orbital shape, as in Figures 6.2b and 6.3c.

We tested this prediction by imaging roughly hexagonally packed arrays of quantum dots (Figure 6.4a) to obtain direct evidence for energy transfer that leads to pooling of the SMA-STM signal into a single acceptor quantum dot. As shown in Figure 6.4b, quantum dot "1" is such an acceptor with a strong uniform SMA-STM signal, surrounded by quantum dots with weaker signals, and little or no signal from further away donors, except for a second acceptor dot "2". The observed gradient shows that we can image the energy funneling pathways.

Energy transfer in thin films of quantum dots has been investigated in bulk arrays of PbS quantum dots, and has a Förster radius of 8-13 nm,[7,8] Electron transfer by the Dexter mechanism had a very short exponential range ~exp[-r/0.5 nm], where r is the separation between the donor and the acceptor. In our arrays of quantum dots, the separation between dots is ≈ 2 nm due to bulky surface ligands (Figure 6.7 inset and 6.11). Thus energy transfer is much more likely than electron transfer. An alternative interpretation of Figure. 6.4b is that a single central dot is excited, and its energy relaxes to phonons and heats nearby quantum dots. However, given that large separation between quantum dots due to surface ligands, heat transfer is improbable.

Energy funneling results in a testable prediction that is different from heat transfer: If the final acceptor quantum dot is removed in an energy transfer mechanism, then the SMA-STM signal should shift to different quantum dot(s) that originally served as donor(s). If instead one removes the absorbing dot from which heat transfer originates, no signal should be observed on any other dots. To test this prediction, we used the STM tip to move acceptor quantum dots out of the way. One example is shown in Figure 6.4c-f. The topography of the initial cluster of 5 PbS quantum dots is shown in Figure 6.4c, with its absorption image in Figure 6.4d. The SMA-STM

signal is strongest on quantum dot "3", weaker on dots "4" and "5", and no signal is observed on dots "6" and "7". Thus dot "3" is potentially the main acceptor. After dots "3" and "4" are removed, the absorption signal shifts mainly to dot "6", which becomes the new energy acceptor. Dot "7" still does not show a strong signal, confirming that we are imaging an energy transfer pathway starting from dot "6" though dots "5" and "4" into dot "3" in Figure 6.4d.

Finally, we note that energy transfer in thin films of quantum dots can be direct[6-8] or surface-mediated, such as by plasmons that can be excited in our gold surface.[10] Our observation of energy pooling on both a metallic Au surface and on a semiconducting c-SiC surface (Figure 6.10) is consistent with both observed mechanisms. We note that our SMA-STM absorption signal on the Au surface always is stronger than on the c-SiC surface (bandgap 2.8 eV), suggesting that optical absorption by the quantum dots is enhanced by plasmons on the Au surface. An absorption signal of PbS quantum dots is also observed on the a-SiC surface (Figure 6.7e-f). When that smaller bandgap surface (~ 1.8 eV)[23] is excited by 532 nm light, direct energy transfer from the surface to the PbS quantum dots (~ 1 eV band gap) is also possible. Thus SMA-STM can be used to directly visualize with nanometer resolution energy pooling pathways among multiple quantum dots, guided by both direct and surface-enhanced excitation and energy transfer mechanisms. It will be interesting to see if direct charge transfer from dot to dot or charge injection from the surface can also be observed when bare dots with tighter packing are observed.

6.3. Energy transfer between single quantum dots and carbon nanotubes

SMA-STM was used to investigate energy transfer between single QDs and CNTs. Figure 6.14a shows a PbS QD and a CNT on the PtAu surface. At a separation of ~ 12 nm, there is no absorption signal on the CNT while the QD shows strong signal, as shown in Figure 6.14b. The QD was moved closer to the CNT (Figure 6.14c). At the new position at ~ 6 nm of separation, a negative absorption signal is observed on the CNT (Figure 6.14d). This indicates that there is a distance-dependent energy transfer from the QD to the CNT.

Another example of QD and CNT energy transfer on PtAu surface is shown in Figure 6.14e-l. The QD was moved closer to the CNT and strong absorption signal on the CNT is observed (Figure 6.14h) . However, when the CNT was moved even closer to the QD, the absorption on the CNT and QD disappears (Figure 6.14l). This data indicates that, either the

energy transfer is orientation-dependent, or the interaction between the QD and CNT shifts their energy levels out of resonance, given their not very small physical sizes and close separation. More examples of energy transfer between single QDs and CNTs on PtAu surface are given in Figure 6.15.

Another interesting observation is that when the bias voltage is varied, the absorption is shifted from the edge (Figure 6.14h,i) to the middle of the CNT (Figure 6.14j). Similar observations are seen on the same type of QD and CNT on the semiconducting c-SiC surface (Figure 6.16). The mechanism of localized absorption signal on the CNTs is not clear at this point.

Figure 6.17 shows two examples of CNTs embedded in arrays of PbS QDs on PtAu surface. Strong positive absorption signal is observed on the CNTs and surrounding QDs in the 90^{o} out of phase LIA images. It suggests that, these CNTs and QDs are heated, probably resulting from long-time nonradiative relaxation and heat transfer.

6.4. Methods

6.4.1 Substrate preparation

Three different substrates were employed in this study: ultrathin PtAu film on sapphire, crystalline silicon carbide (c-SiC) and amorphous silicon carbide (a-SiC). Ultrathin PtAu films on c-plane sapphire substrate (preannealed at ~ 1273 K for 12 hours) were fabricated by electron beam deposition.[24] 5 nm of Pt layer was deposited at the substrate temperature of ~ 1050-1070 K, followed by deposition of 10 nm of Au at ~ 670 K. In order to obtain total internal reflection, a 3 mm fused silica right angle prism (Thorslab) was glued to the back of the samples using a transparent, UHV compatible epoxy (302-3M, Epotek) and cured overnight. Two long edges of the samples were painted with colloidal Ag (TedPella Inc.) to improve electrical contact with sample holders. The samples were degassed at ≈400 K for at least 12 hours before STM imaging.

n-type 4H-SiC (Cree Inc., resistivity ~ 0013-0500 Ω. cm) was used as a semiconducting substrate. To obtain total internal reflection, a 15^{o} wedge was machined at the back side of the sample, then polished until optical quality was obtained using diamond polishing paste. c-SiC samples were resistively degassed at ~ 870 K for at least 6 hours or until the pressure is lower than 10^{-7} Pa. Atomically flat and clean c-SiC surface was prepared by annealing at ~ 1270 K and

~ 1370 K for 10 minutes, then heating to ~ 1470 K for 60 seconds to remove oxides. The cleanness and semiconducting nature of the surface were checked using STM and STS.

a-SiC substrate was prepared from c-SiC substrate. Both prism and wedging methods were used to obtained total internal reflection. The samples were degassed at ~ 400 K for ~ 12 hours. Thin a-SiC films (ca. ~ 50-100 nm) were produced by sputtering degassed c-SiC with 2 keV argon ions for ~ 1 hour, with base pressure $\leq 3 \times 10^{-3}$ Pa.[23]

6.4.2. Quantum dot deposition

PbS (Evident Thermoelectrics), CdSe (NN-Labs) and CdSe/ZnS (Ocean NanoTech) quantum dots dispersed in toluene with corresponding nominal diameters of 4.2 nm, 3.0 nm and 5.5 nm were used as received. The first exciton absorption peaks for PbS, CdSe and CdSe/ZnS quantum dots are 1228 nm, 538 nm and 530 nm, as shown in Figure 6.6. The surfaces of PbS, CdSe and CdSe/ZnS quantum dots are capped with oleic acid, octadecylamine and octadecylamine, respectively. The quantum dots were deposited onto clean surfaces under ultrahigh vacuum using matrix-assisted dry contact transfer (DCT) in which carbon nanotubes were used as a matrix to prevent quantum dot aggregation. CNT powder was loaded onto a frayed fiber glass piece tied onto a tip holder, then 2-5 drops (~ 20 µL) of quantum dot solutions (10 mg/mL) were added. The DCT applicators were gently degassed at elevated temperature (ca. ~ 370 K) for ~ 12 hours while keeping the pressure $\leq 10^{-6}$ Pa. This degassing procedure has been shown to not affect the quantum dot fluorescence and absorption.[20]

6.4.3. STM setup

STM experiments were performed using a home built STM with base pressure $\leq 7 \times 10^{-9}$ Pa.[25] Electrochemically etched W and mechanically cut Pt-Ir (80:20) tips were used. All of the presented data were collected using Pt-Ir tips, except for where noted. The samples were irradiated with p-polarized 532 nm light (diode pumped solid-state laser) with total internal reflection in order to reduce tip heating effects. The laser was amplitude modulated at 2.2 kHz using a mechanical chopper wheel. Topographic and absorption images were simultaneously collected using the STM and a lock-on amplifier. Our technique approximately detects the electron density difference between the ground and excited states.[20] The laser power density was ca. 1200-2600 mW/mm^2.

Quantum dots were manipulated on the surfaces following a procedure described in ref. 26. The tip first scans a line (~ 15- 20 nm) over the quantum dot, then scans the same line, but is moved down by a preset value (typically 0.7 nm). An interpolation distance (20-50% of the line length) can be defined at the middle for which the tip is moved horizontally.

6.4.4. Rabi cycle calculations

Rabi frequencies were estimated for on-resonance excitation as $\omega_R = \mu_{ij}E/\hbar$ where E is the electric field amplitude of the linearly polarized light field and μ_{ij} is the transition dipole moment between states i and j. The electric field was calculated from irradiance ($I \approx$ 1630 mW/mm^2) as $E = \sqrt{2I/c\varepsilon_0} \approx 3.5\text{x}10^4$ V/m, where c is the speed of light and ε_0 is the permittivity of free space. A field enhancement factor of 30 was used for PtIr tips. For PbS quantum dots, the transition dipole moment was calculated from the resonance frequency ($\omega_{ij} \approx 3.54\text{x}10^{15}$ rad/s at 532 nm) and the radiative lifetime of the bi-excition (τ = 50 ps, given the excitation energy at 532 nm is ≈ 2 times higher than the bandgap at ≈ 1200 nm) as $\mu_{ij} = (3\varepsilon_0 hc^3/2\tau\omega_{ij}^3)^{1/2}$. This gave a Rabi cycle for PbS quantum dots of ≈ 2 ps. For CdSe and CdSe/ZnS quantum dots, the radiative lifetime of the single exciton τ = 24 ns was used because the excitation is near the bandgap which gave a Rabi cycle of ≈ 42 ps.

6.4.5. Perturbation theory for SMA-STM signal

The tip-quantum dot-surface system is described by a double barrier tunnel junction and is schematically shown in Figure 6.5. The tunneling probability is given by Fermi Golden rule:

$$k(E) = \frac{2\pi}{\hbar}|M|^2\rho_{final} \tag{6.1}$$

where M is the matrix element and ρ_{final} is the density of states (we write the expression for a single initial state for simplicity, so$\rho_{initial}$ does not appear. Given the small density of states of the quantum dots compared to the metal tip and surface, second order perturbation theory is required:

$$M = M^{(1)} + M^{(2)}$$
$$= \langle\psi_{M1}(\vec{x})\big|\hat{H}_{tunnel}\big|\psi_{M2}(\vec{x})\rangle - \sum_{i'}\frac{\langle\psi_{M1}|\hat{H}_{tunnel}|i\rangle\langle i|\hat{H}_{tunnel}|\psi_{M2}\rangle}{\Delta E_{iF}} \tag{6.2}$$

where $\Delta E_{iF} = \Delta E_{iF}^{(r)} - i\Gamma_i$ expresses the energy gap between tunneling level and state in the quantum dot in terms of the real gap and the decay rate Γ_i of the gap state $|i\rangle$. The state ψ_{M1} and ψ_{M2} of the tip and surface metals are degenerate, but the state $|i\rangle$ of the quantum dots is generally not degenerate. The tunneling Hamiltonian is given by the momentum operator in the tunneling z direction:

$$\widehat{H}_{tunnel} = \frac{-\hbar^2}{2m_e}\frac{\partial}{\partial z} \tag{6.3}$$

and the brackets in eq. (6.2) are integrals over area of the contact surface ds. Thus M still depends on z. i' is a sum over states available for tunneling, empty, or *1/2* filled with electrons. (Orbitals that are filled with two electrons are inaccessible due to Fermi statistics.)

Now consider excitation by light $h\nu$ resonant with transition $|j\rangle \rightarrow |k\rangle$, and neglect direct M_1 to M_2 tunneling at the larger value $z = r$ with the quantum dot in the junction. The matrix element M when the light is on is then approximately given by:

$$M = -\sum_{i' \neq j,k} \frac{M_{1i}M_{i2}}{\Delta E_{iF}} - \frac{M_{ik}M_{k2}}{\Delta E_{kF}} = \bar{M} + M_k \Rightarrow k_{on} \sim |\bar{M}|^2 + 2\,\mathbb{R}e\,\bar{M}M_k + |M_k|^2 \tag{6.4}$$

and when the light is off:

$$M' = -\sum_{i' \neq j,k} \frac{M'_{1i}M'_{i2}}{\Delta E_{iF}} - \frac{M'_{ij}M'_{j2}}{\Delta E_{kF}} = \overline{M'} + M'_j \Rightarrow k_{off} \sim |\bar{M}'|^2 + 2\,\mathbb{R}e\,\overline{M'}M'_j + \left|M'_j\right|^2 \tag{6.5}$$

The tunneling current is $I = ek$. Thus the difference in tunneling current when the laser is on and off is given by:

$$\Delta I \sim k_{on} - k_{off} \tag{6.6}$$

For simplicity, let us consider the excitation process as vertical. (That is, the orbital energies i' are not affected by excitation or charge injection into the quantum dot. This corresponds to removing the ' in eq. (6.5). In reality, there will be some overall shift of electronic structure and *M* and *M*' will not cancel perfectly, leaving a background signal). Three cases are possible.

In the first case, the tip Fermi level (set by the applied bias voltage V) is off-resonant with the state $|k\rangle$, and $|\bar{M}| \gg |M_k|, |M_j|$:

$$\Delta I \sim \mathbb{R}e\bar{M}\left(M_k - M_j\right) \tag{6.7}$$

Thus in the x, y plane, the signal is proportional to the amplitude difference of the two states involved in the optical transition multiplied by an average over occupied states.

In the second case, the tip Fermi level is on-resonant with the state $|k\rangle$, and $|\bar{M}| \ll |M_k|, |M_j|$:

$$\Delta I \sim |M_k|^2 - |M_j|^2 \sim a|\varphi_k(x,y;r)|^2 - |\varphi_j(x,y;r)|^2 \quad (6.8)$$

Thus the signal is proportional to the electron densities different between the states $|k\rangle$ and $|j\rangle$.

In the third case, the tip Fermi level is on-resonant with the state $|k\rangle$, and the state $|k\rangle$ decays to state $|j\rangle$ at a rate Γ_k. The signal then looks like a linear combination of the previous two cases. If $\Gamma_k \to 0$, it is similar to the first case and if $\Gamma_k \to \infty$, it is similar to the second case. Thus, regardless of the applied bias voltage, we either detect the amplitude magnitude difference of the orbitals coupled by light excitation, or the electron density difference between the orbitals $|k\rangle$ and $|j\rangle$ coupled by light excitation. Unlike STS, resonance of the system states in the tunneling gap between the two metal surfaces (tip and substrate) is not required, although the SMA-STM signal is a weaker current perturbation (typically 0.1 pA at 10 pA tunneling currents, as expected form the above equations for off-resonance excitation).

6.5. Figures

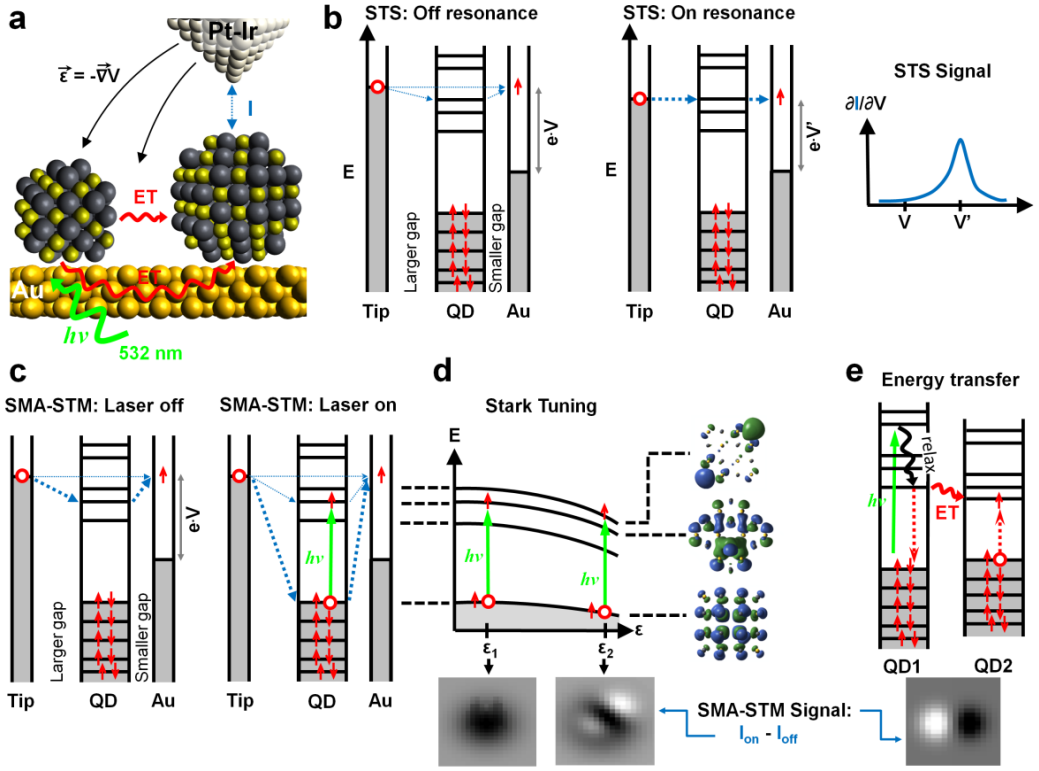

Figure 6.1: Schematic of the SMA-STM experiment. **a,** SMA-STM energy transfer arrangement for two PbS quantum dots with different diameters on the Au surface. The resonant quantum dot is excited at 532 nm (green arrow). Energy transfer (ET) to the larger dot can happen directly when dots are in close contact (top red arrow), or surface-mediated (bottom red arrow). **b,** Conventional STS (scanning tunneling spectroscopy): Off resonance, weak tunneling occurs via 1st order coupling (top horizontal blue arrow) and 2nd order coupling (lower two blue arrows). On resonance, when the bias of the quantum dot and Au surface is changed from V to V', the 2nd order coupling is resonantly enhanced by an empty orbital in the quantum dot (thick blue arrows), yielding a $\partial I/\partial V$ peak. **c,** SMA-STM experiment: When the laser is modulated on-off, a signal is obtained from 2nd order coupling, whether the quantum dot is resonant or not. Weak 1st order tunneling (horizontal blue arrow) always occurs, but cancels in the signal I_{on}-I_{off}. The 2nd order coupling is modulated by electronic excitation, with the amplitude of a tunneling path decreasing when an orbital is partly filled by laser excitation (thick blue arrows on left become thin blue arrows on right), and another tunneling path increasing when orbitals are partly emptied (new thick blue arrows on right). Thus the SMA-STM signal maps out a weighted difference of the orbital electron density of the two optically coupled states (see Methods). **d,** When the tip bias V is changed, the resultant change in electric field ε from ε_1 to ε_2 Stark-tunes the quantum dot orbital energies, so different orbitals (three are shown on right) enter optical resonance (green arrows). SMA-STM then highlights different electron density differences (gray-scale SMA-STM I_{on}-I_{off} images below ε_1 and ε_2 at bottom). **e,** Energy transfer (or electron transfer) from quantum dot 1 to quantum dot 2 leads to a change in orbital population, and thus a change in STM-SMA signal (gray-scale I_{on}-I_{off} image at bottom).

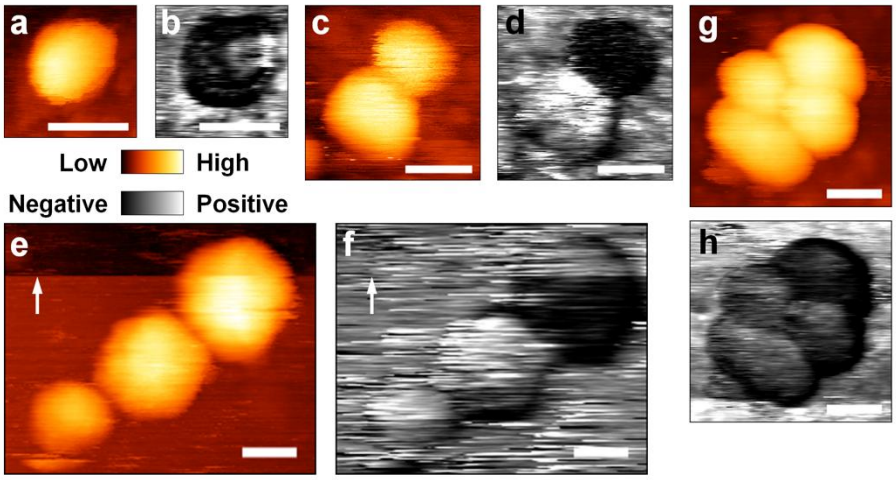

Figure 6.2: Absorption of single and small clusters of PbS quantum dots on Au surface. a, Topographic image (orange color scale) of a single quantum dot with corresponding absorption image in **b** (grey color scale -0.2 to 0.2 pA). Scanning conditions 10 pA, 1.9 V, laser power density 1630 mW/mm^2. **c-d,** A pair of quantum dots. Scanning conditions 10 pA, 1.7 V, grey color scale -0.4 to 0.4 pA, laser power density 1388 mW/mm^2. **e-f,** A cluster of 3 quantum dots. Scanning conditions 15 pA, 1.4 V, grey color scale -0.2 to 0.2 pA, laser power density 1630 mW/mm^2. **g-h,** A cluster of 4 quantum dots. Scanning conditions 5 pA, 1.1 V, grey color scale -0.4 to 0.4 pA, laser power density 1911 mW/mm^2. All scale bars 5 nm.

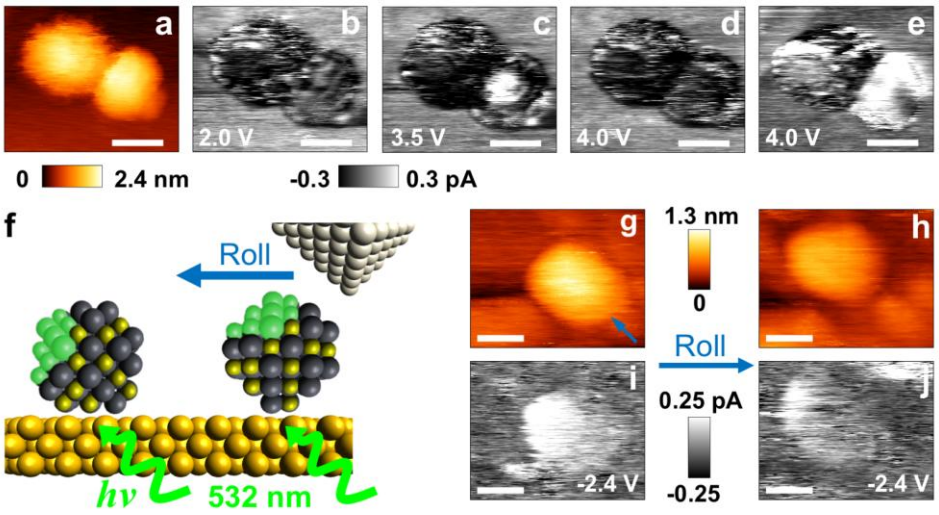

Figure 6.3: Tuning SMA with Stark effect and 3-D imaging of the SMA. a-e, Tuning orbitals into resonance with the Stark effect. **a**, Topographic image showing a CdSe/ZnS quantum dot pair on Au surface. Scanning conditions 5 pA, 2.5 V. **b-d**, Optical absorption images of the quantum dot pair in **a** with increasing sample bias voltage (applied electric field). Scanning current 5 pA, laser power density 1167 mW/mm^2. **e**, After a tip change and cleaning at 1 nA and -8 V, the absorption image changes due to change of the electric field at constant bias. Scanning conditions 20 pA, 4.0 V, laser power density 1167 mW/mm^2. **a-e**, Scale bars 4 nm. **f-j**, 3-D imaging of the absorption shape. **f,** Schematic of the experiment: a quantum dot with a localized optical absorption features is rolled left, resulting in a different projection of the orbital along the tunneling (z) axis. **g-h**, Topographic images of a single CdSe/ZnS quantum dot on Au surface before and after rolling with the tip. Scanning condition 10 pA, 2.7 V. **i-j,** Absorption images of the quantum dot in **g-h** showing rotation of the localized orbital electron density difference. Scanning current 10 pA, laser power density 1167 mW/mm^2, scale bars 5 nm. Data at additional bias voltages is shown in 6.9.

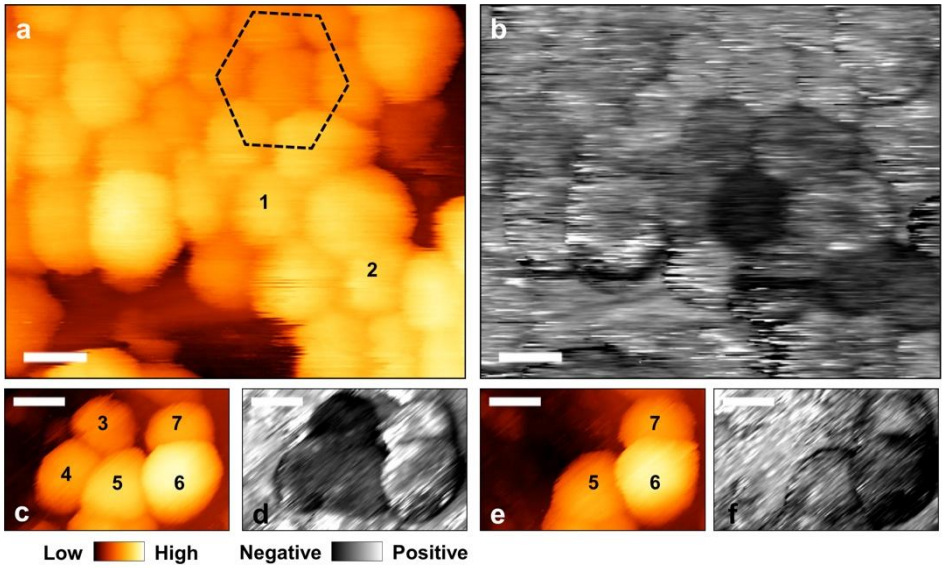

Figure 6.4: Imaging energy transfer between single quantum dots. a, A Topographic image showing an array of PbS quantum dots on Au surface. Short range hexagonal packing is highlighted. **b,** Corresponding absorption image. Scanning conditions 10 pA, 1.5 V, grey color scale -0.2 to 0.2 pA, laser power density 1630 mW/mm^2, scale bars 5 nm. **c,** Topographic image of a cluster of 5 PbS quantum dots with absorption image shown in **d**. The SMA-STM signal shows energy pooling in quantum dot 3, with some signal in adjacent dots 4 and 5. **e,** Topographic image of the same cluster as in **c**, after quantum dots 3 and 4 have been moved away. **f,** The corresponding laser absorption image shows that quantum dots 6 and 7 now carry some signal. Scanning conditions 5 pA, 1.5 V, grey color scale -0.4 to 0.4 pA, laser power density 1911 mW/mm^2, scale bars 5 nm.

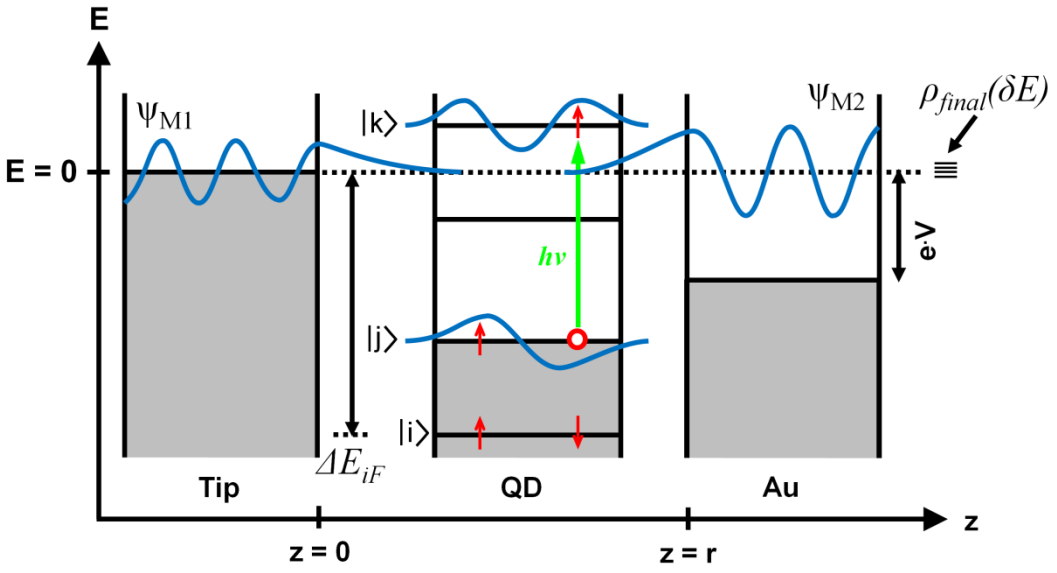

Figure 6.5: Schematic diagram of the double barrier junction. Tip and Au surface are sufficiently separated (by r) so the direct tunneling matrix element $M^{(1)}$ is small. Instead, tunneling can occur resonantly through states of the discrete system (molecule, quantum dot, etc.) in the gap (STS and SMA-STM), or also off-resonantly (SMA-STM only shown here). Excitation of system states perturbs the off-resonant tunneling pathways: previously unoccupied pathways can be filled or partly filled, occupied ones are emptied or partly emptied, changing the probability amplitudes. Thus a signal measuring differences between orbital shapes (or, in the resonant case, a single orbital shape) can be measured.

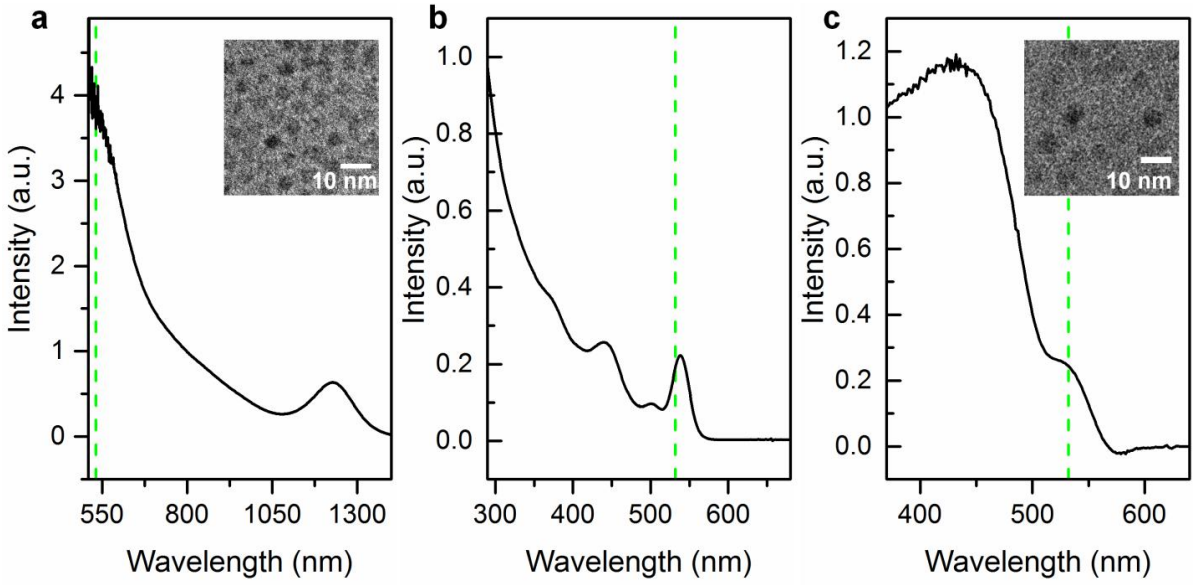

Figure 6.6: Bulk absorption spectra of the investigated quantum dots. a, PbS quantum dot. Inset: a TEM image showing the quantum dot size. **b,** CdSe quantum dot. **c,** CdSe/ZnS quantum dot. Inset: a TEM image showing the quantum dot size and separation. The dashed green line highlights the excitation wavelength at 532 nm.

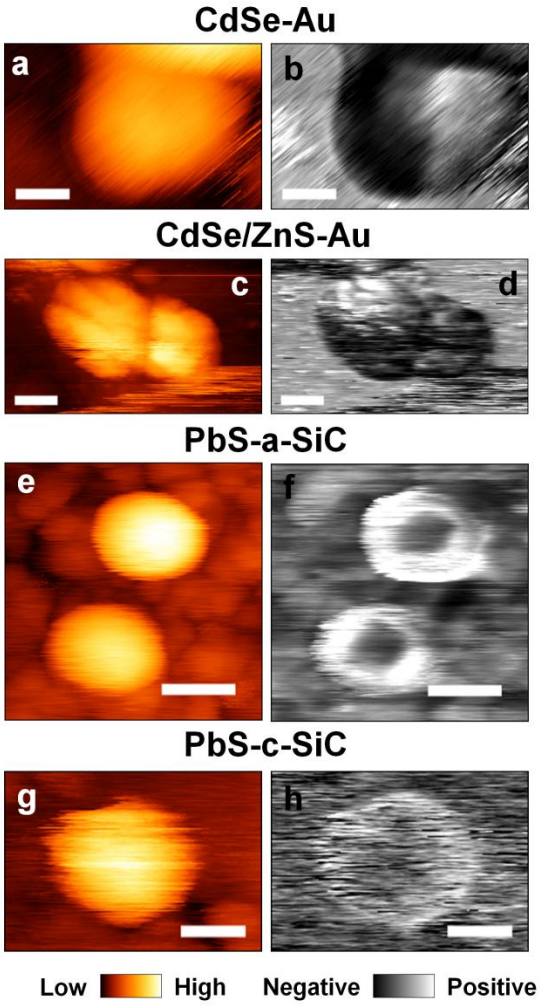

Figure 6.7: Additional absorption examples of single and small clusters of quantum dots. a-b, A pair of CdSe/ZnS quantum dots on Au surface. Scanning conditions 5 pA, 1.6 V, grey color scale -0.4 to 0.4 pA, laser power density 1610 mW/mm^2, scale bars 2 nm. **c-d,** A pair of CdSe/ZnS quantum dots on Au surface. Sub-quantum dot crystallographic structure is resolved in **c**. Scanning conditions 5 pA, 3.0 V, grey color scale -0.3 to 0.3 pA, laser power density 1168 mW/mm^2, scale bars 5 nm. **e-f,** A pair of PbS quantum dots on a-SiC surface. Scanning conditions 10 pA, -1.8 V, grey color scale -0.25 to 0.25 pA, laser power density 1630 mW/mm^2, scale bars 3 nm, W tip. **g-h,** A single PbS quantum dots on c-SiC surface. Scanning conditions 10 pA, 1.1 V, grey color scale -0.05 to 0.05 pA, laser power density 2620 mW/mm^2, scale bars 3 nm, W tip.

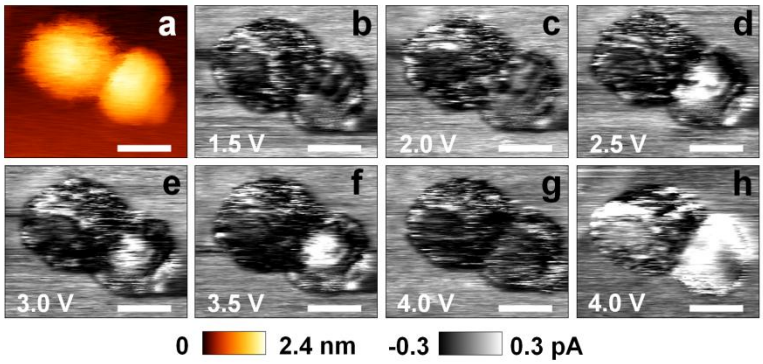

Figure 6.8: Additional absorption images at different sample bias voltages for the quantum dot in Figure 6.3a. a, Topographic image showing a CdSe/ZnS quantum dot pair on Au surface. Scanning conditions 2.5 V, 5 pA. **b-g,** Absorption images with increasing the electric field for the pair in **a**. Scanning current 5 pA. **h,** After a tip change and cleaning at 1 nA and -8 V, the absorption shape changes significantly. Scanning conditions 20 pA, 4.0 V, laser power density 1167 mW/mm^2, scale bars: 4 nm.

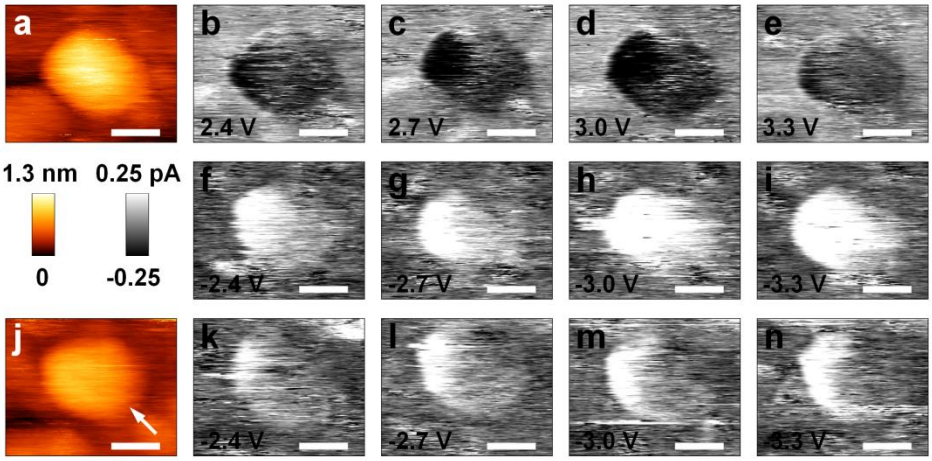

Figure 6.9: Additional absorption images at different sample bias voltages for the quantum dot in Figure 6.3g-h. a, Topographic image showing a single CdSe/ZnS quantum dot on Au surface. Scanning conditions 10 pA, 3.0 V. **b-i,** Absorption images of the quantum dot in **a** with varying sample bias voltage (or electric field). Scanning current 10 pA. **j,** Topographic image of the same quantum dot in **a** after being rolled along the direction of the arrow. Scanning conditions 10 pA, -3.0 V. **k-n,** Absorption images of the quantum dot at the new position in **j**. Scanning current 10 pA, laser power density 1167 mW/mm^2, scale bars 5 nm.

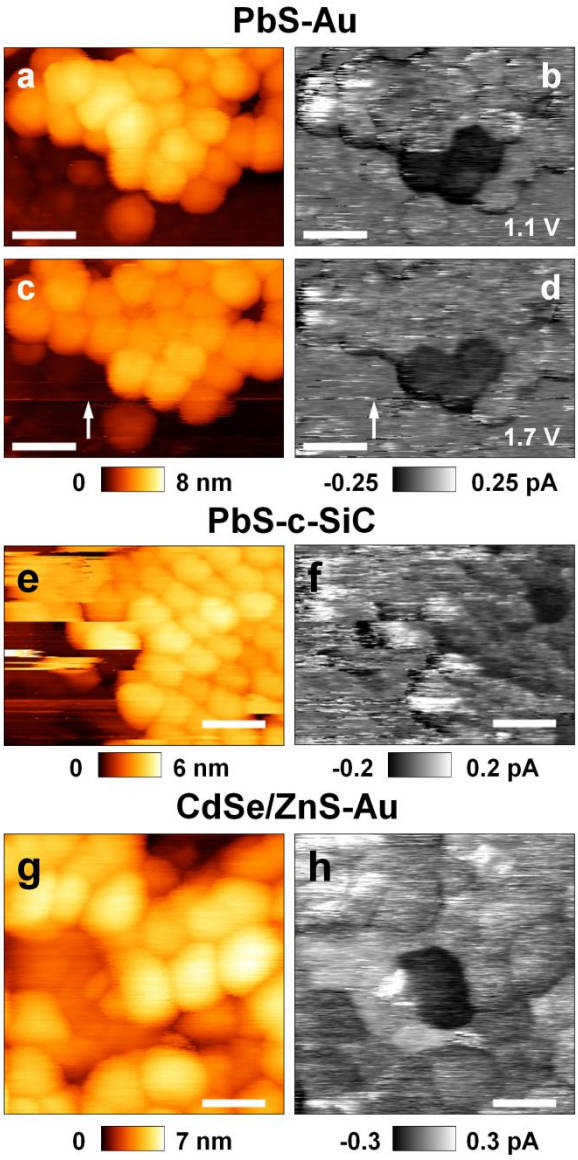

Figure 6.10: More examples of absorption in arrays of quantum dots. a-b, An array of PbS quantum dots on Au surface scanned at 1.1 V. **c-d,** The same cluster in **a-b** scanned at higher voltage 1.7 V. The absorption shape remains unchanged when the number of dots, tip (highlighted by arrow) and electric field are changed suggesting that the photoexcited energy is funneled to the bottom three quantum dots. **a-d,** Scanning current 10 pA, laser power density 1630 mW/mm^2, scale bars 10 nm. **e-f,** A cluster of PbS quantum dots on c-SiC surface. Scanning conditions 10 pA, 1.3 V, laser power density 2620 mW/mm^2, scale bars 10 nm, W tip. **g-h,** A cluster of CdSe/ZnS quantum dots on Au surface. Scanning conditions 10 pA, 3.5 V, laser power density 1167 mW/mm^2, scale bars 10 nm.

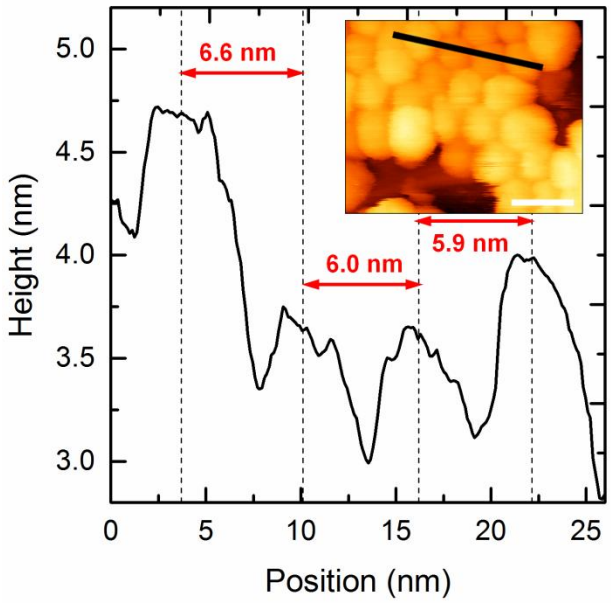

Figure 6.11: Interdot separation in PbS quantum dot arrays. STM height profile of the line in the inset STM image (scale bar 10 nm) showing the interdot separation. The separation between single quantum dots in the array is > 1 nm, given the diameter of the PbS quantum dots of ≈ 4.2 nm. This separation is consistent with TEM measurement shown in the inset of the Figure 6.6a.

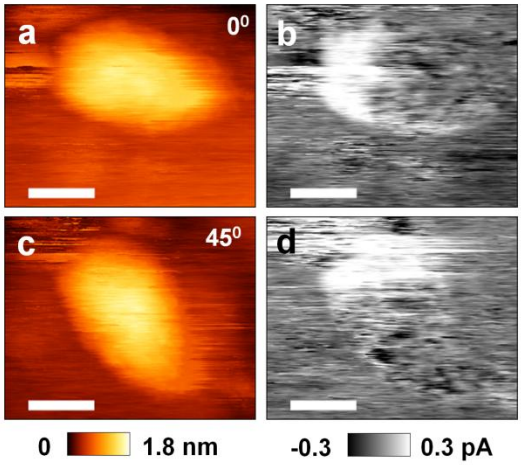

Figure: 6.12: Independence of the absorption shape on the scanning direction. a, Topographic image showing an elongated CdSe/ZnS quantum dot on Au surface scanned at 0^o and with absorption image in **b**. **c,** The same quantum dot in **a** scanned at 45^o and absorption image is shown in **d**. The absorption shape is independent of the scanning direction. Scanning conditions 5 pA, -3.0 V, laser power density 1167 mW/mm^2, scale bars 4 nm.

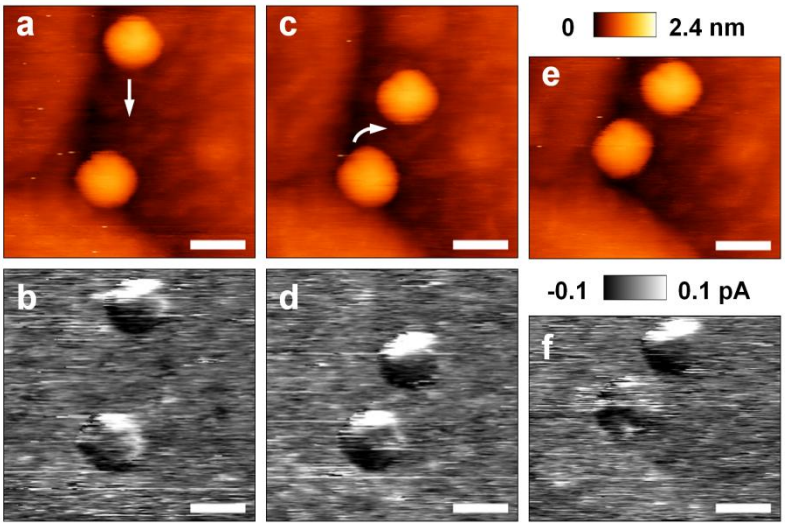

Figure 6.13: Interaction between two single PbS quantum dots. a, A pair of PbS quantum dots with absorption image in **b**. **c-d**, After the top quantum dot is translated to be closer to the bottom quantum dot, the absorption shapes of the two quantum dots are aligned. **e-f,** After the bottom quantum dot is rotated, the alignment disappears even when the separation between the two quantum dots is smaller indicating that the interaction is orientation-dependent. Scanning conditions 10 pA, 1.0 V, laser power density 1630 mW/mm^2, scale bars 5 nm.

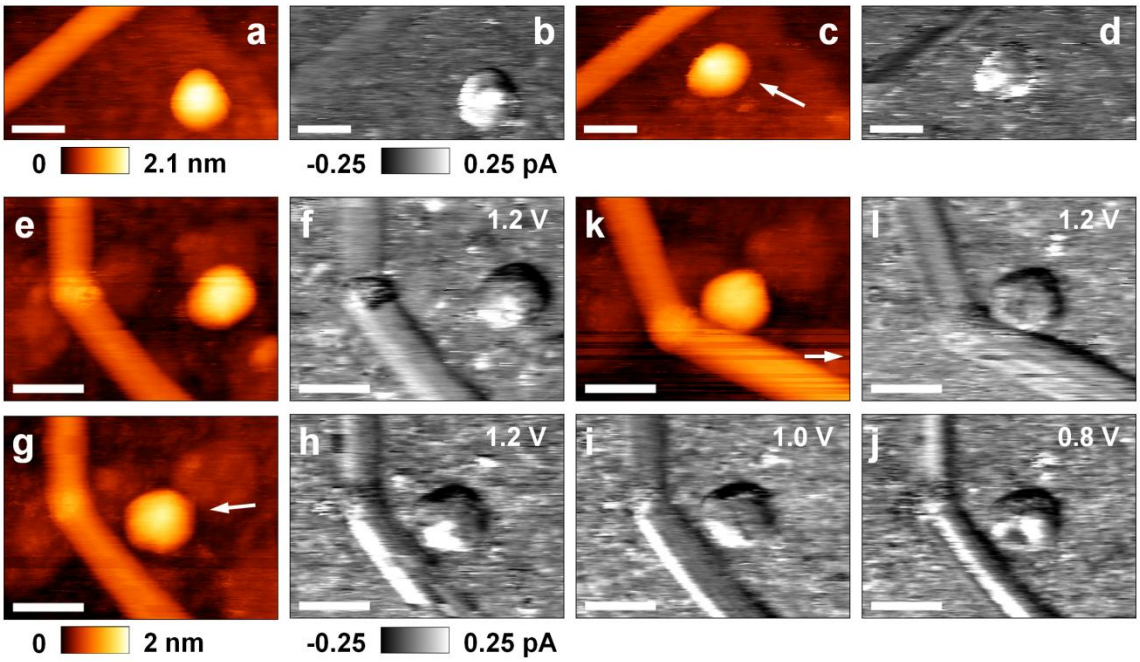

Figure 6.14: Energy transfer between PbS QDs and CNTs on Au surface. (a) STM topographic image showing a PbS QD and a CNT. At that separation of ~ 12 nm, no absorption signal is observed on the CNT, while the QD shows strong nonuniform signal, as shown in (b). (c) Using the STM tip, the QD is moved closer to the CNT. (d) At the separation of ~ 6 nm, strong signal is observed on the left edge of the CNT suggesting that energy is transfer from the QD to the CNT. Scanning conditions 20 pA, 1.3 V, laser power density 1135 mW/mm^2, scale bars 5 nm. (e-j) Another example of energy transfer between QD and CNT. (e-f) Residual absorption signal is observed on the CNT when the QD and CNT separation is ~ 10 nm. (g-j) At the separation of ~ 5 nm, strong signal is observed on the left edge of the bottom part of the CNT. The signal is shifted to the middle when the sample bias voltage is changed from 1.2 V to 0.8 V. (k-l) When the CNT is moved even closer to the QD at ~ 3 nm, the signal on the CNT disappears. It suggests that, The energy transfer between the QD and CNT is not only separation-dependent, but also orientation-dependent. Scanning current 20 pA, , laser power density 1630 mW/mm^2, scale bars 5 nm.

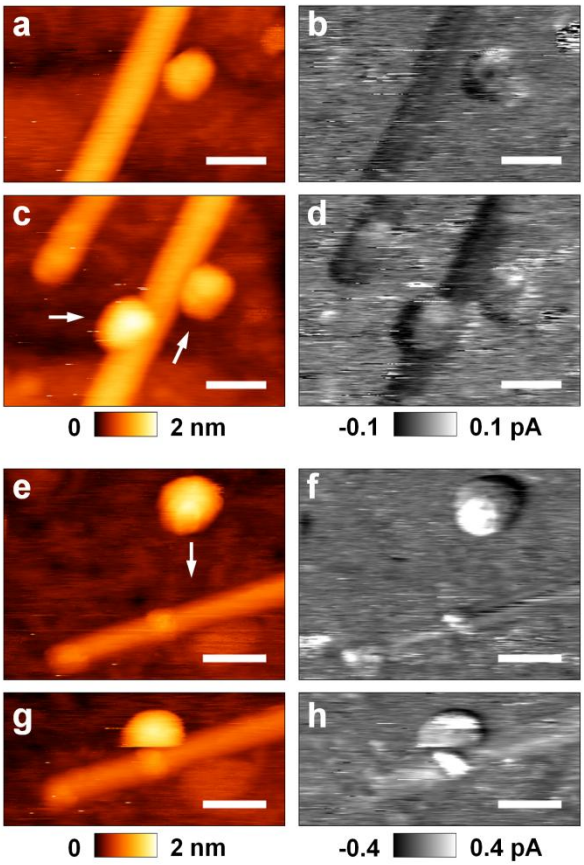

Figure 6.15: More examples of energy transfer between PbS QDs and CNTs on Au surface. (a-d) When there are two QDs close to the CNT (c-d), the absorption intensity on the CNT is stronger than when there is only one QD (a-b). Scanning conditions 20 pA, 1.4 V, laser power density 1630 mW/mm^2, scale bars 5 nm. (e-h) When the QD is moved closer to the CNT, the absorption of the defect is substantially stronger (g-h). Scanning conditions 20 pA, 1.0 V, laser power density 1630 mW/mm^2, scale bars 5 nm.

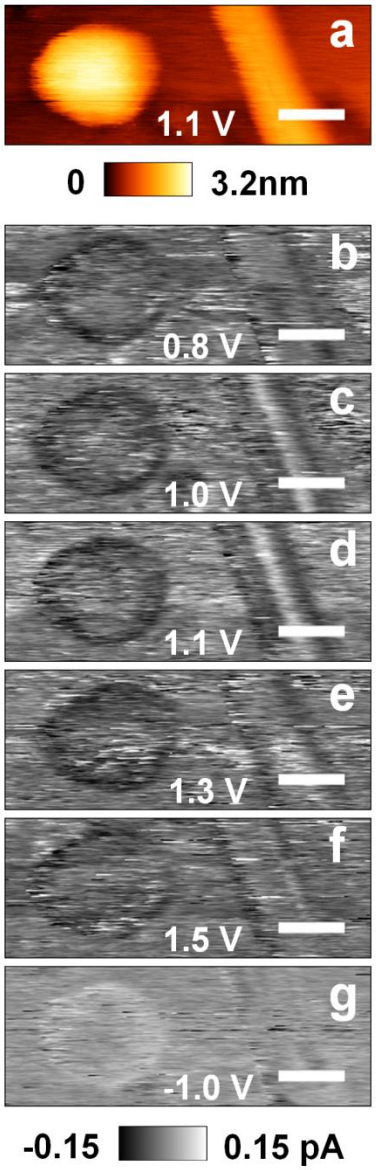

Figure 6.16: Interaction between single PbS QD and CNT on c-SiC surface. When the bias voltage is varied, there appears a positive signal at the middle of the CNT at 1.0-1.1 V (c-d). This observation is consistent with data on Au surface. Scanning current 10 pA, laser power density 2620 mW/mm^2, scale bars 4 nm.

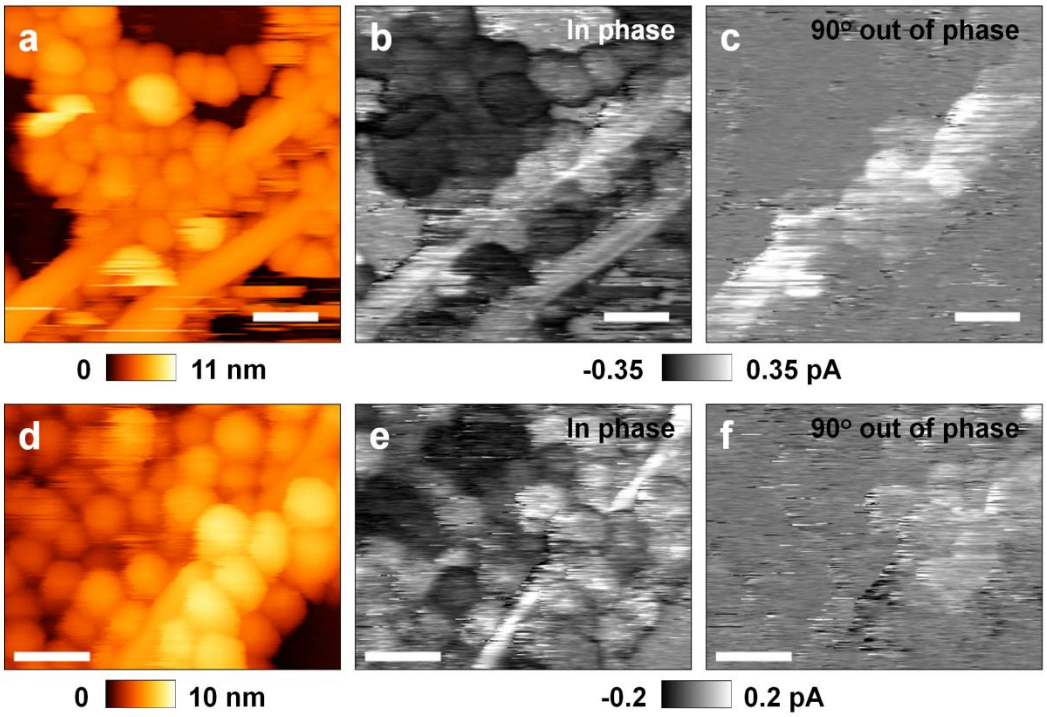

Figure 6.17: Interaction between QDs and CNTs on Au surface. (a) STM topographic image showing two CNTs embedded in an array of QDs. Strong positive absorption signal is observed on the top CNT and surrounding QDs in the 90^{o} out of phase LIA image. Scanning conditions 15 pA, 1.4 V, laser power density 1630 mW/mm^{2}, scale bars 10 nm. (d-f) Another example of the observation in (a-c). In this case, positive signal is only observed on the surrounding QDs in the 90^{o} out of phase LIA image. Scanning conditions 10 pA, 1.3 V, laser power density 1630 mW/mm^{2}, scale bars 10 nm.

6.6. References

1. I. Gur, Science, 310, 462–465 (2005).
2. P. V Kamat, J. Phys. Chem. C, 112, 18737–18753 (2008).
3. E. H. Sargent, Nat. Photonics, 6, 133–135 (2012).
4. X. Chen, L. Liu, P. Y. Yu and S. S. Mao, Science, 331, 746–750 (2011).
5. Z. Han, F. Qiu, R. Eisenberg, P. L. Holland and T. D. Krauss, Science, 338, 1321–1324 (2012).
6. S. A. Crooker, J. A. Hollingsworth, S. Tretiak and V. I. Klimov, Phys. Rev. Lett., 89, 186802 (2002).
7. R. Bose, J. F. McMillan, J. Gao, K. M. Rickey, C. J. Chen, D. V Talapin, C. B. Murray and C. W. Wong, Nano Lett., 8, 2006–2011 (2008).

8. S. W. Clark, J. M. Harbold and F. W. Wise, J. Phys. Chem. C, 111, 7302–7305 (2007).

9. J. Ballard, E. Carmichael, J. Lyding and M. Gruebele, Nano Lett., 6, 45–49 (2006).

10. H. Xu, J. Liu, X. Duan, J. Li, J. Xue, X. Sun, Y. Cai, Z.-K. Zhou and X. Wang, Opt. Mater. Express, 4, 2586–2594 (2014).

11. W. A. Tisdale and X.-Y. Zhu, Proc. Natl. Acad. Sci., 108, 965–970 (2011).

12. K. F. Chou and A. M. Dennis, Sensors, 15, 13288–13325 (2015).

13. R. J. Ellingson, M. C. Beard, J. C. Johnson, P. Yu, O. I. Micic, A. J. Nozik, A. Shabaev and A. L. Efros, Nano Lett., 5, 865–871 (2005).

14. A. J. Nozik, Chem. Phys. Lett., 457, 3–11 (2008).

15. M. C. Beard, K. P. Knutsen, P. Yu, J. M. Luther, Q. Song, W. K. Metzger, R. J. Ellingson and A. J. Nozik, Nano Lett., 7, 2506–2512 (2007).

16. D. S. Ginger and N. C. Greenham, J. Appl. Phys., 87, 1361 (2000).

17. Y. Zhang, D. Zherebetskyy, N. D. Bronstein, S. Barja, L. Lichtenstein, D. Schuppisser, L.-W. Wang, A. P. Alivisatos and M. Salmeron, Nano Lett., 15, 3249–3253 (2015).

18. P. Nagpal and V. I. Klimov, Nat. Commun., 2, 486 (2011).

19. U. Banin and O. Millo, Annu. Rev. Phys. Chem., 54, 465–492 (2003).

20. L. Nienhaus, J. J. Goings, D. Nguyen, S. Wieghold, J. W. Lyding, X. Li and M. Gruebele, J. Am. Chem. Soc., 137, 14743–14750 (2015).

21. B. Cho, W. K. Peters, R. J. Hill, T. L. Courtney and D. M. Jonas, Nano Lett., 10, 2498–2505 (2010).

22. A. O. El-Ballouli, E. Alarousu, A. Usman, J. Pan, O. M. Bakr and O. F. Mohammed, ACS Photonics, 1, 285–292 (2014).

23. D. Nguyen, L. Nienhaus, R. T. Haasch, J. Lyding and M. Gruebele, J. Chem. Phys., 142, 234505 (2015).

24. L. Nienhaus, G. E. Scott, R. T. Haasch, S. Wieghold, J. W. Lyding and M. Gruebele, J. Phys. Chem. C, 118, 13196–13202 (2014).

25. J. W. Lyding, S. Skala, J. S. Hubacek, R. Brockenbrough and G. Gammie, Rev. Sci. Instrum., 59, 1897–1902 (1988).

26. P. M. Albrecht and J. W. Lyding, Small, 3, 146–152 (2007).

Appendix: Surface Dynamics of Non-conducting Glasses Under Water

One of the most popular forms of glasses is the non-conducting glass including silicate-based glasses and fused silica. We extend to study these glass surfaces under water to complement our work on metallic and semiconducting glasses under UHV.[1,2,3] Due to their non-conducting nature, atomic force microscopy (AFM) is employed to make movies of non-conducting glass surfaces. Tapping mode AFM under water is capable of providing lattice resolution on crystalline surfaces. Fig. A.1a shows an example of calcite surface imaged with AFM under water with lattice resolution. Fig. A.1b is a typical AFM image of fused quartz surface, in comparison with STM image of metallic glass surface in Fig. A.1c. Clusters on fused quartz surface are observed to be ~2 times larger compared to clusters on metallic glass surfaces. It may be due to the lower resolution of AFM compared to STM, lager drifting rates during AFM measurements (~10 times larger), faster scanning rate to compensate for thermal drift and hydration of surface clusters.

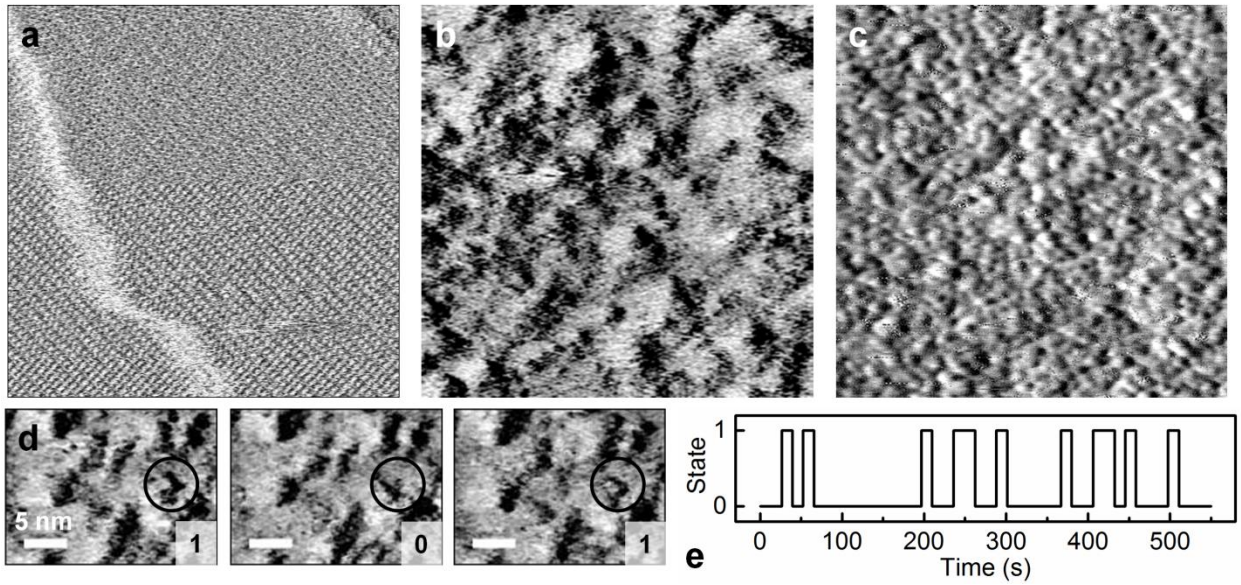

Figure A.1: AFM investigation of fused quartz surface under water. (a) AFM image of calcite under water. Image size 30 nm x 30 nm. (b) AFM image of fused silica under water. Image size 50 nm x 50 nm. (c) STM image of Ce-based metallic glass under UHV. Image size 50 nm x 50 nm. (d) Three frames showing a two-state cluster (circled) on fused silica surface under water. (e) The time trace for the cluster in (d).

Despite of difficulties and lower resolution of AFM, preliminary data shows that clusters on non-conducting glass surfaces also hop in a two-state fashion, in good agreement with our

previous work on metallic and semiconducting glasses.[1,2,3] An example of a two-state cluster on fused silica surface is shown in Fig. A.1d with complete time trace in Fig A.1e.

References

1. S. Ashtekar, G. Scott, J. Lyding, and M. Gruebele, J. Phys. Chem. Lett. 1, 1941 (2010).
2. S. Ashtekar, G. Scott, J. Lyding, and M. Gruebele, Phys. Rev. Lett. 106, 235501 (2011).
3. D. Nguyen, L. Nienhaus, R. T. Haasch, J. Lyding, and M. Gruebele, J. Chem. Phys. 142, 234505 (2015).